TU WIEN

DISSERTATION

Continuum Shell Models for Multi-Layer Carbon Nanostructures

ausgeführt zum Zwecke der Erlangung des akademischen Grades eines
Doktors der technischen Wissenschaften unter der Leitung von

O. Univ. Prof. Dipl.-Ing. Dr.techn. Franz G. RAMMERSTORFER
E317
Institut für Leichtbau und Struktur-Biomechanik

eingereicht an der Technischen Universität Wien
Fakultät für Maschinenwesen und Betriebswissenschaften

von

Dipl.-Ing. Melanie Todt
Matrikelnummer: 0225058
Canongasse 16
1180 Wien, Österreich

Wien, im Dezember 2012   Melanie Todt

For the things we have to learn before we can do,
we learn by doing.
Aristotle

Acknowledgments

Although the acknowledgments are on the first pages of this thesis, this is the last section I completed, hence, they mark the endpoint of four years of work. In the course of these four years of work I received a lot of support from my supervisor, my colleagues, my family, and my friends, and now I am struggling to find words which could express the gratitude I feel towards them.

I am deeply indebted to my supervisor Professor Franz G. Rammerstorfer for his constant support, motivation, advice and the countless discussions during the past four years. I am honored that I had the opportunity to be supervised by such a great scientist, engineer and cordial, humorous person.

I would also like to deeply thank Prof. Oskar Paris for reviewing this thesis and for the valuable feedback regarding its content. A would also like to thank him for the fruitful discussions and ideas regarding the compressive behavior of carbon crystallites.

Special thanks also goes to my colleagues, Dr. Markus A. Hartmann and Dr. David Holec, from the Montanuniversität Leoben for the great collaboration and the many discussion we had during the past four years about the modeling of carbon nanostructures. Further I would like to thank Professor Franz D. Fischer and Professor Paul H. Mayrhofer for the discussions regarding the compressive behavior of carbon crystallites and the van der Waals interactions in carbon onions.

The great working environment I experienced at the ILSB cannot be taken for granted, so I would like to thank all colleagues at the ILSB for making it possible to work in such an familial environment. Special thanks go to Maria Steininger, the good soul of the institute, for taking care of all administrative tasks and Gerhard Schneider for providing and maintaining such an outstanding computer infrastructure. I would also like to thank Prof. Helmut Böhm for reading my thesis and marking all the spelling and grammar mistakes, and for giving me a lot of feedback regarding the content.

Further I like to acknowledge the funding of this thesis by the fFORTE WIT - Women in Technology Program of the Vienna University of Technology, and the Austrian Federal Ministry of Science and Research. Besides the funding of the thesis, the fFORTE WIT program also provided opportunities for attending conferences and courses for professional development, for which I am deeply grateful. In this context I also like to thank Dr.$^{\text{in}}$ Sabine Cirtek and Mag.$^{\text{a}}$ Vera Kuzmits

I

for all the administrative work and support within the fFORTE WIT program.

Finally, I would like to thank my family for which I am switching to German. Zum Schluss möchte mich noch ganz herzlich bei meiner Familie für die großartige Unterstützung bedanken. Mein besonderer Dank gilt dabei meiner Mutter Hedwig Todt, die immer an mich geglaubt und mich immer unterstützt hat. Speziell in der Endphase meines Doktratsstudiums hat Sie mir den Rücken freigehalten, damit ich mich nur auf meine Dissertation konzentrieren konnte. Danke!

Abstract

Carbon nanostructures are nanometer-sized molecular structures made-up of pure carbon such as graphene, single- and multi-walled carbon nanotubes, fullerenes and carbon onions. They posses exceptional mechanical and electronic properties as well as high thermal conductivity which make them promising materials for semiconducting devices and fillers in conductive nanocomposites. To exploit the remarkable properties of these structures and to ensure their reliability and performance, their mechanical properties have to be well understood.

In the present thesis continuum mechanical shell models are used for studying the mechanical behavior of multi-layer carbon nanostructures. These models cause relatively low computational costs compared to atomistic simulation techniques and are – within certain limits – appropriate for studying the mechanical behavior of nanostructures. In continuum shell models of carbon nanostructures the atomic layers are represented by thin elastic shells and the van der Waals interactions between the layers are modeled by appropriate pressure-distance relations.

Different sets of shell parameters found in literature for carbon nanostructures are investigated regarding their suitability for describing the mechanical behavior of a single carbon layer subjected to different mechanical loads. Furthermore, the implication of layer curvature on the formulation of the van der Waals models are discussed and a new van der Waals model for spherical carbon nanostructures is derived. The findings made for the shell parameters and van der Waals interactions are then used for studying the compressive behavior of carbon crystallites and a possible growth limit of carbon onions.

The results obtained for the carbon crystallites are in good agreement with experimental observations made on bent carbon fibers that consist of such crystallites. Furthermore, these results lead to a better insight to the mechanisms determining the compressive behavior of carbon fibers. For carbon onions the occurrence of a structural instability due to mutual accommodation of onion layers is identified as a possible reason for their limited size. The obtained critical sizes are comparable to those observed in experiments.

For both carbon nanostructures experimental observations can be well predicted, confirming that continuum shell models can be used for investigating the mechanical behavior of carbon nanostructures.

Kurzfassung

Unter Kohlenstoff-Nanostrukturen versteht man molekulare Strukturen, die aus reinem Kohlenstoff bestehen und nur einige Nanometer groß sind, wie zum Beispiel Graphene, ein bzw. mehrschichtige Kohlenstoff-Nanoröhrchen, Fullerene, und Kohlenstoff-Zwiebeln. Kohlenstoff-Nanostrukturen besitzen bemerkenswerte mechanische und elektrische Eigenschaften und eine hohe Wärmeleitfähigkeit was sie zu viel versprechenden Materialien für den Einsatz in Halbleiterbauteilen und als Füllstoffe in leitenden Nano-Verbundwerkstoffen macht. Um die hervorragenden Eigenschaften von Kohlenstoff-Nanostrukturen vollständig ausnutzen zu können und um ihre Betriebseigenschaften und Zuverlässigkeit zu gewährleisten müssen die mechanischen Eigenschaften dieser Strukturen bekannt sein.

In der vorliegenden Arbeit werden die mechanischen Eigenschaften von mehrmehrschichtigen Kohlenstoff-Nanostrukturen mit Hilfe von kontinuumsmechanischen Schalenmodellen untersucht. Diese Modelle führen im Vergleich zu atomistischen Simulationsmethoden, zu einem geringeren Rechenaufwand und sind – innerhalb bestimmter Grenzen – geeignet um das mechanische Verhalten atomarer Strukturen zu untersuchen. In kontinuumsmechanischen Schalenmodellen von Kohlenstoff-Nanostrukturen werden die einzelnen atomaren Schichten mittels dünner Schalen modelliert und die van der Waals Interaktionen zwischen den einzelnen Schichten über geeignete Druck-Abstandsbeziehungen berücksichtigt.

Es wird ermittelt welche der verschiedene Schalenparameter-Sets für Kohlenstoff-Nanostrukturen aus der Literatur die mechanischen Eigenschaften der einzelnen atomaren Schichten unter verschiedenen mechanischen Belastungen gut abbilden können. Weiters wird der Einfluss der Krümmung der einzelnen Schichten auf die Formulierung der van der Waals-Modelle untersucht und ein neues van der Waals-Modell für kugelförmige Kohlenstoff-Nanostrukturen hergeleitet. Die so gewonnen Erkenntnisse bezüglich der Schalenparameter und van der Waals-Interaktionen werden dann verwendet um das Verhalten von Kohlenstoff-Kristalliten unter axialem Druck und eine mögliche Wachstumsgrenze von Kohlenstoff-Zwiebeln zu untersuchen.

Die erzielten Ergebnisse für die Kohlenstoff-Kristallite stimmen gut mit experimentellen Beobachtungen an gebogenen Kohlenstofffasern überein, deren Nanostruktur aus Kohltenstoff-Kristalliten besteht. Außerdem ermöglichen die gewonnen Ergebnisse einen besseren Einblick in die Mechanismen die das Verhalten von

Kohlenstofffasern unter axialem Druck bestimmten. Für die Kohlenstoff-Zwiebeln konnte das Auftreten einer strukturellen Instabilität, verursacht durch die gegenseitige Akkommodation der Schalen des Kohlenstoff-Zwiebels, als mögliche Ursache für die begrenzte Größe dieser Strukturen identifiziert werden. Auch hier konnten experimentelle Beobachtung im Hinblick auf die Größe der Kohlenstoff-Zwiebeln gut abgebildet werden.

Für die beiden untersuchten Kohlenstoff-Nanostrukturen konnten experimentelle Ergebnisse gut reproduziert werden, was die Anwendbarkeit von kontinuumsmechanischen Schalenmodellen zur Untersuchung des mechanischen Verhaltens solcher Strukturen bestätigt.

Contents

Chapter 1

Introduction

Carbon occurs in more chemical compounds than any other element and also pure carbon can be encountered in many different molecular configurations, the so called allotropes. Graphite and diamond are probably the most famous carbon allotropes known. Besides diamond and graphite, carbon nanostructures like carbon nanotubes [16, 69, 114, 169], graphene [23, 47, 48, 111, 175], fullerenes [79, 139], and carbon onions [11, 78, 151, 154] have drawn a lot of attention within the last years. Graphene is the strongest and thinnest material ever discovered [47], and the main building block of all carbon nanostructures. Thus, these particles should inherit the exceptional properties of graphene, making them promising candidates as fillers in nanocomposites especially for electronics applications [16, 99, 136]. However, for an expedient application of carbon nanostructures their properties should be well understood.

A lot of experimental work has already been done to study the structure and properties of such nanostructures, see e.g., [11, 68, 79] and computational techniques have also shown to be powerful tools for investigating carbon nanostructures [32, 94, 169]. Multi-layered nanostructures like multi-walled carbon nanotubes and carbon onions usually consist of a high number of atoms and, thus, atomistic simulation techniques become computationally expensive tasks. To reduce the computational requirements continuum mechanical methods may be employed which have shown to be appropriate for studying the mechanical properties of carbon nanostructures [114, 138, 169, 170].

Although continuum mechanical methods give reliable results for the properties of carbon nanostructures, there are still a number of modeling issues needing further discussion. The elastic properties to be used in continuum shell models are subject of intense discussions in the scientific community. Various different values can be found in literature for the elastic modulus, the Poisson's ratio, and the layer thickness, see, e.g., [87, 96, 114, 164, 169]. In multi-layer particles also the van der Waals interactions are of great importance, where the atom-atom interactions have to be described by appropriate continuum mechanical models [72, 97, 145].

1

Before the different modeling issues are addressed in the present thesis all carbon allotropes and their multi-layered configurations are presented and the state-of-the-art in their research is reviewed in Chapter 2. Chapter 3 provides an overview of the different computational techniques available for investigating the properties of carbon nanostructures, where continuum mechanical tools as well as atomistic methods are discussed. In the current thesis the focus is on continuum shell models. The choice of appropriate elastic parameters describing the shell properties is addressed in Chapter 4. Continuum mechanical van der Waals models to be used for different particles are presented in Chapter 5, where also a novel continuum vdW model for carbon onions is derived. The modeling strategies presented in Chapters 4 and 5 are then applied for studying the elastic properties of carbon cyrstallites in Chapter 6, which are the basic building blocks of PAN-based carbon fibers. Further, the continuum shell models are used to investigate a possible growth limit of carbon onions, see Chapter 7. Finally, the gained experience regarding continuum mechanical modeling of carbon nanostructures is summarized in Chapter 8.

In Chapters 4 and 5 the results obtained with continuum shell models are compared with those of Monte Carlo simulations. The models used in the Monte Carlo simulations are the outcome of intense discussions between M.A. Hartmann[1] and the author of this thesis. The Monte Carlo simulations itself are all conducted by Markus A. Hartmann and presented with his permission.

---

[1]Institute of Physics, Montanuniversität Leoben, Franz-Josef-Straße 18, A-8700 Leoben.

Chapter 2

Carbon and its Allotropes

2.1 Electronic structure and bonding configurations

The variety of carbon structures is due to the electronic configuration of single carbon atoms and bonding types arising thereof. In the Periodic Table, carbon is the first element in group IV and possesses six electrons. Two electrons are in the $1s$ orbital, the filled K-shell. The four other atoms are located in the L-shell, where two electrons are in the filled $2s$ orbital and the remaining two electrons are in the half-filled $2p$ orbitals. The electronic configuration of a carbon atom, hence, reads

$$1s^2 2s^2 2p^2 \ . \tag{2.1}$$

Carbon atoms bond together by forming covalent bonds, as a result of overlapping atomic orbitals. From the electronic structure it can be seen that only the two atoms in the $2p$ orbitals should be available as valence electrons, and, consequently, carbon should only be able to form 2 covalent bonds. However, carbon can form four bonds with other atoms (e.g., diamond or CH_4) requiring that the number of valence electrons is somehow increased from two to four. The process increasing the number of atoms and, hence, changing the electronic structure is called hybridization and takes place directly before the atomic orbitals overlap. A single carbon atom does not show any hybridized orbitals. During hybridization one electron of the $2s$ orbital is promoted to the $2p$ orbitals due to a small input of energy. The resulting bonding types then are a consequence of what happens between the electron in the $2s$ orbital and the three electrons in the $2p$ orbitals. Figure 2.1 shows the shapes of the $2s$ and $2p$ orbitals in the non-hybridized configuration as well as the different hybrid orbital configurations. In the $2s$ orbitals the electrons are distributed in a sphere around the atomic center. The $2p$ orbitals are dumbbell-shaped and preferentially aligned along the axis of a Cartesian co-

ordinate system with the atomic center being located in its origin. Figure 2.1 (a) shows also a $sp3$ hybrid orbital which is also dumbbell-shaped but one side of the dumbbell is smaller. For the sake of clarity the smaller orbital arm is not shown in the other figures.

sp3 hybridization

The $2s$ orbital blends with all three $2p$ orbitals. The resulting four $sp3$ hybrid orbitals are uniformly distributed in the space surrounding the atomic nucleus and the four valence electrons are equally distributed over the hybrid orbitals. The large orbital arms point towards the corners of a regular tetrahedron, see Figure 2.1 (b). Typical examples in which carbon forms $sp3$ orbitals and, hence, bonds with four other atoms, are methane (CH_4) or diamond.

sp2 hybridization

The shape of $sp2$ orbitals is similar to that of $sp3$ orbitals. In this configuration the $2s$ orbital mixes with two $2p$ orbitals leading to three $sp2$ orbitals. The $sp2$ orbitals are located in the same place as the $2p$ orbitals with which the $2s$ orbital blends. To maximize the distance between the $sp2$ orbitals the angle between them is 120°, see Figure 2.1 (c). The remaining p orbital is oriented perpendicularly to the plane spanned by the $sp2$ orbitals. Three of the four valence electrons are distributed among the three $sp2$ bonds and the fourth electron occupies the remaining $2p$ orbital. Carbon atoms possessing three bonding partners are $sp2$ hybridized. Ethene (C_2H_4) and graphene are typical $sp2$ bonded molecular structures.

sp hybridization

In this case the $2s$ orbital mixes only with one $2p$ orbital and the other two $2p$ orbitals remain unaffected. The p orbitals are oriented along the axis of the Cartesian coordinate system. Thus, the two resulting sp orbitals are located along the axis of the blended p orbital. The angle between the hybridized orbitals is 180° to maximize the distance between them. The two p orbitals stay oriented along the other two axes of the coordinate system, as shown in Figure 2.1(d). Two valence electrons occupy the sp orbitals and the other two valence electrons are located in the two $2p$ orbitals. Each sp hybridized carbon atom bonds with two other atoms. Ethin is an example for sp bonded carbon atoms (C_2H_2).

σ and π bonds

The type of bonds which form between hybridized atoms, depends on which orbitals overlap. If two hybridized orbitals overlap so called σ bonds are formed.

(a) *s* and *p* orbitals **(b)** *sp3* orbitals **(c)** *sp2* orbitals **(d)** *sp* orbitals
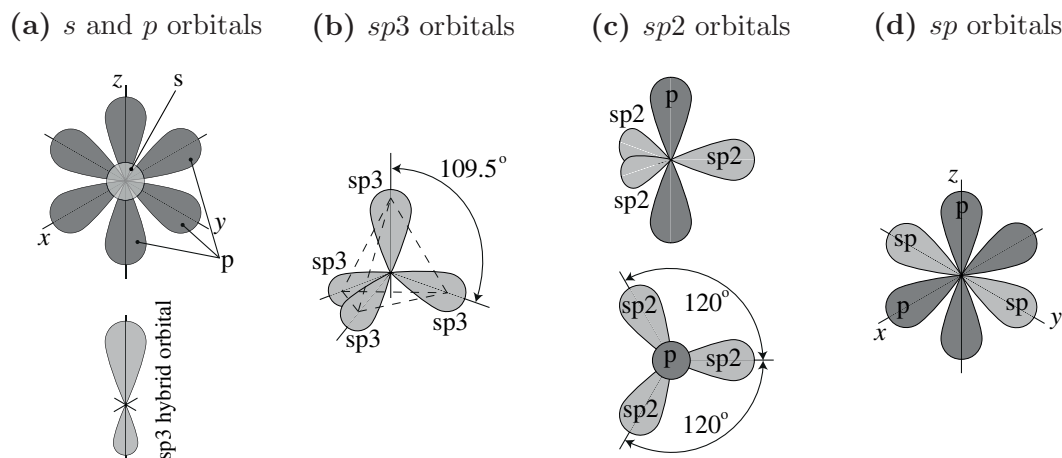
Figure 2.1: $2s$ and $2p$ orbitals of a carbon atom and the resulting different hybrid atom orbitals.

The overlap is formed along the internuclear axis connecting the two atomic nuclei. The charge density of this bond is largest in the space between the carbon atoms and σ bonds and very strong. σ bonds are rotationally symmetric about the internuclear axis, and thus allow a rotation around this axis.

Bonds formed by two overlapping p orbitals are called π bonds. The p orbitals are perpendicular to the internuclear axis and hence the overlapping is "sideways". The charge density is parallel to the internuclear axis, and the π bonds are weaker than the σ bonds. For example in Ethene the two carbon atoms are double bonded, where one bond is a σ bond and one bond is π bond. Each atom is also σ bonded to two H-atoms.

2.2 Diamond

Diamond is the first allotrope to be discussed. It is the hardest natural material known, and shows an exceptional thermal conductivity. Its atomic lattice is that of two interpenetrating face-centered-cubic lattices, where each atomic bond is formed by two overlapping $sp3$ orbitals. As only σ bonds occur, the bonding between the atoms is very strong leading to the high hardness of diamond.

At room temperature and normal pressure diamond is a metastable form of carbon. However, the activation energy for the phase transition to graphite is very high, so it can be excluded at room temperature. Diamond occurs in natural form and can be produced synthetically. In nature diamonds form in the earth's mantle under high pressure ($> 5\,\text{GPa}$) and at temperatures larger than 1400° C [107]. Natural diamonds occur all around the world, the largest amounts being mined in

Russia, Botswana and in the Democratic Republic of Kongo[1]. The formation of diamonds in the mantle is discussed in more detail, e.g., in [54].

Today various methods are available to produce synthetic diamonds. An overview about these methods is provided, e.g., in [171]. The first artificial diamonds were produced using a high pressure high temperature (HPHT) process [20], which is still commonly used. However, the resulting diamonds are of limited size and the amount of impurities in the lattice is hard to control. Chemical vapor deposition techniques allow more control over the amount of impurities and the resulting diamonds are larger then those of HPHT processes [171]. A mixture of hydrogen and methane is heated to 850 – 2000°C and deposited onto seed diamonds as single crystal diamond [107]. Further, this process can be used to produce polycrystalline thin diamond layers on silica, tungsten, or tungsten carbide wafers [107].

Diamond is a popular gemstone, but has also a wide range of industrial applications for which mainly synthetic diamonds are used. Diamond is a perfect cutting material due to its very high hardness and used especially in mining applications. Its low electric and high thermal conductivity make diamond also a favorable wafer material for the electronics industry [84].

2.3 Graphite and Graphene

Graphite has been known for a long time and its properties are well investigated. Overviews of the mechanical and electrical properties can be found, e.g., in [72, 120]. Graphite consists of a series of parallel layers formed by a hexagonal arrangement of carbon atoms, see Figure 2.2. The layers are called basal planes or graphene sheets. The atoms in the layers are $sp2$ bonded, where an angle of 120° between the $sp2$ orbitals (Figure 2.1 (c)) is responsible for the hexagonal atomic arrangements. The overlapping $sp2$ orbitals of neighboring atoms form single strong σ bonds, whereas the remaining p orbitals of each atom form a delocalized π bonding system [107]. The bond length a_{C-C} between neighboring atoms is about 0.142 nm [120]. The smallest periodic unit, the so called primitive unit cell, from which the hexagonal lattice can be generated contains two carbon atoms and is spanned by the basis vectors a_1 and a_2, see Figure 2.3.

The individual layers are stacked together in an ABAB arrangement as shown in Figure 2.2 and connected by nonlocal van der Waals interactions. Besides the hexagonal ABAB arrangement graphite also occurs in an rhombohedral ABCABC configuration. The values of the lattice constant a and the parameter c are listed in Table 2.1 for both graphite structures (taken from [120]) where the distance between neighboring layers is $c/2$. Both configurations have almost the same physical properties and thus, only the thermodynamically stable hexagonal form

---

[1]http://www.diamanten-infos.com/rohdiamant/jahr-produktion-2009.html
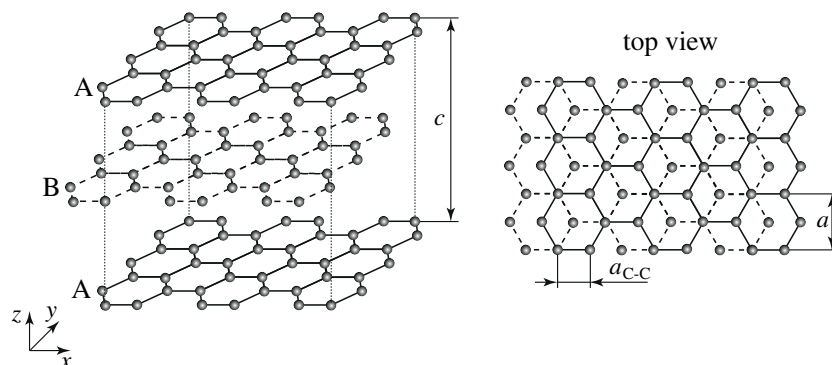
Figure 2.2: Lattice structure and layer arrangement in hexagonal graphite.

Table 2.1: Parameters of hexagonal and rhombohedral graphite.

	ABAB	ABCABC
a in nm	0.2462	0.2456
c in nm	0.67079	1.0044

of graphite is considered in the following.

The van der Waals (vdW) interactions between the layers are relatively weak compared to the covalent σ and π bonds. The difference between the in-plane and out-of-plane bonding configurations lead to anistropy of the graphite crystal. The strong σ bonds in the planes give rise to an elastic modulus of about $1000\,\text{GPa}$ measured parallel to the basal planes, whereas the modulus perpendicular to the basal planes is about $36.6\,\text{GPa}$ [183]. The shear stiffness between the layers is low due to the weak vdW interactions, thus, layers can easily be sheared off. Further, graphite shows a good thermal in-plane conductivity but is a thermal insulator perpendicular to the layers [120].

However, the anistropy of the graphite crystal can be of advantage in some applications. Due to the weak bonding between the layers, they can slide with respect to one another quite easily. Therefore, graphite is a good lubricant, especially for high and low temperature applications and also a good material for pencil leads. Further, graphite is of great importance in the steel making industry where it is used to raise the carbon content in molten steel or for electrodes in electric arc furnaces. Graphite is also used as anode material in all common battery types. A very special application of graphite is its use as neutron moderator in nuclear reactors.

Graphite occurs naturally in metamorphic rocks. According to the United States geological survey about $950\,\text{kt}$ where mined in 2012, with China and India being the largest producers[2]. Graphite also can be produced synthetically by

---

[2]http://minerals.usgs.gov/minerals/pubs/commodity/graphite/mcs-2012-graph.pdf

heating of coke to 2600-3000°C in an inert atmosphere, where the temperature is kept constant for one to three weeks [107].

A single layer of graphite, the so-called graphene, was first isolated in 2004 by Novoselov et. al [111] using mechanical exfoliation. Graphene is the basic structure of many carbon allotropes, like graphite, carbon nanotubes, and even fullerenes [48]. It is stable under ambient conditions and has remarkable electronic properties [111] and high thermal conductivity [82] making it a promising material for semiconductor devices. Its possible applications in field effect transistors, as transparent electrodes, or in solar cells are extensively reviewed in [31]. Further, graphene has potential applications in atomic dust detectors [125] or strain sensors [126], as the eigenfrequency of graphene patches is highly sensitive to mass changes as small as 10^{-6} fg and small strains, respectively. Graphene also possesses exceptional mechanical properties, and thus might be used as filler in composite materials [33]. Graphene-polymer composites are already conductive for graphene volume fractions lower than 2.5% [136]. To ensure the reliability and performance of graphene based products, the mechanical properties of graphene and the influence of defects and elevated temperatures have to be well understood.

Graphene is stated to be the thinnest and strongest material ever discovered [47, 83]. Nanoindentation experiments on single graphene layers have shown that graphene behaves elastic almost until breaking [23, 83]. It possesses a breaking strength[3] of about 42 N/m at 25% of mechanical strain [23, 83]. This high fracture strength can be reduced significantly by defects in the layers and elevated temperatures [180]. At 2400 K it is about 60% lower than the fracture strength at room temperature [180].

The presence of defects in graphene layers was shown, e.g., in [104] by transmission electron microscopy studies, where the formation and annealing of Stone-Wales defects is directly observed. Furthermore, free standing graphene is not perfectly flat and its edges tend to be folded [103]. Ab initio calculations performed in [18] showed that Stone-Wales defects at the edges lead to rippled edges and to a breakdown of the magnetic properties.

Ripples in graphene layers are also an effect of finite temperatures, where the amount and size of the ripples increases with increasing temperature [28]. The thermal rippling of the layers lead to a decrease in membrane stiffness, shear stiffness and Poisson's ratio of graphene [28]. In [28] it is also shown that the negative coefficient of thermal expansion observed in experiments [82] under ambient conditions is also caused by the thermal ripples. However, at a temperature of 568 K the coefficient of thermal expansion becomes positive [28]. Elevated temperatures also lead to an increase in the carbon-carbon bond length, whereas the value of the lattice constant becomes smaller [119]. This decrease in the lattice constant is

---

[3]The fracture strength is given in terms of force per unit length instead of force per unit area, as the thickness of a one atom thick graphene layer is subject of intense discussion in the scientific community, see Chapter 4.
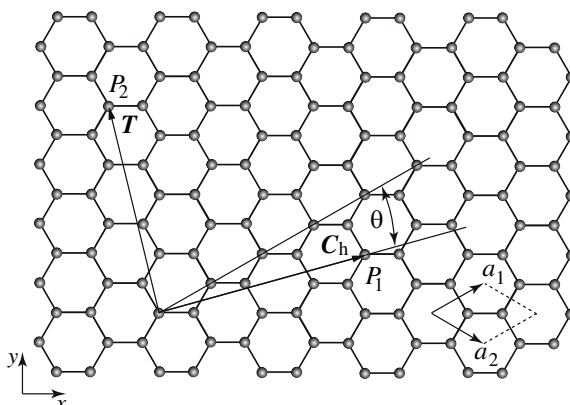
Figure 2.3: Graphene sheet with a_1 and a_2 as primitive vectors of the unit cell.

also attributed to the formation of thermal ripples [119].

Besides its high fracture strength, graphene possesses high stiffness which is sometimes expressed by high values of the elastic modulus E. Such values of E is often proposed to be around 1 TPa [8, 87, 89, 167], where a layer thickness h of approximately 0.34 nm is assumed for its calculation. However, the thickness of a one atom thick layer is the subject of intense discussion in the scientific community. Hence, the membrane stiffness $Eh \approx 340 \pm 40$ N/m [23, 83, 97] should be used to describe the inplane properties of graphene, for more details see Chapter 4.

Several methods are available to synthesize graphene, which can be divided into two groups: (i) top down and (ii) bottom up processes. Mechanical exfoliation [111] is a typical top down process. In this process the layers are separated from graphite and deposited onto a substrate by using a simple adhesive tape. Further top down processes are chemical exfoliation [155], chemical synthesis [137], and the unzipping of carbon nanotubes [24]. Chemical vapor deposition [135, 172] and the epitaxial growth of graphene on SiC surfaces [17, 71] belong to the group of bottom-up processes. A detailed description of production techniques for graphene can be found in [31, 134].

2.4 Single- and Multi-Walled Carbon Nanotubes

Multi-walled carbon nanotubes were first discovered by Iijima in 1991 [69], where a single layer is formed by a rolled graphene sheet. The interlayer distance between the individual concentric tubes is about 0.34 nm [120], and thus similar to the interlayer distance in graphite. However, the rolling of the graphene sheet is not unique, leading to many different forms of carbon nanotubes. The geometric properties of the nanotubes are fully determined by the duple (k, l) with the integers k and l being the so called chiral indices of the nanotube. The chiral angle Θ and the length of the chiral vector $|C_\mathrm{h}|$ shown in Figure 2.3 are related to the

chiral indices by

$$\sin(\Theta) = \frac{\sqrt{3}l}{2\sqrt{k^2 + l^2 + kl}} \tag{2.2}$$

and

$$|C_{\mathrm{h}}| = \sqrt{3}a_{\mathrm{C-C}}\sqrt{k^2 + l^2 + kl} \tag{2.3}$$

respectively [120], where $a_{\mathrm{C-C}}$ is the carbon-carbon bond length. The chiral angle is the angle between the chiral vector and the zig-zag direction of the graphene sheet, see Figure 2.3. For $l = 0$ and k being an arbitrary integer an angle $\Theta = 0°$ is obtained, leading to a so called zig-zag nanotube. An armchair nanotube is obtained if $l = k$, resulting in $\Theta = 30°$. Other combinations of k and l lead to carbon nanotubes with general chirality. The circumference of the carbon nanotube is equal to the length C_{h} and, thus, the diameter of the tube d_{T} reads [120]

$$d_{\mathrm{T}} = \frac{|C_{\mathrm{h}}|}{\pi} = \frac{\sqrt{3}a_{\mathrm{C-C}}\sqrt{k^2 + l^2 + kl}}{\pi} \ . \tag{2.4}$$

The chirality of the tubes is of great importance for the electronic properties of the nanotubes, which are related to k and l according to the following rules [120]

$$\text{if} \quad \frac{k-l}{3} \begin{cases} = \text{integer, metallic nanotube} \\ \neq \text{integer, semiconducting nanotube.} \end{cases} \tag{2.5}$$

Hence, armchair nanotubes are always metallic, whereas zig-zag nanotubes can be either metallic or semiconducting. Further, the chirality of the tubes influences their elastic properties [26]. The axial stiffness of armchair nanotubes is higher than those of zig-zag nanotubes. However, this difference vanishes with increasing tube diameters [26].

As carbon nanotubes are rolled graphene sheets, they should possess the same elastic properties as graphene. In [149] first evidence was found that the axial elastic modulus of carbon nanotubes is exceptionally high. An average value of $E \approx 1.8\,\mathrm{TPa}$ was obtained by measuring the thermal vibrations of multi-walled carbon nanotubes using transmission electron microscopy. Due to the curvature of the tube the carbon-carbon bond length is slightly larger than those of graphite [100], and also influences the elastic properties of the tubes. The axial stiffness of carbon nanotubes with small diameters is lower than those of graphene, but for tube diameters larger than 1.5 nm this difference becomes negligible [26]. The carbon-carbon bond length approaches the bond length of graphene with increasing tube radius [100]. Although, the hexagonal symmetry of the layers should lead to isotropic elastic properties, carbon nanotubes layers are found to be transversal isotropic [26, 106, 108]. However, for small deformations the behavior of the tubes can be considered as isotropic, without introducing a large error [165].

Their exceptional electrical and mechanical properties makes single- and multi-layered carbon nanotubes an interesting material for a lot of applications. A review

of different possible applications can be found, e.g., in [16]. In [9] a method is presented which allows the spinning of carbon nanotube yarns, which possess a tensile strength of about 700 MPa. Carbon nanotube forests are grown on iron-coated silica wafers using chemical vapor deposition. Then nanotubes are drawn away from the edges of the forests, these tubes cling together and form a strand. The properties of the spun yarns depend on the tube properties as well as on the twist of the yarn. Carbon nanotubes can also be used as actuators converting electrical energy to mechanical energy. This feature is exploited in [3], where thin aerogel sheets are drawn form carbon nanotube forests and tested for their ability to act as artificial muscles. Further, carbon nanotubes can be used as fillers in polymer matrices to produce conductive composites for the electronics industry, or as scanning probe tips for atomic probe microscopes [16].

Especially in the latter applications, the buckling load of carbon nanotubes is of importance as they are thin and slender structures. The axial buckling of multi-walled carbon nanotubes is experimentally investigated, e.g., in [52, 181]. After Euler beam buckling occurred, shell buckling of the layers due to bending of the tube is observed [181]. The shell buckling pattern is equal to the buckling pattern observed for purely bent nanotubes [95] and also predicted in [114] using continuum shell models. However, buckling experiments on nanotubes are difficult to realize, thus, computational methods are frequently used to investigate the buckling behavior of single- and multi-walled carbon nanotubes, see e.g., [138, 161, 162, 169]. Comparison with experiments show that the theoretical predicted buckling loads are often lower then the buckling loads observed in experiments [52]. This discrepancy is attributed to the formation of covalent interlayer bonds [52]. Covalent interlayer bonds between tube walls have shown to lead to an increased load transfer between the tubes [21, 179] and also improve the electric conductivity of multi-walled carbon nanotubes. However, if vacancies in the layers are involved in the formation of the interlayer bonds a reduction of the buckling load is observed [116, 179]. Detailed reviews of computational and experimental attempts concerning the buckling of carbon nanotubes can be found in [132, 160].

Carbon nanotubes can be grown using, e.g., an arc-discharge process, where a carbon source is evaporated and the tubes grow on a negative charged carbon electrode [69]. Large amounts of carbon nanotubes in the form of tube forests can be produced using chemical vapor deposition [3, 9]. Further production techniques are laser ablation of carbon [173] and gas-phase pyrolysis.

2.5   Fullerenes and Carbon Onions

Fullerenes are closed, hollow $sp2$ bonded carbon cages in the nanometer range. The first fullerene to be discovered was the C60, consisting of 60 carbon atoms arranged in 12 pentagonal and 20 hexagonal rings [79], see Figure 2.4. It is often referred to as buckminster fullerene in dedication to Richard Buckminster Fuller

C60 C240 C500 C1280
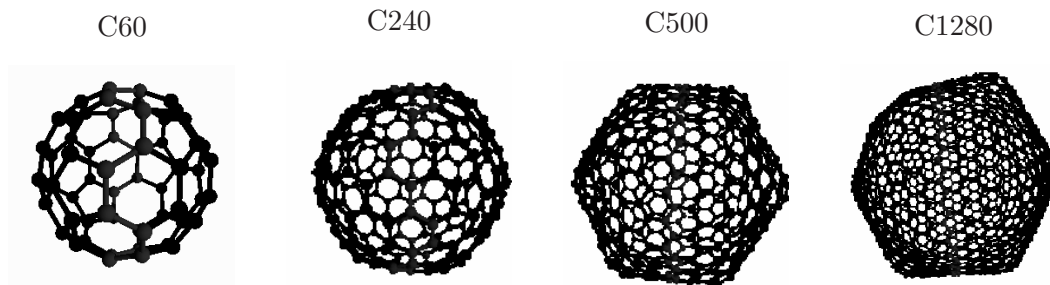
Figure 2.4: Icosahedral fullerenes of various sizes. By courtesy of Markus A. Hartmann, Institute of Physics, Montanuniversität Leoben, Franz-Josef-Straße 18, A-8700 Leoben.

whose geodesic-domes often show similar structures. The results obtained in [79] already indicated that larger fullerene clusters than C60 exist. The existence of fullerenes formed by $n = 72$, 76, 78, 84 atoms is theoretically predicted in [44] and all of them except C72 have been produced successfully [36, 42, 73].

C60 was first produced by vaporization of graphite due to intense laser irradiation [79], where only low quantities of C60 can be obtained. Macroscopic quantities of fullerenes were first produced by Krätschmer et al. [76]. In [76] graphitic electrodes are evaporated by resistive heating in a evaporation chamber filled with helium leading to graphitic carbon soot containing a few mass percent of C60. Today several other methods are in use, like arc heating of graphite [57], vaporization of graphite in solar generators [30], inductive heating of carbon samples [117], and pyrolysis of hydrocarbons [142]. Fullerenes can also be found in the soot of flames [50] and, thus, controlled combustion processes can be used to generate large amounts of fullerenes [2, 64]. A good overview of the mentioned techniques is provided, e.g., in [62].

In contrast to graphene and carbon nanotubes, which posses a pure hexagonal atomic structure, fullerenes also contain pentagonal rings, see Figure 2.4. Introducing pentagons in a hexagonal lattice leads to a local curvature at the location of the pentagon which is, e.g., illustrated in [25]. The number of pentagons needed to form a closed cage carbon structure can be evaluated under the following considerations. (i) It is assumed that fullerenes are only formed by hexagonal and pentagonal atomic arrangements. (ii) Each atom is covalently bonded to 3 other atoms and, thus, the number, n_{E}, of atom-atom bonds is equal to

$$n_{\mathrm{E}} = \frac{3n}{2} \tag{2.6}$$

where n is the number of atoms. (iii) According to Euler's theorem the number of faces can then be calculated as

$$n_{\mathrm{F}} = 2 + n_{\mathrm{E}} - n = 2 + \frac{n}{2} \tag{2.7}$$

With (i) Equation (2.7) can be rewritten as

$$n_5 + n_6 = 2 + \frac{n}{2} \tag{2.8}$$

with n_5 and n_6 being the number of pentagonal and hexagonal faces, respectively. (iv) At each atom three faces meet and therefore, the condition

$$n = \frac{5n_5 + 6n_6}{3} \tag{2.9}$$

has to be satisfied. Using Equations (2.8) and (2.9) the number of pentagons and hexagons can be evaluated as

$$n_5 = 12, \quad n_6 = \frac{n}{2} - 10 \; , \tag{2.10}$$

respectively. From Equation (2.10) it becomes apparent that under the above made assumptions the number of pentagons is exactly 12 and independent of the number of atoms forming the fullerene.

Fulfilling Euler's theorem is a necessary but not a sufficient condition for a fullerene being thermodynamically stable. Based on the work of [14] on corannulene molecules (bucky-bowls) and on the assumption that closed cell structures are preferred the so called isolated pentagon rule (IPR) is postulated in [77]. This rule states, that only such fullerenes are stable for which the pentagons are not in direct contact with each other. The IPR is an implication of the fact that the local stability of a fullerene increases if the local curvature decreases [75]. Two touching pentagons lead to a high local curvature, see e.g., Figure 1 in [25], and thus, are energetically less favorable. Besides this, fullerenes have to fulfill the valence requirements of carbon and thus, stable configurations can only consist of an even number of atoms [77]. All discovered fullerenes so far conform to Euler's theorem as well as the IPR and consist of an even number of atoms.

The smallest fullerene meeting all criteria is C60 [77]. For larger fullerenes like the C84 a number of isomers satisfying the IPR can be found. Although, these isomers are thermodynamically stable, only those with no antiaromatic π bonds are kinetically stable, and hence, isolable [1]. The existence of larger fullerenes is also investigated in [75], where only icosahedral cage structures are considered. Icosahedral fullerenes are special class of closed cage structures with their number of atoms being equal to [75]

$$n = 20(h^2 + hk + k^2), \quad 0 \le k \le h \; , \tag{2.11}$$

where h and k are integers. These fullerenes have the shape of a truncated icosahedron, where the pentagons are located at the vertices of the icosahedron. In [75] it is shown that C60, C180 and C240 have a relatively high stability. All of them belong to the group of icosahedral structures with either $h = 0$ or $h = k$,

and thus posses I_h-symmetry. Stability considerations on larger fullerenes [139] showed that all fullerenes with $h = k$ form a closed cell structure, which is not necessarily the case if $h = 0$. However, large fullerenes with $h = k$ ($n = 60k^2$) tend to form multi-layer arrangements as they are more stable [139].

Such multi-layered particles were first observed by Iijima in 1980 [68] and in [151] it is shown that they form from soot when subjected to intense electron irradiation. The multi-layered arrangements are called carbon onions [78] due to their onion-like structure. In [78] it is proposed that the layers of these particles are icosahedral fullerenes and that they grow through the spiraling network mechanism presented in [80, 178]. The proposed multi-layer fullerene structure and electron microscope photographs of these particles are depicted in Figure 2.5. They may show a rather polyhedral shape or be almost perfectly spherical, where in a strict sense only the spherical particles should be denoted as carbon onions.

Several techniques are available for producing multi-layered particles and carbon onions such as electron irradiation of graphite at elevated temperatures ($\geq$ 300°C) [11, 12], annealing of diamond nanoparticles [70, 148], high pressure transformation of single-crystal graphite [19], using a radio frequency plasma process [45], or synthesis by decomposition of phenolic resin [182]. In conjunction with the production technique also the growing process and the shapes of the resulting particles become of interest.

Onions produced by high-pressure transformation of single crystal graphite seem to grow from the inside to the outside [19, 40, 46]. The formation of single fullerene and a two-layered particles from graphitic layers is observed in [46],where the flexibility of the graphitic layers is of great importance for the formation of the particles. As shown by [32] the formation of single fullerenes from graphene is a multi-step process. First, pentagonal rings are formed due to the loss of carbon atoms at the edges of graphene. The pentagons then lead to the curvature of the graphene sheet, see also [25]. Finally the free edges are zipped open and form the fullerene structure. In [19] small graphite plates are located in a high-pressure diamond cell and subjected to high pressures and shear deformations. An increase in pressure and shear deformation leads to onions with a higher number of layers leading to the assumption that spherical multi-layered particles grow from the inside to the outside. Onion-like particles produced from coal by radio frequency plasma synthesis also grow in the same way [40].

If high-temperature annealing of nanodiamonds is used to produce carbon onions, the particles start their transformation at the outer boundaries of the nanodiamond [81, 148]. Atomistic simulations of this technique [94] reveal the transformation process. At a temperature of about 1500K the outer region of the nanodiamond transforms to graphitic layers leaving a nanodiamond at the center. Increasing the temperature to 3000K leads to the graphitization of the inner core. Finally the amorphous carbon in the center is transformed into concentric fullerene layers. The resulting onion has almost the same diameter as the initial
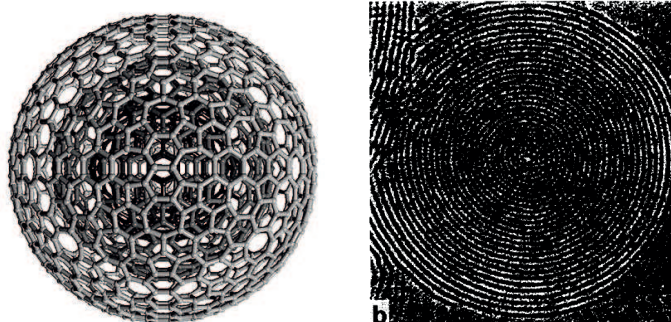
Figure 2.5: Multi-layer fullerene (left) and a transmission electron microscope (TEM) photograph of a carbon onion (right). TEM photo take from [12].

nanodiamond. A similar growing scenario has also been proposed in [68, 152] for particles produced by electric arc discharge experiments.

With some of the presented production techniques mainly multi-layered poly-hedral particles are obtained, see, e.g., [19, 45, 79, 182]. This polyhedral shape leads to the assumption that the layers of such particles and also of carbon onions are formed by icosahedral fullerenes [13, 78, 140]. Concentrically stacked fullerenes have interlayer spacings close to the interlayer distance of graphite which is about 0.34 nm. Thus, assuming that carbon onion layers are icosahedral fullerenes seems to be reasonable. Intense electron irradiation can be used to transform the poly-hedral particles to almost spherical ones [11, 12, 151]. At room temperature, the particles become more spherical but contain a large number of defects, whereas irradiation at elevated temperatures leads to particles consisting of concentric per-fectly spherical layers as shown for example in [12], Figure 2. For higher irradiation temperatures also a self compression of the spherical particles is observed, leading to a decrease in the interlayer spacing towards the center of the onion. In [12] it is proposed that the intense electron irradiation introduces vacancy defects by knocking out atoms from the individual layers. To eliminate the resulting dangling bonds the atoms in the layers rearrange and hence the layer shrinks. As conse-quence holes in the center of polyhedral particles disappear as they are filled by the surrounding shells [12]. This phenomena is already described in [153]. In [144] the transformation of polyhedral to spherical layers is investigated using atomistic simulations. As in [12] it is assumed that atoms are removed from the icosahe-dral layers by electron irradiation. The remaining holes are filled with heptagonal and additional pentagonal atomic rings in such way that the total number of pen-tagons in the layer is larger than 12. The newly formed layers posses a higher sphericity and contain a higher, lower, or equal number of atoms than the initial icosahedral layers. Similar calculations have been performed in [159], showing that the sphericity of fullerenes can be increased by introducing so called Stone-Wales defects.

Carbon onions should inherit the exceptional mechanical, electrical and electronic properties of graphene, due to their similar structure. Thus, they are also promising candidates as fillers in nanocomposites, especially for electronics applications [16, 99, 136]. Because of their multi-layer spherical structure they posses a high local electronic density and, therefore, a high ability of absorbing electromagnetic radiation. Their application as fillers in composites used for electromagnetic shielding is investigated, e.g. in [99]. Carbon onions have also potential application as additives in lubricants [70] or as solid lubricants [61]. Using C60 derivatives like C60Fe as lubricant is already proposed in [79]. As discussed above, subjecting carbon onions to electron irradiation at higher temperatures leads to a self compression of these particles. At about 700°C the core of carbon onions is transformed to a nanodiamond [10, 11, 121]. Hence, carbon onions can be used as nanoscopic pressure cells for nanodiamond production.

In all presented applications the size of the multi-layered particles is of substantial interest. But what is the maximum size to which these particles can be grown? In reality carbon onions can consist only of a few layers [70, 154], be of intermediate size [12, 19], or consists of many layers [163, 185] with diameters up to 50 nm. In [185] it is shown that the precursor material and the irradiation dose influence the size of the particles. Thus, the questions arise, if carbon onions can be grown to far larger sizes, or if there is something like a growth limit?

This question is addressed in Chapter 7 using continuum mechanical methods to simulate the growth of carbon onions. Similar considerations have already been made in [140] where it is proposed that carbon onions can grow to very large sizes. However, in contrast to [140] also the deformations of the layers due to vdW interactions and the possibility of a structural instability limiting the size of carbon onions are taken into account in Chapter 7.

Chapter 3

Modeling of Carbon Nanostructures

Today, computational methods are extensively used in practically all fields of applied sciences to gain better insight into phenomena observed in experiments. These methods allow to conduct analysis and parametric studies, which would cause tremendous costs or are not even possible in experiments. Furthermore, results obtained in computational simulations provide information about phenomena which might occur in experiments, and thus may influence the experimental setup.

Computational methods used for studying carbon nanostructures can be divided into atomistic and continuum mechanical methods. Atomistic methods are able to capture phenomena at the atomic scale, e.g., bond breaking, but usually are limited to relatively small structures formed by a few thousand atoms. For larger structures like multi-layer arrangements continuum mechanical methods can be used, which describe the behavior of the structure in an average sense. In the following sections a basic overview of the different methods is provided with the focus being on the simulation of the mechanical behavior of nanostructures. A more detailed description of many of the presented computational techniques is given, e.g., in [120].

3.1   Atomistic Methods

Carbon nanostructures are composed of n carbon atoms, with n ranging from a few atoms forming small molecules to several billion atoms making up multi-layer nanostructures. If the atomic structure is, e.g., subjected to macroscopic deformations, the individual atoms change their positions. This change in position is not arbitrary but depends on the forces each atom experiences due to its interactions with other atoms. In *ab initio* simulations these forces are calculated from

electronic-structure considerations, whereas in molecular dynamic or Monte Carlo simulations the forces are derived form interatomic potentials.

3.1.1 Ab initio Simulations

In *ab initio* simulations the forces between the atomic nuclei and, thus, the motion of the nuclei are calculated from electronic-structure calculations and require the solution of the many-body Schrödinger equation

$$H(\underset{\sim}{x}_i, \underset{\sim}{X}_I)\Psi(\underset{\sim}{r}_i, \underset{\sim}{X}_I)) = E\Psi(\underset{\sim}{r}_i, \underset{\sim}{X}_I) . \tag{3.1}$$

This equation states, that a wave function Ψ is a stationary state if the Hamilton operator acting on Ψ leads to a result that is proportional to the same wave function Ψ. E is the energy of this stationary state. The vectors $\underset{\sim}{x}_i = \{\vec{x}_1, \vec{x}_2, ..., \vec{x}_{ne}\}$ and $\underset{\sim}{X}_I = \{\vec{X}_1, \vec{X}_2, ..., \vec{X}_n\}$ contain the position vectors $\vec{x}_i$ and $\vec{X}_i$ of the *ne* electrons and n nuclei, respectively. The vector $\underset{\sim}{r}_i = \{\vec{x}_i, \vec{s}_i\}$ contains also the spins of the electrons. The Hamiltonian operator characterizes the total energy of a wave function and is given by

$$H(\underset{\sim}{x}_i, \underset{\sim}{X}_I) = K_\mathrm{N} + K_\mathrm{e} + H_\mathrm{I}^\mathrm{ee}(\vec{x}_i) + H_\mathrm{I}^\mathrm{NN}(\vec{X}_I) + H_\mathrm{I}^\mathrm{eN}(\vec{x}_i, \vec{X}_I)] \tag{3.2}$$

where, K_N and K_e are the kinetic energies of the electrons and nuclei, respectively. The energies due to electron-electron, nucleus-nucleus, and electron-nucleus interactions are given by H_I^ee, H_I^NN, and H_I^eN, respectively. The stationary wave function $\Psi(\underset{\sim}{r}_i, \underset{\sim}{X}_I)$ and the corresponding energy E, are the solution of the eigenvalue problem given by Equation (3.1).

An exact solution of this eigenvalue problem is difficult to obtain, even for small molecules consisting of a few atoms. Under some assumptions (Born-Oppenheimer approximation, adiabatic approximations, neglecting quantum effects in nucleus dynamics, for further details see, e.g., [120]) Equation (3.1) can be decoupled into one eigenvalue equation for the electrons and one for the nuclei. Under the above assumptions the latter equation, describing the nuclei movement, is replaced by the Newtonian equation of motion. The ground state energy of the nuclei required to calculate the forces on the nuclei, however, depends on the ground state energy of the electrons. Thus, the electron eigenvalue equation has to be solved, which is still an complicated task. Approximated schemes are adopted for solving this equation, where in material science the *density functional theory* (DFT) is used. Further details on DFT approximation techniques and *ab initio* methods can be found in [120] and references therein.

The biggest advantages of *ab initio* techniques are that, less input information is required and that scenarios are allowed to develop which where not considered before the simulations. The only input information needed is about the electronic configuration of the atoms making up a the structure. However, solving the underlying equations is a computationally expensive task, and therefore only applicable

for small structures. In [87] *ab initio* simulations are used to investigate the elastic properties of carbon nanotubes and graphene. The binding energy and intertube distance of bundles of carbon nanotubes is studied in [41], where also the vdW interactions are considered in an appropriate form. However, in *ab initio* simulations the correct treatment of vdW interactions in multi-layer structures is a complicated task. Some concepts are proposed in [37, 51].

For large multi-layer structures *ab initio* methods are not applicable due to their high computational costs, however they can be used to obtain the potential energy functions and the corresponding parameters needed in molecular dynamics and Monte Carlo simulations.

3.1.2 Molecular Dynamics and Monte Carlo Simulations

In molecular dynamics (MD) and Monte Carlo (MC) simulations interatomic potentials are used to describe the interactions between the n atoms forming the nanostructure. The required potentials are derived from *ab initio* simulations and describe interactions either between two atoms or many atoms. An overview about commonly used interatomic potentials is provided in [120].

In MD simulations the displacement of the atoms is described by Newtonian dynamics. At a time t the current configuration of a nanostructure is given by the position vectors $\vec{\boldsymbol{x}}_i$ and the velocities $\vec{\boldsymbol{v}}_i$ of all atoms $i = 1, ..., n$. The force acting on a single atom i can then be calculated as

$$\vec{\boldsymbol{F}}_i = -\sum_{j \neq i} \bigtriangledown_{\vec{\boldsymbol{x}}_i} E_{\text{pot}}(r_{ij}) \ , \tag{3.3}$$

The potential energy function $E_{\text{pot}}(r_{ij})$ describes the energetics of the atoms, and is assumed to be known. The quantity r_{ij} is the distance between atoms i and j and $\bigtriangledown_{\vec{\boldsymbol{x}}_i}$ denotes the spatial derivative of $E_{\text{pot}}(r_{ij})$ with respect to the current position of atom i. The sum ranges over the $n - 1$ neighboring atoms of atom i. However, usually the interatomic potentials are short-ranged involving only the nearest neighbors of atom i, thus only the contributions of these neighbors must be considered in the sum, reducing the computational requirements significantly. After the current interatomic forces $\vec{\boldsymbol{F}}_i$ are calculated the position vectors $\vec{\boldsymbol{x}}_i$ and velocities $\vec{\boldsymbol{v}}_i$ can be updated by integrating the three Newtonian equations of motion

$$m_i \ddot{\vec{\boldsymbol{x}}}_i = \vec{\boldsymbol{F}}_i \ . \tag{3.4}$$

where m_i denotes the mass of atom i. The system has reached a new state at time $t + dt$. If it has reached its equilibrium configuration the analysis stops, otherwise the procedure starts again with Equation (3.3). When the mechanical behavior of an atomic system is investigated the equilibrium configuration is indicated by a minimum of the potential energy and, hence, by $\vec{\boldsymbol{F}}_i = \vec{\boldsymbol{0}}$. Examples on potential energy functions are provided below in conjunction with MC simulations, see

Equation (3.5). For further details on the potential energy functions and the MD approach, see [120].

In MC simulations the displacements of the atoms are not calculated from the Newtonian equation of motion. Instead new configurations of the system are generated by randomly changing the positions of single atoms. A new configuration is accepted if the change of an energy quantity $\Delta\Pi < 0$ or if the probability p of the new configuration $p > 1$. The choice of the energy quantity and the probability function depend on the ensemble definition. For an ensemble where the number of atoms n, the volume to which these atoms are confined and the temperature are kept constant, Π is equal to the potential energy U and $p = \exp(-\Delta U / k_B T)$. Here, ΔU denotes the difference in the potential energy of the system before and after the displacement, T is the absolute temperature, and k_B is the Boltzmann constant. For further details on ensemble definitions and statistical mechanics, see [120] and references therein.

In the MC simulations conducted in Section 4.2 the potential energy of the system is approximated by the sum

$$U = \sum_{k_1} U^S_{k_1} + \sum_{k_2} U^B_{k_2} + \sum_{k_3} U^T_{k_3} \qquad (3.5)$$

of two-atom bond stretching, three-atom bond bending and four-atom bond torsion contributions $U^S_{k_1}$, $U^B_{k_2}$, and $U^T_{k_3}$, respectively. The indices k_1, k_2, and k_3 run over all covalently bonded pairs, all bond angles, and all torsion angles, respectively. The term of bond-stretching between two covalently bonded atoms i and j is described with the Morse potential,

$$U^S(r_{ij}) = U_0(\{1 - \exp[\beta(r_{ij} - r_0)]\}^2 - 1). \qquad (3.6)$$

with r_{ij} being the actual bond length and r_0 being the equilibrium bond length. U_0 is the bond energy and β^{-1} is the width of the potential. The bond-bending term is described by a harmonic potential,

$$U^B(\theta_{ijk}) = \frac{1}{2} k_\theta (\cos\theta_{ijk} - \cos\theta_0)^2, \qquad (3.7)$$

where θ_{ijk} is the angle between the $i - j$ and $j - k$ bonds, θ_0 is the equilibrium bond angle, and k_θ is the bending force constant. The torsion contribution is given by

$$U^T(\phi_{ijkl}) = \frac{1}{2} k_\phi (1 - \cos 2\phi_{ijkl}), \qquad (3.8)$$

where ϕ_{ijkl} is the torsion angle and k_ϕ is the torsion force constant. The change in the potential energy ΔU can then be calculated as

$$\Delta U = U_{\text{new}} - U_{\text{old}} + \sum_l \vec{\boldsymbol{F}}^{(\text{ext})}_l \cdot \Delta\vec{\boldsymbol{x}}_l \qquad (3.9)$$

with U_{new} and U_{old} being the potential energies of the new and previous configuration, respectively. The vectors $\vec{F}_l^{(\text{ext})}$ and $\Delta\vec{x}_l$ denote an external force acting on an atom l and the displacement of this atom due to this force, respectively, where l runs over all atoms experiencing an external force. A new equilibrium configuration is obtained if the free energy $G = U - TS$ as a function of the potential energy U, the temperature T, and the entropy S of the system reaches a minimum value.

Molecular dynamics simulations are often used to study the mechanical behavior of carbon nanostructures, like carbon nanotubes [101, 169, 174] or graphene [22, 23, 175, 184]. MC simulations are less frequently employed for investigating carbon nanostructures. For example, Chen et al. [28, 29] used MC simulations to study the plastic elongation of carbon nanotubes and the influence of temperature on the elastic constants of graphene. MC simulations are also used in [63] to investigate the curvature induced excess surface energy in spherical nanoparticles.

Compared to *ab initio* simulations MD and MC methods require more input information, like the energy potential functions and the parameters used in the functions. However, they are computationally less expensive and the vdW interactions between atoms can be easily considered. The vdW interactions can be described by a pair potential such as the Lennard-Jones potential, see Chapter 5, and thus simply contribute to the total potential energy of the system.

3.2 Continuum Mechanical Methods

Within certain limits, continuum mechanical models have shown to be appropriate to describe the mechanical behavior of carbon nanostructures, see e.g., [86, 122, 169]. Compared to atomistic simulation techniques the computational requirements of continuum mechanical approaches are relatively low, allowing the investigation of large atomic structures. Using continuum mechanics the layers of carbon nanostructures can be modeled either as space frame structure using beam- and/or spring elements [86, 124] or as continuum shells [114, 169]. Both modeling concepts are briefly discussed in the following sections. However, only continuum shell models are used in the present thesis for studying the mechanical behavior of carbon nanostructures.

3.2.1 Space Frame Models

Space frame models of carbon nanostructures are closely related to MD models. The atomic bond properties are described by structural elements like beams or springs instead of interaction potentials used in MD simulations. In this section only beam models of carbon nanostructures are discussed in more detail. Information about continuum spring models for carbon nanostructures can be found,

e.g., in [102].

Using continuum beams for modeling atomistic structures is often referred to as lattice structure method or molecular structural mechanics approach. The properties of the beams are derived from interatomic potentials used in MD simulations, where usually a circular cross section of the beams is assumed [85, 86, 124]. Following the approach presented in [86] the total potential energy of a system can be expressed as

$$U = \sum_{k_1} U^S + \sum_{k_2} U^B + \sum_{k_3} U^{T_1} + \sum_{k_4} U^{T_2} + \sum_{k_5} U^{\mathrm{vdW}} \qquad (3.10)$$

where U^S is the two-atom bond stretching contribution, U^B is the energy due to three-atom bond bending, U^{T_1} and U^{T_2} denote the dihedral and out-of-plane torsion contribution involving four atoms, respectively, and U^{vdW} accounts for the in-plane vdW interactions. Hence, k_1 spans all covalent bonded atom pairs, k_2, k_3, k_4 run over all bending and trosional angles and k_5 spans all vdW interactions in the layers. In the following the in-plane vdW interactions are not considered and the two trosional terms U^{T_1} and U^{T_2} are combined in a single term U^T [86]. The resulting simplified expression of the potential energy is then equal to Equation (3.5). In contrast to the MC approach above, small strains are assumed and the energy contributions are described by simple harmonic forms [86]

$$U^S = \frac{1}{2}k^S(\Delta r)^2 \qquad (3.11)$$

$$U^B = \frac{1}{2}k^B(\Delta\theta)^2 \qquad (3.12)$$

$$U^T = U^{T_1} + U^{T_2} = \frac{1}{2}k^T(\Delta\phi)^2 \ . \qquad (3.13)$$

The parameters k^S, k^B, and k^T denote the bond stretching, bond angle bending, and bond torsional resistance, respectively. The changes in bond length, bond angel and the twisting increment are described by Δr, $\Delta\theta$, and $\Delta\phi$, respectively.

The strain energy contributions of a beam subjected to pure tension, pure bending, and pure torsion are given in a similar form by

$$U_{\mathrm{S}} = \frac{1}{2}k_{\mathrm{S}}(\Delta L)^2 (\text{beam stretching}) \qquad (3.14)$$

$$U_{\mathrm{B}} = \frac{1}{2}k_{\mathrm{B}}(2\alpha)^2 (\text{beam bending}) \qquad (3.15)$$

$$U_{\mathrm{T}} = \frac{1}{2}k_{\mathrm{T}}(\Delta\beta)^2 (\text{beam torsion}) \ , \qquad (3.16)$$

respectively, with k_{S}, k_{S}, and k_{T} being the axial, bending, and torsional stiffness of the beam. The variables ΔL, α, and $\Delta\beta$ denote the change in beam length, the beam bending angle, and the torsional angle of the beam, respectively; for more

details see [86]. Under the assumptions that $\Delta L = \Delta r$, $2\alpha = \Delta\theta$, and $\Delta\beta = \Delta\phi$, the stiffness properties of the beam are directly obtained by comparing Equations (3.11) to (3.13) with (3.14) to (3.16) as

$$k_{\mathrm{S}} = k^S, \quad k_{\mathrm{B}} = k^B, \quad k_{\mathrm{T}} = k^T \ . \tag{3.17}$$

Space frame models are applied to study the tensile behavior of single- and multi-walled carbon nanotubes [8, 85, 86, 150] and graphene [124]. For carbon nanotubes an elastic modulus of $\approx 1000\,\mathrm{GPa}$ is obtained assuming a wall thickness of $0.34\,\mathrm{nm}$. For graphene an elastic modulus of $1040\,\mathrm{GPa}$ and a Poisson's ratio of $1.129 - 1.441$ are found [124]. In the simulations of the multi-walled nanotubes the vdW interactions are modeled via nonlinear springs [85]. Furthermore, space frame models are applied to investigate buckling of graphene [123] and the influence the of defects on the mechanical behavior and elastic properties of graphene [49, 141].

3.2.2 Shell Models

Using continuum shells for modeling single carbon layers was first proposed by Yakobson et al. [169]. In [169] the membrane stiffness C and the bending stiffness D of a nanotube layer are calculated by comparing the change in total energy obtained by MD simulations to the strain energy introduced in a continuum model of the tube for the same deformation state. The Poisson's ratio $\nu = 0.19$ is evaluated from the reduction of tube diameter due to axial deformation [169]. In the following the energy considerations made in [169] are briefly reviewed.

Using MD simulations it is shown that the change in total energy per atom $\Delta\bar{U}_{\mathrm{A}}$ of a nanotube subjected to axial compression is expressed as

$$\Delta\bar{U}_{\mathrm{A}} = \frac{1}{2}(\Delta\bar{U}_{\mathrm{A}})''\epsilon_x^2 \tag{3.18}$$

where $(\Delta\bar{U}_{\mathrm{A}})''$ is the second derivative of $\Delta\bar{U}_{\mathrm{A}}$ with respect to the axial strain ϵ_x. For $\Delta\bar{U}_{\mathrm{A}}''$ a value of $59\,\mathrm{eV/atom}$ is found in [169]. For the whole nanotube the change in total energy can then be expressed as

$$\Delta U_{\mathrm{A}} = \int_S \rho\Delta\bar{U}_{\mathrm{A}}\mathrm{d}S = \int_S \rho\frac{1}{2}(\Delta\bar{U}_{\mathrm{A}})''\epsilon_x^2\mathrm{d}S, \tag{3.19}$$

with ρ as the atom area density and S as the surface area of the nanotube.

Assuming that the nanotube is a thin cylindrical shell the strain energy V_{A} due to the axial deformation of the tube depends only on the membrane strains and, hence, reads

$$V_{\mathrm{A}} = \frac{1}{2}\int_S \frac{C}{1-\nu^2}[(\epsilon_x + \epsilon_y)^2 - 2(1-\nu)(\epsilon_x\epsilon_y)]\mathrm{d}S \tag{3.20}$$

where S denotes the surface area of the tube. In a small strain setting the circumferential strain ϵ_y can be expressed as

$$\epsilon_y = -\nu\epsilon_x \ . \tag{3.21}$$

With Equation (3.21), Equation (3.20) simplifies to

$$V_{\mathrm{A}} = \frac{1}{2} \int_S C \epsilon_x^2 \mathrm{d}S \ . \tag{3.22}$$

By comparing Equation (3.19) with Equation (3.22) the membrane stiffness is obtained in [169] as

$$C = \rho(\Delta \bar{U}_{\mathrm{A}})'' = 360 \,\mathrm{N/m} \ . \tag{3.23}$$

The bending stiffness is calculated from the strain energy U_{R} introduced by rolling a graphene sheet to a tube with radius R. For a continuum shell model U_{R} reads

$$U_{\mathrm{R}} = \frac{1}{2} \frac{D}{R^2} \tag{3.24}$$

if a thin shells are assumed. The strain energy U_R is equal to $|U_{\mathrm{NT}} - U_{\mathrm{G}}|$ denoting the difference between the total energy of a carbon nanotube and a planar graphene sheet, leading to a bending stiffness $D = 0.16 \,\mathrm{nN}\,\mathrm{nm}$ [169]. Finally, an elastic modulus $E = 5500 \,\mathrm{N/mm^2}$ and a thickness $h = 0.066 \,\mathrm{nm}$ are obtained using the standard relations $C = Eh$ and $D = Eh^3/(12(1 - \nu^2))$. With these values the buckling behavior of carbon nanotubes could be well predicted [169].

Later investigations regarding the strain energy of carbon nanotubes confirmed that modeling the atomic layers by continuum shells is consistent with atomistic modeling techniques and that the values obtained in [169] are in the correct order of magnitude [166].

Isotropic thin shell models were successfully applied in [114] to study buckling of multi-walled carbon nanotubes subjected to axial loading and bending. The obtained buckling patterns agree well with buckling patterns observed in experiments and the obtained strain energy histories are in good agreement with those of atomistic simulations. Also findings of [15] show that continuum shell models are applicable for modeling carbon nanostructures.

In multi-layered carbon nanostructures vdW interactions between adjacent layers have to be considered in an appropriate form. In [60, 114, 122] pressure-distance relations are used, whereas in [15] the vdW interactions are modeled via trusses (possessing only an axial stiffness). Both concepts are used in the present thesis to describe the vdW interactions between neighboring layers, see Chapters 6 and 7. A detailed description about the modeling of vdW interactions in continuum shell models can be found in Chapter 5.

The shell model proposed in [169], however, does not account for the chirality of nanotubes and also small scale effects cannot be considered. Further it was shown in [66] that the elastic parameters depend on the type of loading. Thus, more advanced shell models were proposed, e.g., [6, 7, 26, 131, 164]. In [164] an atomistic-based shell model is derived, which fully considers the anisotropy and chirality of the tube, but avoids the definition of a layer thickness h. An atomistic-based shell model accounting for the size and chirality of the tubes is also proposed

in [26]. Additionally, nonlocal elastic shell models are proposed, see, e.g., [6]. This analytical models give a very good representation of the fundamental frequencies of nanotubes if appropriate nonlocal parameters are used [6]. The application of nonlocal shell models for modeling carbon nanostructures is extensively reviewed in [7].

More advanced models are able to capture some features like the chirality introduced anisotropy of the shell, but they lead to more complex models. For example, the nonlocal parameter required in a nonlocal shell model depends on the size of the nanotube, the boundary conditions used, and also on the number of layers making up a multi-walled nanotube [7]. Therefore, this parameter has to be specifically evaluated for each tube configuration by comparison with atomistic simulations increasing the computational costs of these methods. Further, the influence of chirality on the elastic properties of carbon nanotubes vanishes fast with increasing radius, and is negligible for tube diameters larger than 1 nm [26]. And also the assumption of isotropic layers is admissible for small deformations [165].

In the present thesis only small strains are considered, and for the carbon onions investigated in Chapter 7 spherical symmetry is assumed. Thus, the simple isotropic elastic shell model presented in [169] and [114] is used. The choice of the corresponding elastic constants is discussed in Chapter 4.

3.2.3   Multi-Scale Methods

For the sake of completeness also multi-scale methods are mentioned but not discussed in detail. An exhaustive review of these methods can be found, e.g., in [88, 90].

Multi-scale methods take advantage of both, atomistic and continuum mechanical approaches. Thus, they can be used to investigate the mechanical behavior of large carbon nanostructures where at specific positions the local atomic configurations are of importance. The main issue of multi-scale approaches lies on the smooth bridging between the atomistic and continuum length scale.

A multi-scale approach is, e.g., used in [168] to investigate the crack propagation in a graphene sheet. The area around the crack tip is represented by a quantum mechanical domain (*ab initio*) and moves with the crack tip, the rest of the graphene sheet is modeled as continuum shell.

Chapter 4

Elastic Properties of Single Carbon Layers

4.1 Motivation

In the present thesis the layers of carbon nanostructures are modeled as thin shells as proposed in [114, 169]. In graphene the atoms are arranged in a hexagonal structure. Hence the material behavior is isotropic in a small strain setting. Furthermore, nanoindentation experiments revealed that graphene possesses an elastic material behavior almost until breaking [83]. Under these considerations the behavior of the thin shells can then be described using three independent parameters: membrane stiffness

$$C = Eh \tag{4.1}$$

bending stiffness

$$D = \frac{Eh^3}{12(1 - \nu^2)} \tag{4.2}$$

and Poisson's ratio ν. The variables E and h denote the elastic modulus and the thickness of the layers, respectively.

As shown in Table 4.1 a lot of experiments, atomistic simulations, and analytical investigations have been carried out to estimate the elastic properties of a single carbon layer. The values given for E, h and ν vary significantly and also the values of C and D show large differences. It should be noted, that the elastic modulus E is often calculated from the tensile stiffness of carbon nanotubes or graphene sheets by assuming that the thickness h of a carbon layer is equal to the interlayer spacing of graphite $h = c/2 \approx 0.34$ nm [8, 87, 89, 167, 175, 177], with c as shown in Figure 2.2. This thickness leads in combination with the corresponding values of E and ν, to a far larger bending stiffness than obtained, e.g., in [22, 96, 97]. Nevertheless, in [167] it was possible to reproduce nanoindentation

experiments conducted by [83] with an assumed thickness of 0.34 nm.

Table 4.1: Values for C, D, E, h and ν found in literature.

Method/Structure/Ref.	C [J/m^2]	D [nNnm]	E [GPa]	h [nm]	ν [-]
[8] molecular structural mechanics					
graphene, in-plane	-	-	~ 1000	0.34[1]	0.16[1]
graphene, out-of-plane	-	-	~ 110	0.34[1]	0.16[1]
[23] molecular dynamics, graphene	312				0.31
[22] molecular dynamics, graphene		0.2242			
[83] nanoindentation experiments					
graphene	342 ± 30	0	-	-	-
[87] *ab initio*					
graphene	-	-	1110	0.34[1]	-
nanotube $r = 0.344$ nm	-	-	1060	0.34[1]	0.125
nanotube $r = 0.369$ nm	-	-	940	0.34[1]	0.047
[89] *ab initio*, nanotubes	-	-	1050	0.334[1]	0.186
[96] analytically, graphene					
1st gen. Brenner pot.	-	0.133	-	-	-
2nd gen. Brenner pot	-	0.110	-	-	-
incl. dihedral angle effect	-	0.225	-	-	-
[97] analytically, graphene	340 ± 50	0.255			0.398
[114] finite element method, nanotubes	363	0.176	4840	0.075	0.19[1]
[130] molecular mechanics, nanotubes					
MM3 ([5])	-	-	2520	0.134	0.21
Tersoff-Brenner	-	-	3100	0.098	0.26
[165] atomistic-based shell theory					
graphene[2]	~ 470	~ 0.22	-	-	-
nanotubes[2]	~ 480	~ 0.225	-	-	-
[166] electronic band theory, nanotubes	377.4	0.183	5100	0.074	0.24
	(357.7)	(0.176)			
[167] *ab initio*, graphene	-	-	1030	0.34[1]	0.22
[169] molecular dynamics, nanotubes	363	0.137	5500	0.066	0.19
[177] nanoscale continuum theory					
nanotubes, parameter set 1	159	-	475	0.335[1]	-
nanotubes, parameter set 2	236	-	705	0.335[1]	-
[175] molecular dynamics, graphite	-	0	1240	0.34[1]	0.24
[184] molecular dynamics, graphene	235.88	-	-	-	0.4136

[1] Values are assumed in the cited papers.

[2] Values obtained for the unstrained nanostructures.

Furthermore, it is not fully accepted that a single graphene layer has an intrinsic bending stiffness. In nanoindentation experiments of graphene the strain energy

due to bending is three orders of magnitude lower than the energy quantities due to in-plane strain [83]. From this results it is concluded in [83] that graphene has zero bending stiffness. However, the comparison between the strain energies due to bending and in-plane strain is not admissible, as these energies are two different physical quantities. Zero bending stiffness of graphene is also proposed in [175], as bending of a one atom thick layer does not lead to any tensile or compressive strains in the layer. Although pure bending does not lead to a change in the atom-atom distance, further effects like three-atom bending or four-atom out-of-plane torsion contribute to the total potential energy of the system. These energy contributions are disregarded in [175], but have also to be considered in the evaluation of the bending stiffness of single graphene layers. Furthermore, the conclusions drawn in [83] and [175], are in clear contradiction to observations made in [22, 96, 97] by atomistic simulations.

The above examples show, that it is not clear which combination of E, h, and ν represents the behavior of a single carbon layer most accurately. The parameter sets listed in Table 4.1 were all derived for graphene or nanotubes, fullerenes were not considered for evaluating the elastic parameters so far. Thus, fullerenes are used in the present chapter to investigate which of the parameter sets listed in Table 4.1 gives a good representation of the mechanical behavior of a single carbon layer.

4.2 Analytical Considerations on Fullerene Layers

Fullerenes are closed, cage like structures, which are almost spherical in their shape as long as their radii are small enough, see Section 2.5. For basic analytical considerations they can assumed to be perfectly spherical and, hence are modeled as thin spherical shells. In this chapter the fullerenes are subjected to an external hydrostatic pressure and to a circumferential load at the equator of the sphere to study their stiffness properties. The results obtained with the analytical model are compared to results of MC simulations.

The MC simulations are performed according to the procedure described in Section 3.1.2 and conducted by Markus A. Hartmann[1] [56]. The parameters used in the potentials for the MC simulations are derived from *ab initio* simulations [63], their values are listed in Table 4.2.

The radii of the spheres representing the fullerenes are assumed to be equal to the mean radii of the fullerenes. Using MC simulations the mean radii $R^{(0)}$ can be calculated from the equilibrium configurations of unloaded fullerenes as [56]

$$R^{(0)} = \langle |\vec{\boldsymbol{x}}_i - \vec{\boldsymbol{X}}| \rangle. \tag{4.3}$$

---

[1]Institute of Physics, Montanuniversität Leoben, Franz-Josef-Straße 18, A-8700 Leoben.

Table 4.2: Parameters used in the potentials for the MC simulations [56].

Parameter	Symbol	Value
stretching potential	E_0	$6.1322\,\text{eV}$
inverse width of the potential	β	$0.18502\,\text{nm}^{-1}$
equilibrium carbon-carbon bond length	$r_0 a_{\text{C-C}}$	$0.14322\,\text{nm}$
bending force constant	k_Θ	$10\,\text{eV}$
equilibrium bond angle	Θ_0	$120°$
torsion force constant	k_ϕ	$0.35\,\text{eV}$

Table 4.3: Mean radii of different carbon fullerenes obtained from MC simulations [56].

	C60	C240	C500	C1280
$R^{(0)}$ [nm]	0.355	0.711	1.023	1.631

The vectors $\vec{x}_i$ and $\vec{X}$ are the position vectors of atom i and of the fullerene's center of mass, respectively. The angular brackets denote averaging over all atoms. Table 4.3 shows the mean radii obtained for different fullerenes.

Different parameters sets for E, h, and ν are used in the analytical continuum models to investigate which parameter should be used in a continuum shell model. The parameter sets and the corresponding values of C and D are given in Table 4.4. All parameter sets are taken from Table 4.1.

The obtained values of the membrane stiffness C are within or close to the experimentally obtained range $C = 342 \pm 30\,\text{N/m}$ [83]. Only ES4 slightly underestimates the experimental value, but is still close to the lower limit of the experimental range. The results for the bending stiffness D are more diverse, and not all of them match observations made in other references listed in Table 4.1. According to the values given in Table 4.1 the bending stiffness of a single graphene layer is in the range $0.11\,\text{nN\,nm}$ to $0.255\,\text{nN\,nm}$, even if the references used in Table 4.4 are not considered. Sets ES1, ES2, and ES4 are within or close to

Table 4.4: Parameter sets used for modeling the elastic properties of fullerene layers.

Set Name	Reference	E [GPa]	h [nm]	ν [-]	C [J/m^2]	D [nNnm]
ES1	[169]	5500	0.066	0.19	363	0.136
ES2	[114]	4840	0.075	0.19	363	0.176
ES3	[130]	2520	0.134	0.21	337.68	0.528
ES4	[130]	3100	0.098	0.26	303.80	0.260
ES5	[89]	1050	0.334	0.186	350.70	3.377

Table 4.5: Hydrostatic stiffness of different fullerenes obtained from MC simulations and analytical considerations (MC data from [56]).

| Fullerene | $K_{\mathrm{H}}^{(\mathrm{MC})}$ [N/m] | $K_{\mathrm{H}}^{(\mathrm{MCS})}$ [N/m] | K_{H} [N/m] | | | | |
			ES1	ES2	ES3	ES4	ES5
C60	9859	10021	11263	11263	10743	10318	10828
C240	9061	9750	=	=	=	=	=
C500	8499	9764	=	=	=	=	=
C1280	8259	9756	=	=	=	=	=

this range, whereas ES4 gives a significantly higher value for the bending stiffness of a single layer. The bending stiffness obtained with ES5 exceeds all other values by an order of magnitude. This fact was already stressed in the previous section.

In the first loading case the fullerenes are subjected to an external pressure p_{H}. The change in radius ΔR is then related the total applied force via

$$F_{\mathrm{H}} = p_{\mathrm{H}} A_0 = \frac{8\pi C}{1-\nu} \Delta R \qquad (4.4)$$

where $A_0 = 4\pi (R^{(0)})^2$ is the surface area of the undeformed sphere with radius $R^{(0)}$. Hence, the stiffness parameter

$$K_{\mathrm{H}} = \frac{8\pi C}{1-\nu} \qquad (4.5)$$

obtained for the continuum model is independent of the fullerene radius. To realize a hydrostatic pressure in the MC simulations each atom i is subjected to an external force $\vec{F}_i^{(\mathrm{ext})}$ pointing towards the center of mass of the fullerene. The change in the mean radius ΔR is measured and the hydrostatic stiffness $K_{\mathrm{H}}^{(\mathrm{MC})}$ is evaluated as [56]

$$K_{\mathrm{H}}^{(\mathrm{MC})} = \frac{\sum_n |\vec{F}_i^{(\mathrm{ext})}|}{\Delta R} \qquad (4.6)$$

with n being the number of atoms making up the fullerene. The results obtained for different fullerenes and the different parameter sets are shown in Table 4.5. Usually fullerenes are not perfectly spherical but rather have a polyhedral shape. To investigate the influence of the fullerene shape on the hydrostatic stiffness all atoms making-up the fullerenes are enforced to be located on a sphere during hydrostatic deformation, with the sphere possesing an undeformed radius $R^{(0)}$. The corresponding hydrostatic stiffness is denoted as $K_{\mathrm{H}}^{(\mathrm{MCS})}$.

The hydrostatic stiffness of carbon fullerenes $K_{\mathrm{H}}^{(\mathrm{MC})}$ becomes lower with increasing size of the fullerene and, thus, depends on the fullerene radius. However, the decrease in $K_{\mathrm{H}}^{(\mathrm{MC})}$ diminishes for larger fullerenes. The hydrostatic stiffness

$K_{\mathrm{H}}^{(\mathrm{MCS})}$ of the enforced spherical fullerenes is for the C60 fullerene almost equal to the corresponding value of $K_{\mathrm{H}}^{(\mathrm{MC})}$ and decreases only slightly with fullerene size. Hence, the difference $K_{\mathrm{H}}^{(\mathrm{MCS})} - K_{\mathrm{H}}^{(\mathrm{MC})}$ increases with fullerene size. This leads to the conclusions that C60 and probably also C240 can be considered as spheres without introducing a large error and that the decrease in $K_{\mathrm{H}}^{(\mathrm{MC})}$ is mainly due to the more faceted shape of larger fullerenes and not due to the increasing size. The hydrostatic stiffness is directly proportional to C and, therefore, all parameter sets should give reliable results, as all of them predict experimental values of C well. Surprisingly, set ES4 shows the best agreement with the MC results, although its membrane stiffness C is slightly lower than the experimental one. Generally, $K_{\mathrm{H}}^{(\mathrm{MC})}$ and $K_{\mathrm{H}}^{(\mathrm{MCS})}$ are overestimated by the continuum models, where ES1 and ES2 lead to the highest hydrostatic stiffness.

For a further comparison between the different parameter sets the critical hydrostatic pressure, i.e. the buckling pressure, of the fullerenes is evaluated. In the MC simulations a critical loading state is indicated by the collapse of the fullerene and, thus, can only be calculated for the faceted fullerenes. From the collapse load the critical pressure can be estimated as [56]

$$p_{\mathrm{H}}^{(\mathrm{MC})*} = \frac{n|\vec{\boldsymbol{F}}_{\mathrm{H}}^{(\mathrm{ext})}|}{A_0} \tag{4.7}$$

where $\vec{\boldsymbol{F}}_{\mathrm{H}}^{(\mathrm{ext})*}$ denotes the collapse force per atom and $A_0 = 4\pi(R^{(0)})^2$ is the mean surface area of the undeformed fullerene. The corresponding critical pressure for bifurcation buckling of a thin spherical shell as calculated from linear stability theory for shells reads [118]

$$p_{\mathrm{H}}^{*} = \frac{2Eh^2}{\sqrt{3(1 - \nu^2)}(R^{(0)})^2} \ . \tag{4.8}$$

This equation holds only for perfect spheres, thus the considerations regarding p_{H}^{*} are limited to C60 and C240. For larger fullerenes the assumption of perfect spheres is not permissible. The results obtained for the critical pressures are summarized in Table 4.6. Parameter sets which give a good representation of D also lead to meaningful results for the critical hydrostatic pressure. Sets ES3 and ES5 strongly overestimate D, and also strongly overestimate $p_{\mathrm{H}}^{(\mathrm{MC})*}$. Both, p_{H}^{*} and D strongly depend on the thickness h of the layers. This leads to the conclusions that, although sets ES3 and ES5 correctly model the membrane stiffness, their values of h are far to high and, hence the corresponding elastic moduli are to low. Especially, the assumption of the layer thickness being equal to the interlayer spacing of graphite (ES5), is not meaningful for simulations in which bending is involved.

As third load case a radial load applied as line load along the equator of the fullerenes is considered. Analytically the response of a perfect sphere to this radial

Table 4.6: Critical hydrostatic pressure of C60 and C240 obtained from MC simulations and analytical considerations (MC data from [56]).

Fullerene	$p_{\mathrm{H}}^{(\mathrm{MC})*}$ [GPa]	p_{H}^{*} [GPa] ES1	ES2	ES3	ES4	ES5
C60	276	224	254	424	282	1092
C240	63	56	63	106	70	272

load can be obtained as

$$\Delta R_{\mathrm{E}} = \frac{\left[\frac{3(1-\nu^2)(R^{(0)})^2}{h^2}\right]^{1/4} f^{\mathrm{E}} \ R^{(0)}}{2Eh} \tag{4.9}$$

with ΔR_{E} being the change of the radius at the equator. The force per unit length applied at the equator is denoted by f^{E}. Using a total force value as defined by $F^{\mathrm{E}} = 2\pi R^{(0)} f^{\mathrm{E}}$ instead of f^{E} in Equation (4.9), the ring load stiffness of a sphere can be evaluated as

$$K_{\mathrm{R}} = \frac{F^{\mathrm{E}}}{\Delta R_{\mathrm{E}}} = \frac{4\pi \ Eh}{\left[\frac{3(1-\nu^2)(R^{(0)})^2}{h^2}\right]^{1/4}} \ . \tag{4.10}$$

In contrast to the hydrostatic stiffness K_{H} the ring load stiffness K_{R} depends on the radius of the spheres. In the MC simulations the radial ring load is difficult to realize as the atoms are usually not exactly located along the equator, but are rather distributed in an area close to it, see Figure 4.1. Each atom i located within this area is subjected to a force $\vec{F}_i^{(\mathrm{ext})}$ pointing towards the center of mass of the fullerene. The corresponding ring load stiffness reads [56]

$$K_{\mathrm{R}}^{(\mathrm{MC})} = \frac{\sum_{n_{\mathrm{E}}} |\vec{F}_i^{(\mathrm{ext})}|}{1/n_{\mathrm{E}} \sum_{n_{\mathrm{E}}} |\Delta R_i|} \ , \tag{4.11}$$

with

$$\Delta R_i = R_i^{\mathrm{new}} - R_i^{\mathrm{old}} \ . \tag{4.12}$$

The quantities R_i^{new} and R_i^{old} are the distances between atom i and the fullerene's center of mass before and after the ring load is applied, respectively. The number of atoms in the equatorial area is denoted by n_{E}.

The values of the ring load stiffness obtained with the continuum model and the MC simulations, respectively, are shown in Table 4.7. On first sight, set ES3 gives the best representation of the ring load stiffness, as the values for C60 and C240 match the MC results almost perfectly. And also for C500 and C1280 the ring load stiffness is well predicted. However, in the case of C60 and C240, the ring load in the MC simulations is rather an area load than a line load, which was assumed in the continuum model. In the continuum model the load is more localized, which
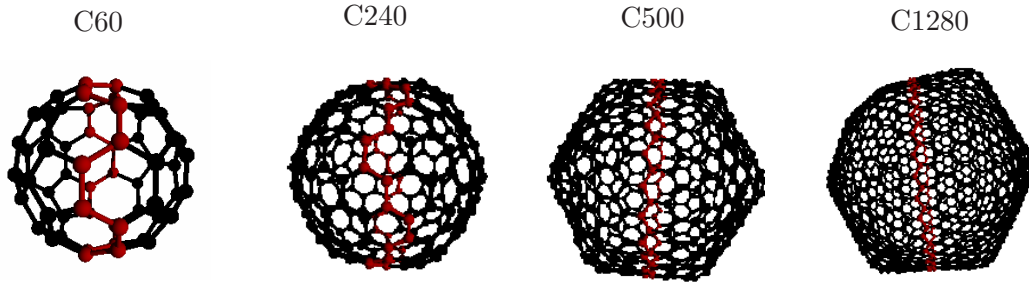
Figure 4.1: Defined equator (marked in red) for simulating the ring load in MC simulations. By courtesy of Markus A. Hartmann [56].

Table 4.7: Ring load stiffness of different fullerenes obtained from MC simulations and analytical considerations (MC data from [56]).

Fullerene	$K_{\mathrm{R}}^{(\mathrm{MC})}$ [N/m]	K_{H} [N/m] ES1	ES2	ES3	ES4	ES5
C60	2042	1508	1607	2003	1551	3277
C240	1394	1065	1136	1416	1095	2315
C500	1103	889	947	1180	914	1930
C1280	831	703	750	935	723	1529

should lead to larger displacements and, hence, to a lower ring load stiffness than observed in the MC simulations. Therefore, set ES3 actually overestimates the ring load stiffness. For larger fullerenes the ring load area decreases relative to the total surface area of the fullerene and approaches a sharp line for infinitely large fullerenes, see Figure 4.1. Thus, the continuum mechanical prediction of K_{R} should get better with increasing size of the fullerenes. This effect is captured by parameter sets ES1, ES2, and ES4, where ES2 gives the best representation of $K_{\mathrm{R}}^{(\mathrm{MC})}$ for the two largest fullerenes. As can be seen from Equation (4.10) the ring load stiffness also strongly depends on h. Again, set ES5 completely fails in predicting this stiffness, while ES3 again overestimates it. This observations confirm the conclusions drawn for the critical hydrostatic pressure.

Considering all three loading cases, ES2 and ES4 show the best agreement with the MC simulations. However, the membrane stiffness of graphene is not well predicted by ES4, thus ES2 is used in Chapter 7 to model the layers of carbon onions. As the hydrostatic stiffness of enforced spherical fullerenes is independent of the radius, all carbon layers can be modeled with the same properties.

ES1 slightly underestimates the mechanical properties of fullerenes but gives a good representation of the membrane and bending stiffness of a single graphene layer. This set is used to model the layer properties of graphene layers making up carbon crystallites investigated in Chapter 6. ES3 overestimates the bending stiff-

ness of a graphene layer, and thus also overestimates the critical pressure and ring load stiffness of the fullerenes. ES5 completely fails in predicting the mechanical behavior if bending of the layers is involved.

However, it should also be noted that sets ES3 and ES4 were derived in [130] for the same structure, but with different potentials describing the atom-atom interactions. The obtained elastic constants differ significantly, leading to different mechanical behavior of the corresponding continuum structure. A strong dependency of the elastic constants on the parameters used in the MD simulations is also observed in [177]. Hence, using other parameters in the MC simulations would lead to other results of these simulations and, therefore, to another choice of parameters for subsequent continuum mechanical simulations.

Nevertheless, it can be clearly stated that ES5 (and similar parameter sets) should not be used in continuum shell models, although this is often proposed in literature, see Table 4.1. This parameter set not simply overestimates the bending stiffness of graphene, the critical pressure, and ring load stiffness of fullerenes, but is completely off-target.

4.3   Remarks on the Elastic Constants

In the previous section fullerenes are modeled as thin elastic spherical shells. The mechanical properties of the shells are described using the elastic modulus E, the thickness of the layers h, and the Poisson's ratio ν. The atomic structures modeled as shells, however, consist of a single atomic layer. As already discussed in Section 4.1 the question about the physical meaning of the thickness of such layers arises. One hardly can argue that a single atomic layer possesses something like a thickness.

Thus, E, h, and ν have to be considered as "effective values", which give – in combination – a good representation of the membrane and bending stiffness of the atomic layers. They do not necessarily have a physical meaning as in bulk materials. Due to this fact, stress resultants in terms of section forces f_{kl} and section moments m_{kl} should be used instead of stresses σ_{kl} to describe the loading state of a single carbon layer. The stress resultants are related to the stresses by

$$f_{kl} = \int_{-h/2}^{h/2} \sigma_{kl}(z)\mathrm{d}z \tag{4.13}$$

$$m_{kl} = \int_{-h/2}^{h/2} \sigma_{kl}(z)z\mathrm{d}z \ , \tag{4.14}$$

where $k, l = x, y$. The coordinate z is transverse to the mid surface of the plate or shell. This concept is applied in Chapter 7 for describing the loading state of carbon onions.

4.4 Conclusions

To model carbon layers as thin elastic plates or shells the elastic modulus, the layer thickness and the Poisson's ratio are required as input parameters. The values of these parameters found in literature differ strongly. Often an elastic modulus of $\sim 1000\,\text{GPa}$ is derived from the membrane properties of a single graphene or nanotube layer, where the thickness of the layers is assumed to be equal to the interlayer spacing of graphite. It is shown that this combination of elastic modulus and layer thickness completely fails to predict the mechanical behavior of carbon structures when bending is involved, and thus should not be used in a continuum model.

For a good representation of the bending stiffness in combination with the proper membrane stiffness, the thickness of the layer must be below or close to $0.1\,\text{nm}$, and consequently, the elastic modulus must be far larger than $1000\,\text{GPa}$. Parameter sets fulfilling these criteria also give good approximation of the membrane stiffness of graphene. The ring load stiffnesses (radial loading along the equator of fullerenes considered as spheres) and the values of the critical pressures for buckling of spherical fullerenes obtained with these sets in combination with analytical continuum models are in good agreement with results obtained by MC simulations. The parameters E, h, ν are derived from MD simulations and, hence, depend on the potentials and parameters used in these simulations. Consequently, no clear statement can be given which parameter set is the "correct" one.

As long as pure membrane loading is considered continuum shell models give qualitatively and also quantitatively reliable results, as all shell parameter sets give almost the same membrane stiffness. If bending gets involved reliable qualitative results can be achieved with data sets fulfilling the above criteria. The quantitative results have to be considered with care, as the bending stiffness of the shells strongly depends on the shell parameters used and thus, on the underlying MD simulations conducted for evaluating these shell parameters.

Chapter 5

Continuum van der Waals Models for Multi-Layer Carbon Nanostructures

5.1 Introduction

For multi-layer carbon nanostructures like graphite, MWCNTs, or carbon onions the van der Waals (vdW) interactions between neighboring layers must be considered in addition to the in-plane covalent bonds. From an atomistic point of view the vdW interactions between two layers result from vdW interactions between discrete atoms forming the layers. These atom-atom interactions, however, are not applicable to continuum mechanical models for which a pressure-distance relation is required. Appropriate continuum vdW models for different carbon nanostructures can be found in the literature, see e.g., [60, 72, 98, 145]. Some of these models are discussed in this Chapter, where special emphasis is placed on the continuum model for spherical nanostructures.

5.2 Van der Waals Interactions between discrete Atoms

VdW interactions are non-local interactions between un-charged atoms or molecules and are relatively weak compared to covalent or ionic bonds. The non-local interactions between two atoms can be described using a pair potential

$$U_{12}(r) = \left(\frac{k}{k-l} \right) \left(\frac{k}{l} \right)^{l/(k-l)} \epsilon \left[\left(\frac{\sigma}{r} \right)^k - \left(\frac{\sigma}{r} \right)^l \right], \qquad (5.1)$$

where $k, l \in \mathbb{N}$ see, e.g., [105]. In Equation (5.1) r is the current distance between the two interacting atoms, σ describes the distance at $U_{12} = 0$, and ϵ accounts for the depth of the potential well. Both σ and ϵ depend on the kind of interacting atoms. The pair potential U_{12} consists of an attractive part $U_{\text{atr}} = -\left(\frac{\sigma}{r}\right)^l$ and a repulsive part $U_{\text{rep}} = \left(\frac{\sigma}{r}\right)^k$. According to the London-equation [93] the weak attractive interaction between two atoms vanishes with the 6-th power leading to $l = 6$. For the repulsive part $k = 12$ is chosen for practical reasons and has no physical meaning. With $l = 6$ and $k = 12$ Equation (5.1) simplifies to

$$U_{12} = 4\epsilon \left[\left(\frac{\sigma}{r}\right)^{12} - \left(\frac{\sigma}{r}\right)^6 \right] , \tag{5.2}$$

being equal to the Lennard-Jones (LJ) potential, see, e.g., [72]. In the following the LJ potential is used to describe the vdW interactions.

The first derivative of the LJ-potential U_{12} with respect to the distance r gives the forces acting on the individual atoms

$$F_{12} = \frac{d\,U_{12}}{dr} = -\frac{4\epsilon}{r} \left[6 \left(\frac{\sigma}{r}\right)^6 - 12 \left(\frac{\sigma}{r}\right)^{12} \right] \tag{5.3}$$

where the attractive forces are assumed to be positive. At the equilibrium distance of the atoms the forces on the atoms must vanish, i.e., the potential has its minimum value. With $\frac{d\,U_{12}}{dr} = F_{12} = 0$ the equilibrium distance, r_0, can be calculated as

$$r_0 = 2^{1/6}\,\sigma. \tag{5.4}$$

Figure 5.1 illustrates the LJ potential U_{12} and the resulting inter-atomic force for two interacting carbon atoms ($\sigma = 0.3415\,\text{nm}$ and $\epsilon = 0.00239\,\text{eV}$, see, e.g., [98]) as a function of the atom-atom distance r. For distances smaller than the equilibrium distance $r_0 = 0.3833\,\text{nm}$ the absolute value of the interaction force increases fast with decreasing r, being a result of the large exponent $n = 12$ of the repulsive part U_{rep} in the pair-potential U_{12}. For distances r larger than r_0 the atoms are attracted to each other, where the absolute values of the attractive forces are small compared to the repulsive ones. The attractive forces vanish relatively fast with increasing r. Although, the attractive forces become zero for $r \to \infty$, only, they are often treated as negligible for large distances ($\approx r > 1.0\,\text{nm}$), see, e.g. [72].

5.3 Continuum Models for Planar Nanostructures

Graphite and carbon crystallites are planar nanostructures where vdW interactions are active between adjacent layers. In the case of planar nanostructures formed by layers of infinite size it is justified to assume that neighboring layers consist of the same number of atoms. Thus, each atom of a layer interacts with the same
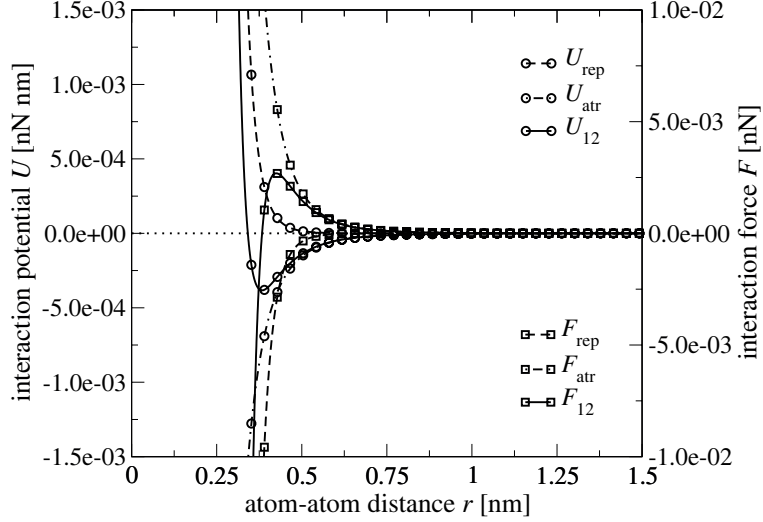
Figure 5.1: Van der Waals interaction potential U and interaction force F of two interacting carbon atoms.

number of atoms on the neighboring layer, leading to equal vdW forces acting on each atom. Based on this assumption a continuum vdW model in the form of a pressure-distance relation is derived in [72] by summing up all vdW interactions between atoms on two neighboring layers, resulting in

$$p(\alpha) = \frac{C_{33}}{6} \left[\left(\frac{\sigma}{\alpha} \right)^{10} - \left(\frac{\sigma}{\alpha} \right)^{4} \right] \tag{5.5}$$

The compressive constant C_{33} is given in [72] as $36.5\,\text{GPa}$ and has been confirmed experimentally in [183]. σ is a LJ-parameter, see Section 5.2, and α is the current interlayer distance. Two neighboring layers reach their equilibrium distance α_{eq} if the condition $p(\alpha = \alpha_{\text{eq}}) = 0$ is satisfied, leading to

$$\alpha_{\text{eq}} = \sigma \; . \tag{5.6}$$

The equilibrium interlayer distance α_{eq}, thus is smaller than the equilibrium distance of two atoms by a factor $2^{1/6}$, see Equation (5.4).

Another possible way of obtaining a pressure-distance relation for planar nanostructures is to replace the discrete sum by a surface integral and use the atom area density, i.e. the atoms per unit area, to describe the number of atoms in an infinitesimally small area of the layers, see e.g. [55, 98, 145]. To avoid boundary effects due to non-saturated atoms at the edges, it is assumed that both layers are infinite in their size. In planar carbon nanostructures the atoms in the individual layers have a hexagonal arrangement with an atom-atom bond length

$a^{(0)} = a_{C-C} \approx 0.142 \, \text{nm}$. Thus, the atom area density, ρ_∞, reads

$$\rho_\infty = \frac{4}{3\sqrt{3} \, a_{C-C}^2} \tag{5.7}$$

Two atoms on two adjacent layers with an atom-atom distance r interact with each other with a vdW force F_{12}, given by Equation (5.3). Assuming that the atom on layer 1 is located at (0,0,0) and that the atom on layer 2 has the position (x,y,α) (Figure 5.2), the atom-atom distance is given by

$$r = \sqrt{x^2 + y^2 + \alpha^2} \, . \tag{5.8}$$

Only the components of F_{12} which are normal to the surfaces of the layer contribute to the vdW pressure and therefore, only these components are considered in the following. These normal components can be estimated as

$$F_{1N} = -F_{12} \sin(\beta) = F_{12} \frac{\alpha}{r}$$
$$F_{2N} = -F_{12} \sin(\beta) = F_{12} \frac{\alpha}{r} \tag{5.9}$$

where F_{iN} acts on one atom in the i-th layer (positive for repulsion). By employing the atom area density the following expressions for the total normal forces acting on infinitesimally small areas of layer 1 and 2, dA_1 and dA_2, respectively, are obtained

$$\mathcal{F}_1 = \rho_\infty \, dA_1 \int_{-\infty}^{\infty} \rho_\infty \, F_{1N} \, dx \, dy$$
$$\mathcal{F}_2 = \rho_\infty \, dA_2 \int_{-\infty}^{\infty} \rho_\infty \, F_{2N} \, dx \, dy \tag{5.10}$$

where $\mathcal{F}_i$ includes the vdW interactions of all atoms located on dA_i with all atoms on the adjacent layer. From Equation (5.10) it can be seen that for $dA_1 = dA_2$ the normal forces acting on dA_1 and dA_2 are equivalent. Therefore, the resulting vdW pressure acting on layer 1 and 2 must be equivalent, too. Inserting Equation (5.9) into Equation (5.10) under consideration of Equation (5.3) yields

$$p(\alpha) = C_0 \left[\left(\frac{\sigma}{\alpha} \right)^{11} - \left(\frac{\sigma}{\alpha} \right)^5 \right] \tag{5.11}$$
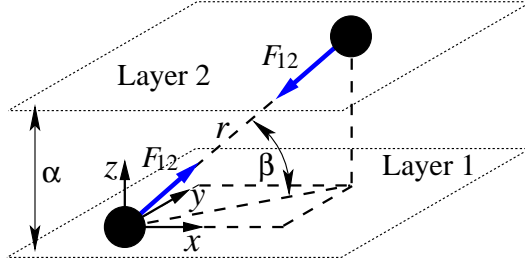
for the vdW pressure between layer 1 and 2 as function of the interlayer distance α (positive for repulsion) with

$$C_0 = 8 \, \epsilon \, (\rho_\infty)^2 \, \sigma \, \pi \, . \tag{5.12}$$

With $p(\alpha_{eq}) = 0$ the equilibrium distance can be calculated as

$$\alpha_{eq} = \sigma, \tag{5.13}$$

Figure 5.2: Two-layer planar nanoparticle with interlayer distance α.

being equal to the inter layer distance observed for the model given by Equation (5.5).

For Equation (5.5) the constant parameter $\frac{C_{33}}{6}$ has a value of 6.08 GPa [72], whereas for Equation (5.11) the parameter C_0 depends on the values chosen for ϵ and σ. If the values given in [98] ($\sigma = 0.3415$ nm, $\epsilon = 0.00239$ eV) are used a value of 4.79 GPa is obtained for C_0, which is quite different from $\frac{C_{33}}{6}$. For the values given in [176] ($\sigma = 0.3345$ nm, $\epsilon = 0.00319$ eV) the value for C_0 is calculated as 6.25 GPa, being quite close to $\frac{C_{33}}{6}$. The experimental results of [183] show that it is more likely that C_0 is around 6 GPa. With appropriately chosen parameters for σ and ϵ, the constant C_0 can be adapted to experimental observation. More problematic seems the fact that there is a difference between the exponents of Equation (5.5) and Equation (5.11):

$$\underbrace{C_1 \left[()^{10} - ()^4\right]}_{(5.5)} \neq \underbrace{C_0 \left[()^{11} - ()^5\right]}_{(5.11)} . \tag{5.14}$$

It is not clear how strong this difference in the exponents influences the results for multi-layer structures. However, both equations lead to the same equilibrium distance as long as the same value for σ is chosen.

5.4 Continuum Models in Simply Curved Nanostructures

The class of simply curved nanostructures consists of carbon nanotubes and multi-walled carbon nanotubes (MWCNT), where vdW interactions are of importance only for the latter. For curved nanostructures the number of atoms forming each layer is different for neighboring layers. This difference in the number of atoms has to be considered in the continuum mechanical formulation of the vdW interactions to obtain an accurate representation of the vdW pressures on opposite faces of neighboring layers.

The pressure-distance relation given by Equation (5.5) [72] is used, e.g., in [114, 170] to describe the vdW interactions in MWCNTs. However, this relation

has been derived for graphene [72] and, thus, does not account for the different numbers of atoms in neighboring layers. Nevertheless, it allows a straightforward implementation in standard finite element codes to access finite element solutions for the mechanical behavior of carbon nanotubes. As long as the radii of the MWCNT walls are sufficiently large this method gives reliable results.

One method for including the curvature effect is to assume that the vdW pressure on opposite faces of adjacent layers is inversely proportional to their radii, leading to $p_{\text{in}}R_{\text{in}} = p_{\text{out}}R_{\text{out}}$, see ,e.g., [60, 122, 161].

In [98] pressure-radius relations are derived analytically from the LJ-potential (Equation (5.2)) without any of the above assumptions. A short review of the derivations made in [98] is given in the following. In [98] a double-wall nanotube is used for deriving the pressure distance relations, where R_1 and R_2 are the radii of the inner and outer nanotubes, respectively. Using cylindrical coordinates $(R_i, \theta, z, i = 1, 2)$ the distance between two atoms on the inner layer and on the outer layer, respectively, can be given as

$$r = \sqrt{R_1^2 + R_2^2 - 2R_1R_2\cos\theta + z^2}. \tag{5.15}$$

The vdW force $F(r)$ between these two atoms can be calculated according to Equation (5.3), where only the radial components $F_{i\text{R}}$ $(i = 1, 2)$ of this force contribute to the vdW pressure. By employing the atom area density ρ_∞ the forces acting on infinitesimally small areas of the inner and outer nanotube can be calculated as

$$F_1 = \rho_\infty \, dA_1 \int_{A_2} F_{1\text{R}} \, \rho_\infty \, dA_2 \tag{5.16}$$

and

$$F_2 = \rho_\infty \, dA_2 \int_{A_1} F_{1\text{R}} \, \rho_\infty \, dA_1, \tag{5.17}$$

respectively, where dA_i is an infinitesimally small area of the i-th nanotube. With Equations (5.16) and (5.17) the vdW pressures acting on the nanotube wall are finally obtained as

$$p_1 = C_0 \frac{R_2}{R_1} \left[231 \left(\frac{\sigma}{R_1 + R_2} \right)^{11} \left(\frac{R_2 - R_1}{R_2 + R_1} E_{13} - E_{11} \right) \right.$$
$$\left. -160 \left(\frac{\sigma}{R_1 + R_2} \right)^{5} \left(\frac{R_2 - R_1}{R_2 + R_1} E_7 - E_5 \right) \right], \tag{5.18}$$

$$p_2 = C_0 \frac{R_1}{R_2} \left[231 \left(\frac{\sigma}{R_1 + R_2} \right)^{11} \left(\frac{R_2 - R_1}{R_2 + R_1} E_{13} + E_{11} \right) \right.$$
$$\left. -160 \left(\frac{\sigma}{R_1 + R_2} \right)^{5} \left(\frac{R_2 - R_1}{R_2 + R_1} E_7 + E_5 \right) \right] \tag{5.19}$$

with

$$C_0 = \frac{3\pi}{32}\epsilon\sigma\rho_\infty^2 \tag{5.20}$$

The parameters E_{13}, E_{11}, E_7, E_5 denote integrals involving R_1, R_2, and the circumferential angle θ and can be led back to elliptic integrals. For more details see, [98]. From Equations (5.18) and (5.19) it can be seen that neither $p_1 = p_2$ nor $p_1 R_1 = p_2 R_2$ are satisfied by the vdW pressures acting on the nanotube walls. In [98] the obtained relations are then used to investigate buckling of double-layer carbon nanotubes under external pressure. It is shown that – compared to the results obtained with the derived vdW interaction pressures – the critical pressure is overestimated by 25% if $p_1 R_1 = p_2 R_2$ is assumed for the vdW pressures and by 75% if the relation $p_1 = p_2$ is used. The results illustrate that accounting for the different number of atoms in adjacent layers is of great importance in the formulation of the vdW model, especially if the stability of multi-layer structures is studied.

5.5   Continuum Model for Spherical Nanostructures

Carbon onions and multi-layer fullerenes are typical doubly-curved multi-layer nanostructures. For these kinds of nanostructures the difference in the number of atoms forming neighboring layers is even more strongly pronounced than in simply curved nanostructures. Similar to the work [98] an appropriate vdW pressure-distance relation can be obtained by integrating the vdW interactions over the surfaces of neighboring layers using an atom area density. In literature different attempts can be found to describe the vdW interaction between spherical particles using this atom density approach. One of the first studies dates back to Hamaker in 1937 [55], in which the vdW attraction between two spherical particles is investigated. In [55] the particles are considered as solid and only the attractive part of the vdW potential is used, i.e., the London-vdW forces [93]. Although the case of hollow concentric particles is not treated in [55] the basic ideas of using an atom density and integrating over the particle volume become clearly visible.

The case of rigid hollow nanostructures is investigated in [67], where concentric configurations as well as configurations with separated particles are studied. For multi-layer doubly curved nano-structures only the concentric configuration is of importance and only this case is discussed further. The atom-atom pair potential used in [67] reads

$$U_{12} = \sum_{k=6,12} (-1)^{k/2} \, A_k / r_{ij}^k \tag{5.21}$$

where A_k are Lennard-Jones parameters and r_{ij} is the distance between atoms j and i. The potential given in Equation (5.21) is equal to the Lennard-Jones

potential given in Equation (5.2) with $A_i = 4\epsilon \ \sigma^i$. In [67] the total interaction potential is obtained by summing up all interactions between the atoms of the inner and the outer layers leading – for the special case of concentric spherical layers – to

$$V_{n_1 n_2} = \sum_{k=6,12} (-1)^{k/2} \frac{n_1 \ n_2 \ A_k}{2 \ (k-2) \ R_1^k \ b} \left[\frac{1}{(b-1)^{k-2}} - \frac{1}{(b+1)^{k-2}} \right] \qquad (5.22)$$

with n_i being the number of atoms forming layer $i = 1, 2$. The quantity $b = \frac{R_2}{R_1}$ describes the relation between the radii of the outer and inner layers, R_2 and R_1, respectively. With the atom area density, ρ_∞, the number of atoms in each layer can be expressed as

$$n_i = \rho_\infty \ 4 \ \pi \ R_i^2 \qquad (5.23)$$

and Equation (5.22) can be re-formulated as

$$V_{n_1 n_2} = C_1 \left[\frac{E_1 \sigma^{10}}{(R_1^2 - R_2^2)^{10}} - \frac{E_2 \sigma^4}{(R_1^2 - R_2^2)^4} \right] \ , \qquad (5.24)$$

where

$$\begin{aligned} C_1 &= \frac{64}{5} \ R_1^2 \ R_2^2 \ (\rho_\infty)^2 \ \epsilon \ \sigma^2 \pi^2, & (5.25) \\ E_1 &= 5R_1^8 + 60R_1^6 R_2^2 + 126R_1^4 R_2^4 + 60R_1^2 R_2^6 + R_2^8 \ , \\ E_2 &= 5 \left(R_1^2 + R_2^2 \right) \ . & (5.26) \end{aligned}$$

In [67] the layers are treated as rigid, so the vdW interactions do not lead to any deformation. The vdW interaction potential given in Equation (5.22) is, however, not applicable in a continuum mechanical description of a multi-layer spherical system where the deformations of the system are of interest as well. An appropriate vdW pressure-distance relation was derived in the present thesis' project and is presented in the following sections of this chapter. Furthermore, equilibrium configurations of different two-layer systems were estimated. The results were published in [145], too.

5.5.1 Remarks On the Atom Area Density of Doubly-Curved Carbon Nanopstructures

As mentioned above the vdW interaction potential and the vdW pressure distance relation for doubly-curved nanostructures can be derived by integrating over all atom-atom interactions between atoms on two neighboring layers. The number of atoms in each layer can be described using an atom area density

$$\rho^{(0)} = \frac{n}{4\pi (R^{(0)})^2} \ , \qquad (5.27)$$

where n is the number of atoms in the layer and $R^{(0)}$ is the radius of the undeformed layer. In [157] it is shown that the radius $R^{(0)}$ depends on n by

$$R^{(0)} = a^{(0)}(0.103374\ n - 0.424548)^{0.5}\ . \tag{5.28}$$

The parameter $a^{(0)}$ is the covalent atom-atom bond length. Replacing $R^{(0)}$ in Equation (5.27) by Equation (5.28) leads to

$$\rho^{(0)} = \frac{n}{4\pi\ (0.103374\ n - 0.424548)\ (a^{(0)})^2}\ . \tag{5.29}$$

From Equation (5.29) it is clearly visible that $\rho^{(0)}$ depends on the number of atoms forming a layer and thus on the size of the layer.

In the following only carbon nanostructures are considered with a covalent carbon-carbon bond length $a^{(0)} = a_{C-C} = 0.142\,\text{nm}$ .The relation between $\rho^{(0)}$ and the layer size (in terms of $R^{(0)}$) for spherical carbon nanostructures is shown in Figure 5.3. The atom density increases fast for small nanostructures with $R^{(0)} < 1.0\,\text{nm}$ and decreases slowly for $R^{(0)} > 1.0\,\text{nm}$. The limiting value of the atom density can be calculated using Equation (5.29) where it is assumed that for $R^{(0)} \to \infty$ also $n \to \infty$, and thus

$$\begin{aligned}
\rho^{(0)}(n \to \infty) &= \frac{1}{0.103374\ (a^{(0)})^2\ 4\pi} \approx \\
&\approx \frac{4}{3\sqrt{3}\ (a^{(0)})^2} = \rho_\infty\ . \tag{5.30}
\end{aligned}$$

where $\frac{4}{3\sqrt{3}\ (a^{(0)})^2}$ is the atom area density of graphite, see Section 5.3.

Figure (5.3) shows that for large layer radii ($R^{(0)} > 1.0\,\text{nm}$) the atom density of plane graphene can be used to account for the number of atoms in the layers as the relative deviation $\frac{\rho^{(0)} - \rho_\infty}{\rho_\infty}$ is smaller than 1%. For small radii it seems to be necessary to use the actual density $\rho^{(0)}$. The smallest layer that may occur in a multi-layer doubly-curved structure is the C60 fullerene. This fullerene consists of 60 atoms which are arranged in hexagonal and pentagonal rings. With Equations (5.28) and (5.29) the radius and the atom density of C60 can be calculated as $0.3413\,\text{nm}$ and $40.982\,\text{atoms/nm}^2$, respectively. This density is about 7% higher than the atom density of graphite. For C240 ($R^{(0)} = 0.7012\,\text{nm}$) an atom area density $R^{(0)} = 38.84\,\text{atoms/nm}^2$ is obtained, leading to a relative deviation to the density of graphite of about 1.8%. This deviation can already be considered as negligible. Therefore, the actual atom area density has to be considered only for fullerenes being smaller than C240.

5.5.2 Derivation of the Pressure-Radius Relation

In the following only the case of concentrically nested two-layer spherical nanostructures is considered. The distance, r, between two atoms on neighboring layers
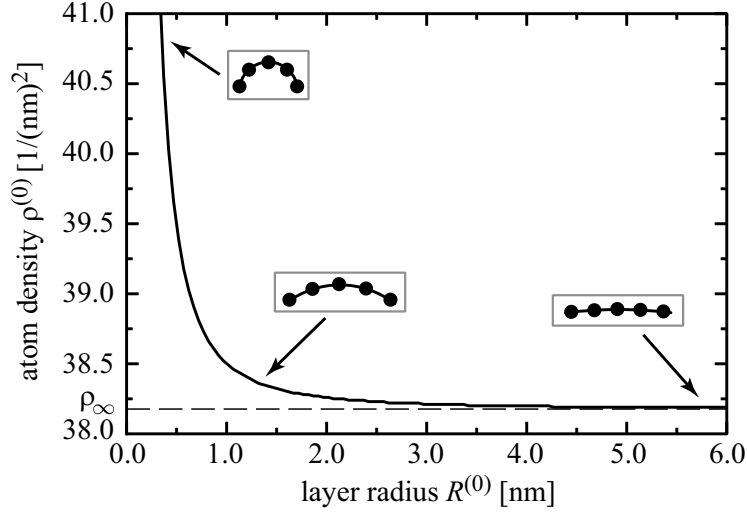
Figure 5.3: Dependency of the atom area density $\rho^{(0)}$ on the on the radius, $R^{(0)}$, of the spherical layers [145].

is a function of the current radii of the inner and outer layer, R_1 and R_2, respectively and reads

$$r = \sqrt{R_1^2 + R_2^2 - 2R_1R_2\sin(\theta)\cos(\gamma)} \ , \tag{5.31}$$

where the angles θ and γ describe the position of the considered atom on the outer layer relative to the interacting atom on the inner layer, see Figure 5.4. The two atoms attract/repel each other with a vdW force F_{12} given in Equation (5.3). Only the radial components of F_{12} contribute to the vdW pressure and thus, the other components are neglected in the following. The radial components of F_{12} acting on the atoms on the inner and outer layer F_1 and F_2, respectively, can be calculated as

$$F_1 \;=\; \frac{F_{12}}{r}[R_2\sin(\theta)\cos(\gamma) - R_1] \ , \tag{5.32}$$

$$F_2 \;=\; \frac{F_{12}}{r}[R_2 - R_1\sin(\theta)\cos(\gamma)] \ . \tag{5.33}$$

The total force $\mathcal{F}_1$ acting on one atom of the inner layer is the sum of forces due to vdW interactions with all atoms of the outer layer. Using the atom area density ρ_∞ the sum over the discrete atoms can be replaced by an integral over the surface of the outer layer, thus, $\mathcal{F}_1$ can be calculated as

$$\mathcal{F}_1 = \rho_\infty \int\limits_{A_2^{(0)}} F_1 \ \mathrm{d}A_2^{(0)} \ . \tag{5.34}$$
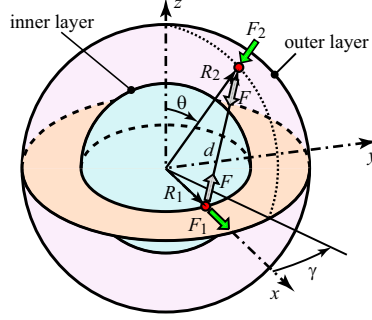
Figure 5.4: Double-layer carbon onion [145].

where F_1 is given by Equation (5.32). The vdW pressure p_1 acting on the inner layer can now be obtained as

$$p_1 = -\frac{(\rho_\infty)}{A_1} \int\limits_{A_1^{(0)}} \mathcal{F}_1 \, dA_1^{(0)} \, , \tag{5.35}$$

where the integral

$$-(\rho_\infty) \int\limits_{A_1^{(0)}} \mathcal{F}_1 \, dA_1^{(0)} \, , \tag{5.36}$$

represents the total force acting on the inner layer due to vdW interactions of all atoms of the inner layer with all atoms of the outer layer. The surface of the deformed layer A_1 on which the total force acts can be calculated as

$$A_1 = 4\pi \, R_1^2 \, ,$$

It should be noted that the integrals

$$\tag{5.37}$$

$$\int\limits_{A_2^{(0)}} [\,] \, dA_2^{(0)} = \int\limits_0^\pi \int\limits_0^{2\pi} (R_2^{(0)})^2 \sin(\theta) \, [\,] \, d\gamma d\theta \, ,$$

$$\int\limits_{A_1^{(0)}} [\,] \, dA_1^{(0)} = \int\limits_0^\pi \int\limits_0^{2\pi} (R_1^{(0)})^2 \sin(\theta) \, [\,] \, d\gamma d\theta \, .$$

occurring in Equations (5.34) and (5.35) are performed over the initial, i.e., the undeformed layers - represented by $A_1^{(0)}$ and $A_2^{(0)}$. Integrating over the deformed surfaces of the layers A_1 and A_2 in combination with a constant atom density ρ_∞ would lead to deformation dependent numbers of atoms in the layers, what

would introduce an error. Adding or removing atoms from the layers is equal to
adding or removing energy from the two-layer system. If this change in energy is
not accounted for in the model, e.g. by introducing an energy source or sink, a
non-conservative mechanical system, and hence, an erroneous mechanical model
would be obtained. Similar to p_1 the vdW pressure acting on the outer layer, p_2
can be calculated as

$$p_2 = \frac{(\rho_\infty)^2}{A_2} \int\limits_{A_2^{(0)}} \left(\int\limits_{A_1^{(0)}} F_2 \; \mathrm{d}A_1^{(0)} \right) \; \mathrm{d}A_2^{(0)} \; . \tag{5.38}$$

Inserting Equations (5.31)–(5.33) into Equations (5.35) and (5.40) leads to a set
of elliptic integrals, which after some lengthy analytical manipulations, yield

$$p_1 = \frac{1}{R_1} C_0 \left[\frac{2 \; E_{11} \; \sigma^{11}}{(R_2^2 - R_1^2)^{11}} - \frac{5 \; E_{12} \; \sigma^5}{(R_2^2 - R_1^2)^5} \right] \; , \tag{5.39}$$

$$p_2 = \frac{1}{R_2} C_0 \left[\frac{5 \; E_{21} \; \sigma^5}{(R_2^2 - R_1^2)^5} - \frac{2 \; E_{22} \; \sigma^{11}}{(R_2^2 - R_1^2)^{11}} \right] \; , \tag{5.40}$$

with

$$
\begin{align}
E_{11} &= 15R_1^8 + 220R_1^6R_2^2 + 594R_1^4R_2^4 + 396R_1^2R_2^6 + 55R_2^8 \; , \tag{5.41} \\
E_{12} &= 3R_1^2 + 5R_2^2 \; , \tag{5.42} \\
E_{21} &= 3R_2^2 + 5R_1^2 \; , \tag{5.43} \\
E_{22} &= 15R_2^8 + 220R_2^6R_1^2 + 594R_2^4R_1^4 + 396R_2^2R_1^6 + 55R_1^8 \; , \tag{5.44}
\end{align}
$$

and

$$C_0 = \frac{32}{5} \; (R_1^{(0)})^2 \; (R_2^{(0)})^2 \; (\rho_\infty)^2 \; \epsilon \; \pi \; \sigma \; . \tag{5.45}$$

As discussed in Section 5.5.1, using ρ_∞ to describe the number of atoms in the
individual layers is also valid for small layer radii. To compare the derived result
for doubly-curved nanostructures with those used for planar structures given in
Section 5.3 the limiting case $R_1^{(0)} \to \infty$ is considered. With $R_2 = R_1 + \alpha$ and
$R_1 = R_1^{(0)} + \Delta R_1$ the vdW pressures p_1 and p_2 approach

$$\lim_{R_1^{(0)} \to \infty} (p_1) = - \lim_{R_1^{(0)} \to \infty} (p_2) = p_\mathrm{G} = E_\mathrm{G} \left[\left(\frac{\sigma}{\alpha} \right)^{11} - \left(\frac{\sigma}{\alpha} \right)^5 \right] . \tag{5.46}$$

where α is the interlayer distance, ΔR_1 is the change in the layer radius due
to deformation, and $E_\mathrm{G} = 8\epsilon \; (\rho_\infty)^2 \; \sigma \; \pi$. Equation (5.46) is equal to Equation
(5.11) derived in Section 5.3. Figure 5.5 shows the pressure p_1 on the inner layer
as function of the interlayer distance α for Equations (5.5), (5.11), and (5.39),
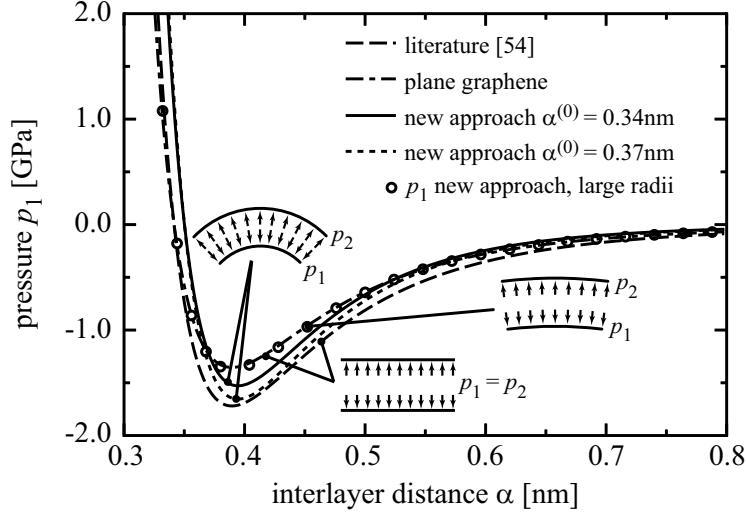
Figure 5.5: Comparison between the pressure-distance relation of the current approach with the pressure-distance relation for plane graphene (Eqn. (5.11)) and the pressure-distance relation (Eqn. (5.5)) given in the literature [72]. Figure also presented in [145].

where the values for graphite ($\sigma = 0.3415\,\text{nm}$ and $\epsilon = 0.00239\,\text{eV}$) are used for the Lennard-Jones parameters. For the sake of simplicity it is assumed that $R_1 = R_1^{(0)} = 0.40\,\text{nm} = \text{const}$, implying that only the outer layer is deformable. The reference radius of the outer layer is calculated as $R_2^{(0)} = R_1^{(0)} + \alpha^{(0)}$, where distances $\alpha^{(0)}$ of $0.34\,\text{nm}$ and $0.37\,\text{nm}$ are assumed, respectively.

The pressure p_1 obtained with the new approach given by Equation (5.39) strongly differs from the results estimated with Equations (5.5) and (5.11) representing the vdW interactions in plane graphene. The pressure in doubly-curved nanostructures depends on the initial interlayer distance $\alpha^{(0)}$ as $\alpha^{(0)}$ determines the radius of the outer layer and thus the number of atoms forming this layer. The number of atoms has a direct influence on the number of vdW interactions between the layers and thus on the resulting vdW pressure. For large layer radii ($R_1^{(0)} \gg 1.0\,\text{nm}$) Equation (5.39) gives almost the same results as Equation (5.11), as already shown in Equation (5.5).

5.5.3   Equilibrium Configuration

Equations (5.39) and (5.40) describe the vdW pressures on opposite faces of two neighboring layers. Additionally to the vdW pressures also the equilibrium distance between the layers is of interest. To evaluate the equilibrium radii of the layers, and, hence, their equilibrium distance the theorem of stationarity of the potential energy is used. The potential energy due to the vdW interactions V_T is

equal to the sum of all vdW interaction potentials between all atoms of the inner layer with all atoms of the outer layer. Employing the atom area density ρ_∞ and replacing the sum by surface integrals leads to

$$V_T = (\rho_\infty)^2 \int\limits_{A_1^{(0)}} \left(\int\limits_{A_2^{(0)}} V \, dA_2^{(0)} \right) dA_1^{(0)} . \tag{5.47}$$

where V is the Lennard-Jones potential given in Equation (5.2). Again, the integrations have to be performed over the surfaces of the undeformed layers represented by $R_1^{(0)}$ and $R_2^{(0)}$ resulting in

$$V_T = C_1 \left[\frac{E_1 \sigma^{10}}{\left(R_1^2 - R_2^2\right)^{10}} - \frac{E_2 \sigma^4}{\left(R_1^2 - R_2^2\right)^4} \right] , \tag{5.48}$$

where

$$C_1 = \frac{64}{5} (R_1^{(0)})^2 (R_2^{(0)})^2 (\rho_\infty)^2 \varepsilon \, \sigma^2 \pi^2, \tag{5.49}$$

$$E_1 = 5R_1^8 + 60R_1^6 R_2^2 + 126R_1^4 R_2^4 + 60R_1^2 R_2^6 + R_2^8 , \tag{5.50}$$

$$E_2 = 5\left(R_1^2 + R_2^2\right) . \tag{5.51}$$

The vdW potential V_T is symmetric with respect to R_1 and R_2 and thus the system can be characterized as conservative. Equation (5.48) is equal to Equation (5.22) describing the interaction between two rigid doubly-curved layers. To account for the deformation of the layers the strain energy of both layers must be included in the total potential energy, Π. The individual layers of the onion can be modeled as thin shells with membrane stiffness $\sim Eh$, bending stiffness $\sim Eh^3$, and Poisson's ratio ν, for details see Chapter 4. The membrane stiffness of a single layer in terms of a force–displacement relation is given by $k_S = \frac{4\pi \, R_i^2 \, p_i}{\Delta R_i} = \frac{8Eh\pi}{1-\nu}$ where p_i is the pressure acting on layer i. It follows that k_S does not depend on the layer radius and, thus, the strain energy of a deformed layer can be written as

$$U_i = \frac{1}{2} k_S (\Delta R_i)^2 , \tag{5.52}$$

where $\Delta R_i = R_i - R_i^{(0)}$ is the radial deformation of layer i. Considering the strain energy of both layers $(i = 1, 2)$ of the double-layer system leads to a total potential energy of

$$\Pi = V_T + U_1 + U_2 . \tag{5.53}$$

Contributions resulting from an initial curvature-induced excess surface energy, discussed e.g. in [63] are not considered in this formulation. Applying the theorem of stationarity of the potential energy yields

Table 5.1: Reference configuration of two nested fullerenes. $R_1^{(0)}$, $R_2^{(0)}$ are the reference radii of the inner and outer fullerene, respectively. $\alpha^{(0)}$ is the reference distance between the fullerenes and ρ_1, ρ_2 are the atom densities of the inner and outer fullerene, respectively. Data from [145].

	$R_1^{(0)}$ [nm]	$R_2^{(0)}$ [nm]	$\alpha^{(0)}$ [nm]	ρ_1 [1/nm^2]	ρ_2 [1/nm^2]
C60 in C180	0.35139	0.60990	0.25851	38.67	38.51
C60 in C240	0.35139	0.70364	0.35225	38.67	38.57

$$\frac{\partial \Pi}{\partial R_1} = 0 \quad \text{and} \quad \frac{\partial \Pi}{\partial R_2} = 0 \ . \tag{5.54}$$

Equations (5.54) represent two nonlinear equations for the two unknowns R_1 and R_2, and hence, for $\alpha = R_2 - R_1$.

5.5.4 Validation of the Model

For the validation of the continuum vdW model two different nested double-layer fullerenes are considered where their initial configurations are given in Table 5.1. The equilibrium radii and interlayer distances are obtained by solving Equation (5.54) and the results are compared to those of MC simulations.

For the continuum model of the nested fullerene a membrane stiffness $Eh = 363\,\text{J/m}^2$ and a Poisson's ratio $\nu = 0.19$ is assumed for each layer [114], leading to $k_S = 11263.2\,\text{J/m}^2$. In the MC simulations an equilibrium bond length $r_0 = 1.418\,\text{A}^{-1}$, an equilibrium bond angle $\theta_0 = 120°$, a bond energy $E_0 = 4.99\,\text{eV}$, a bond depth $\beta = 2.1867\,\text{A}^{-1}$, torsion force constant $k_\phi = 0.262\,\text{eV}$, and a bending force constant $k_\theta = 5.86\,\text{eV}$ are used (values taken from [158]). For more details on MC simulations, see Section 3.1.2. Additionally, the results of the vdW model for doubly-curved structures are compared to those of two continuum vdW models, M1 and M2, for planar structures. The pressure-distance behavior of M1 is described by Equation (5.5), and that of M2 is obtained by linearizing Equation (5.5) at the equilibrium distance of graphite, α_{eq}, leading to

$$p = C\Delta\alpha \ . \tag{5.55}$$

The parameter $\Delta\alpha$ is the change in the interlayer distance and $C = C_{33}/\alpha_{\text{eq}}$. To be consistent with the MC simulations the following values are used for the LJ-parameters: $\varepsilon = 0.00319\,\text{eV}$ and $\sigma = 0.3345\,\text{nm}$ [176]. With these values $\alpha_{\text{eq}} = 0.3345\,\text{nm}$ can be obtained for $p(\alpha) = 0$ where $p(\alpha)$ is given by Equation (5.5). The models M1 and M2 describe the pressure-distance behavior of graphene,

Table 5.2: Calculated equilibrium configurations of nested fullerenes obtained with continuum mechanics (present vdW, M1, M2) and Monte Carlo simulations. Data from [145].

		R_1 [nm]	R_2 [nm]	α [nm]
	Monte Carlo	0.34407	0.62013	0.27606
C60 in C180	present vdW	0.34277	0.61888	0.27611
	M1	0.34728	0.62227	0.27499
	M2	0.35031	0.61315	0.26283
	Monte Carlo	0.35146	0.70320	0.35174
C60 in C240	present vdW	0.35152	0.70316	0.35165
	M1	0.35157	0.70293	0.35137
	M2	0.35164	0.70265	0.35101

and thus, do not account for the difference in the number of atoms in neighboring layers.

The results of the MC simulations and all continuum models are summarized in Table 5.2. The obtained equilibrium configurations of the continuum vdW model for doubly-curved structures are in good agreement with the results of the MC simulations. The difference for the interlayer distance is only around 2%, and also the equilibrium radii are obtained accurately. M1 and M2 also give good approximations of the equilibrium configurations, where the results of M2 are the least accurate ones. However, the differences to the MC simulations are for M1 and M2 larger than those of the model for doubly-curved structures. It has to be noted that the interlayer distance is underestimated by M1 and M2 for both configurations of nested fullerenes. For all models the results obtained for C60 in C240 are closer to the MC simulations than those calculated for C60 in C180. For C60 in C240 the initial interlayer distance $\alpha^{(0)}$ is closer to the equilibrium distance of graphite α_{eq}, whereas $\alpha^{(0)}$ is significantly different from α_{eq} for the case of C60 in C180. This leads to the conclusion that the performance of the vdW models depends – besides the initial radii – on the initial interlayer distance $\alpha^{(0)}$. This is logical since the effect of the vdW interactions itself strongly depends on the distance between the layers and decreases fast with increasing interlayer distance.

It has to be noted that C60 is almost perfectly spherical, but C180 and C240 are more polyhedral in their shape rather than spherical. Nevertheless, the continuum model of the nested fullerenes gives reliable results for the averaged equilibrium configuration. Locally different interlayer distances and layer radii induced, e.g., by a locally different atom density due to pentagonal rings cannot be captured with the continuum model.
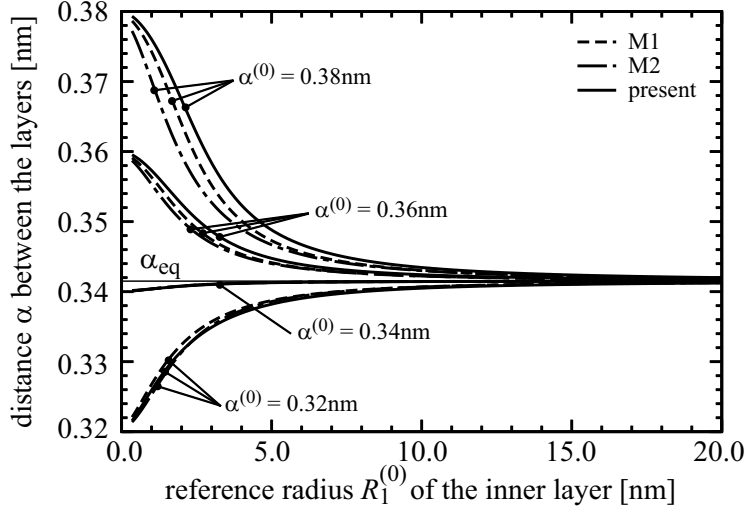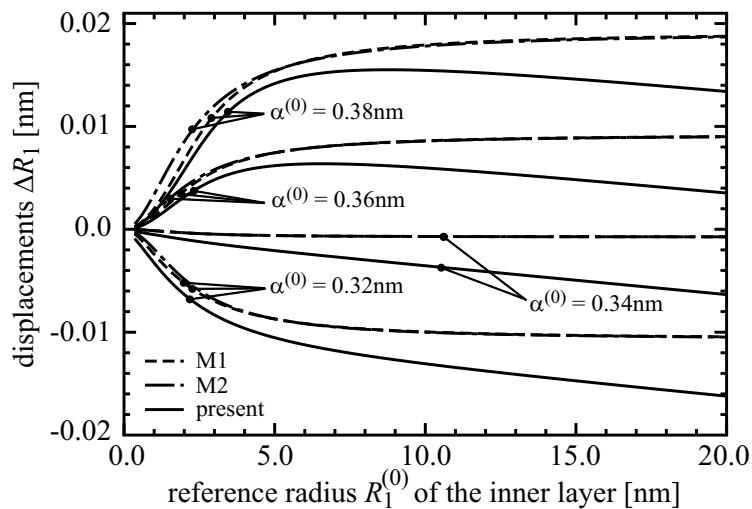
Figure 5.6: Equilibrium distance of two onion layers depending on the reference radius $R_1^{(0)}$ of the inner layer and the reference interlayer distance $\alpha^{(0)}$ [145].

5.5.5 Results and Comparison with Simplified Models

To show the consequences of taking the curvature effect into account in the formulation of the vdW model a parameter study is performed where the results of different vdW models are compared. The vdW model for doubly-curved structures performs best for nested fullerenes, see Section 5.5.4. Thus, this model is taken as reference. For the parameter study the initial radius of the inner layer $R_1^{(0)}$ is varied from $0.35\,\text{nm}$ to $20\,\text{nm}$ and different reference distances $\alpha^{(0)} = 0.32, 0.34, 0.36, 0.38\,\text{nm}$ are used. For the membrane stiffness k_S a value of $11263.2\,\text{J/m}^2$ is chosen, being the same as in Section 5.5.4. For calculating the atom area density ρ_∞ a carbon-carbon bond length of $a^{(0)} = 0.142\,\text{nm}$ is used. The LJ-parameters used are different from those of Section 5.5.4 and read $\epsilon = 0.00239\,\text{eV}$ and $\sigma = 0.3415\,\text{nm}$, leading to $\alpha_\text{eq} = 0.3415\,\text{nm}$.

The obtained results for the equilibrium interlayer distance are depicted in Figure 5.6. It is clearly visible that the performance of the models M1 and M2 strongly depends on the initial interlayer distance $\alpha^{(0)}$. If $\alpha^{(0)}$ is close to the equilibrium interlayer distance α_eq of graphene all models give the same results. M1 and M2 show a slightly different behavior compared to the model for doubly-curved structures if the vdW interaction is initially under compression ($\alpha^{(0)} = 0.32\,\text{nm}$), where the difference is more strongly pronounced for small fullerenes with $R_1^{(0)} < 5.0\,\text{nm}$. For interlayer distances $\alpha^{(0)} > \alpha_\text{eq}$ the interlayer distance is underestimated by M1 and M2, where the difference to the reference model is the stronger the larger $\alpha^{(0)}$ and the smaller the fullerene is. With increasing size of the fullerenes the interlayer distance approaches α_eq independently of the model used and of the initial interlayer distance $\alpha^{(0)}$.
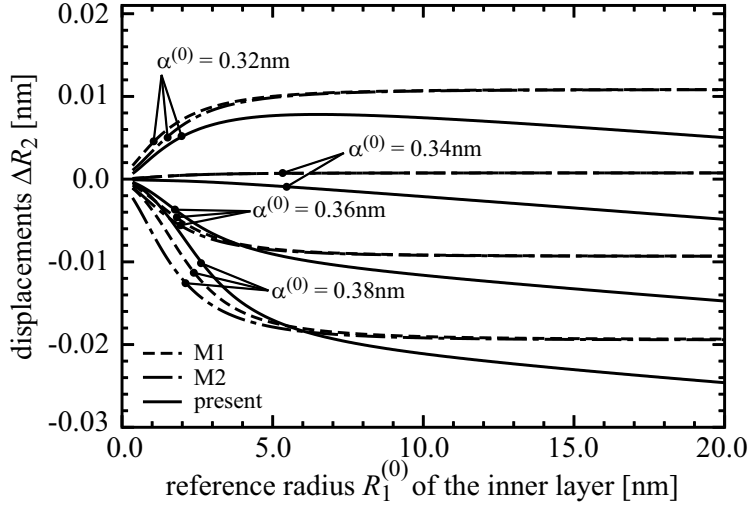
Figure 5.7: Radial displacements ΔR_1 of the inner layer depending on the reference radius $R_1^{(0)}$ of the inner layer and the reference interlayer distance $\alpha^{(0)}$ [145].

Although all models show comparable behavior for the resulting interlayer distances, the differences between them become obvious if the deformations of the individual layers are considered, see Figures 5.7 and 5.8. M1 and M2 still show the same overall behavior. Differences between these two models can only be observed for $\alpha^{(0)} = 0.38$ nm and there only for fullerenes with $R_1^{(0)} < 5.0$ nm. If the vdW interface is initially under compression ($\alpha^{(0)} = 0.32$ nm) the inner layer is more strongly compressed for the vdW model for doubly-curved structures (present model) whereas the displacements of the outer layer are smaller compared to M1 and M2. This phenomenon is a result of the different number of atoms in the layers. The inner layer is compressed by more atoms of the outer layer than the outer layer is repelled by the atoms of the inner layer. A surprising result is that for $\alpha^{(0)} = 0.34$ nm $< \alpha_{\mathrm{eq}}$ both layers decrease in their size, although one would expect the outer layer to become a little larger, as it is observed for M1 and M2. However, the present model is in good agreement with MC simulations giving the model credibility. For $\alpha^{(0)} > \alpha_{\mathrm{eq}}$ and $R_1^{(0)} < 5.0$ nm the displacements of the inner and outer layers are smaller for the current model resulting in larger interlayer distances α, as already discussed above. For $R_1^{(0)} > 5.0$ nm the displacements of the outer layer grow larger whereas the inner layer deforms less and less. This behavior is quite different to those observed for M1 and M2.

5.5.6 Summary

A continuum mechanical vdW model in the form of pressure-radius relations is derived for doubly-curved carbon nanostructures. The different number of atoms in

Figure 5.8: Radial displacements ΔR_2 of the outer layer depending on the reference radius $R_1^{(0)}$ of the inner layer and the reference interlayer distance $\alpha^{(0)}$ [145].

neighboring layers is accounted for, leading to different vdW-induced pressures on opposite faces of neighboring layers. As the atom area density is used to describe the number of atoms in the layers the model has a homogenizing character, and effects due to a locally different atom density cannot be captured. Nevertheless, the model approximates the "mean" equilibrium configurations of nested fullerenes better than existing simplified models, as shown by comparisons with MC simulations. A further comparison shows that the obtained interlayer distances are in good agreement with the interlayer distances of the simplified models. However, the deformations of the individual layers are significantly different from those of the simplified models, especially for large fullerenes. Concluding, it can be said that the derived vdW model should be used if the radial deformations of the layers and the corresponding subsequent membrane forces are of importance, e.g. if the stability of multi-layer doubly-curved structures is investigated.

5.6 ABAQUS Models

The presented continuum vdW models in conjunction with equations describing the mechanical behavior of the layers give access to the analytical solution of the mechanical behavior of carbon nanostructures. However, an analytical solution can only be obtained for simple structures and some elementary load cases. For complex loading conditions and geometries numerical methods have to be employed, where the finite element method is the most common one in continuum mechanics. Different modeling approaches are possible for applying the vdW models in an finite element analysis. In the following the implementation of two approaches

into the finite element program ABAQUS[1] is discussed.

5.6.1 Van der Waals interactions via Spring Elements

The vdW interactions between neighboring layers are equivalent to a nonlinear elastic bedding. In a finite element model such a bedding can be represented by nonlinear spring elements. In the following only directly opposing finite element nodes on adjacent layers are linked by a spring element, i.e. there is no interaction between neighboring points of the bedding (a nonlinear Winkler bedding is used). As a further simplification it is assumed that the distance between adjacent layers ,α, is close to the equilibrium interlayer distance, α_{eq}, and that changes $\Delta\alpha$ in the interlayer distance are small, too. Thus, the behavior of the vdW bedding can be linearized around α_{eq}, and linear spring elements can be used to model the vdW bedding.

ABAQUS provides two different types of springs connecting two nodes, namely SPRINGA, whose line of action is the line joining the two nodes, and SPRING2, which is acting in a fixed direction. Both spring types can be either linear or nonlinear, depending on their property definitions. In the case of linear spring elements the only property parameter required is the spring stiffness in terms of force per relative displacement. The stiffness of the vdW bedding, $\hat{k}$, in terms of a pressure distance relation can be derived by linearizing Equations (5.5) or (5.11) around α_{eq}. In the following only Equation (5.5) is considered, leading to

$$\hat{k} = -\frac{\mathrm{d}p}{\mathrm{d}\alpha}\big|_{\alpha=\alpha_{\text{eq}}} = \frac{C_{33}}{\alpha_{\text{eq}}} \ . \tag{5.56}$$

The minus sign in Equation (5.56) considers that forces in a spring are positive for attraction and negative for repulsion. With $\hat{k}$ the corresponding pressure-distance relation reads

$$p_{\text{lin}} = \hat{k} \cdot \Delta\alpha \ . \tag{5.57}$$

To obtain the stiffness of the spring elements, k_{kl}, the stiffness of the bedding $\hat{k}$ is multiplied by the area A_{kl} associated with the finite element nodes l and k linked by the spring, see Figure 5.9. The area A_{kl} is chosen in a way that the resulting spring forces acting on nodes k and l lead – under consideration of the shape function of this element – to the same virtual work as the distributed vdW pressure acting on A_{kl}. For planar structures the areas A_k and A_l obtained at node k and l , respectively, are equal, whereas for curved nanostructures A_k and A_l are different, especially if the layer radius is small. In the latter case $A_{kl} = \frac{A_k+A_l}{2}$ is assumed and k_{kl} can be calculated as

$$k_{kl} = \hat{k} \cdot A_{kl} \ . \tag{5.58}$$

---

[1]http://www.simulia.com/products/abaqus_fea.html
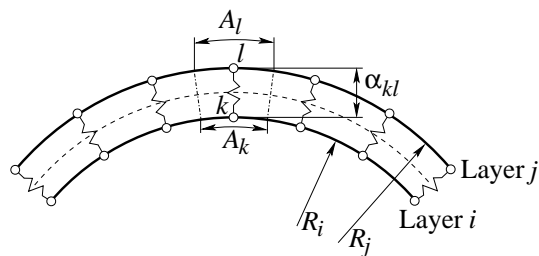
Figure 5.9: Areas associated to nodes k and l in curved structures.

Finally the force in the spring, and thus, the vdW force acting on a single finite element node of the layers can be obtained as

$$F_{kl} = k_{kl} \cdot (\alpha_{kl} - \alpha_{\text{eq}}) = \hat{k} \cdot A_{kl} \cdot (\alpha_{kl} - \alpha_{\text{eq}}), \qquad (5.59)$$

where α_{kl} is the current distance between nodes k and l.

Thus, using the spring vdW model leads to equal forces on opposite faces of neighboring layers

$$p_i A_i = p_j A_j = p(\alpha)\frac{A_i + A_j}{2} \; , \qquad (5.60)$$

for planar structures ($A_i = A_j$) as well as for curved structures ($A_i \neq A_j$). The quantities p_i and p_j are the vdW pressures acting on the layers and A_i and A_j are the corresponding surface areas. From Equation (5.60) it can be seen that the different curvature of neighboring surfaces is considered, although not in a correct way, see Sections 5.4 and 5.5.

5.6.2   Van der Waals interactions via User Interface

Using spring elements for modeling the vdW bedding is an pre-processing-intensive task, as shown in the previous section. Another possible way to model the vdW bedding in ABAQUS is to define a user interface UINTER, see e.g., [114, 170].

The pressure-distance relations describing the interactions between the master and slave surfaces have to be implemented by the user. The current relative position of a point on the slave surface with respect to the nearest point of the master surface in normal and transversal directions is handed over to the interface by ABAQUS. Thus, the stress in normal direction can be directly defined by using either Equation (5.5) or Equation (5.11), where the interlayer distance α is equal to the relative position in normal direction. The stresses have to be positive for compression and negative for tension. As the shear stiffness of the vdW interface is small compared to the normal stiffness, it will be neglected in the vdW model, see also [114]. Therefore, the tangential stresses are set to zero, i.e., a frictionless interface is defined. The normal and tangential directions are always defined with respect to the master surface. To ensure proper convergence

characteristics, also the interface stiffness matrix $\underset{\approx}{\mathbf{K}}^{(\mathrm{I})}$ has to be implemented by the user. The matrix element $K_{ij}^{(\mathrm{I})}$ defines the change in the i-th stress component due to an infinitesimally small perturbation of the j-th component of the relative displacement array. Thus, the component $K_{11}^{(\mathrm{I})}$ is equal to the current stiffness of the vdW bedding in normal direction in terms of a pressure-distance relation

$$K_{11}^{(\mathrm{I})} = \frac{\partial p(\alpha_{\mathrm{eq}} + \Delta\alpha)}{\partial\Delta\alpha} \tag{5.61}$$

All other components of the interface stiffness matrix are set to zero, as the vdW interface is assumed to have zero shear stiffness.

The interface model also considers a possible curvature of the nanostructures, such that the total forces due to the vdW pressure on the interacting surfaces are equal. The resulting normal force due to contact is related to the slave surface $p(\alpha)A_{\mathrm{slave}} = p_{\mathrm{master}}A_{\mathrm{master}}$, thus the magnitude of the vdW forces acting on the surfaces depends on the choice of the master and slave surfaces.

5.7 Conclusion

Continuum van der Waals models for multi-layer carbon nanostructures with different degrees of curvature have been presented. It has been shown that the difference between the number of atoms forming adjacent layers in curved nanostructures has to be considered to get a correct representation of the vdW interactions. Using a correct vdW model is especially crucial if the displacements and the subsequent stresses in the layers are of importance, e.g., if the mechanical stability of a structure is considered. Although the vdW models which account for a curvature of the structure give more accurate results, they cannot be implemented in standard finite element programs in a straight forward way. Thus, they are only applicable for simple multi-layer structures subjected to elementary load cases. Access to finite element solutions of multi-layer nanostructures is possible by using simplified vdW models, which allow a straight forward implementation but are less accurate. This trade-off between accuracy and applicability has to be considered in choosing an appropriate vdW model. The simplified finite element vdW models are used in the following chapters where the stability of carbon crystallites and carbon onions is investigated.

Chapter 6

Elastic Properties of Carbon Crystallites

6.1 Introduction

Carbon reinforced plastics (CFRP) possess high stiffness and strength at low density, making them perfect materials for lightweight design applications. Thus, their usage in aircraft, space, automotive, and sports industries has increased substantially within the past decades. This increase in use requires a better understanding of the material behavior of CFRP in order to avoid catastrophic failures during product life.

CFRP are composite materials consisting of carbon fibers embedded in a matrix made of, e.g., epoxy resin. The properties of CFRP are influenced by the properties of the fibers and the matrix, the amount of fibers in the matrix, the bonding between the constituents, the fiber orientation etc. Although many different parameters influence the properties of CFRP it is necessary to have detailed knowledge about the properties of their constituents. Hence, the mechanical properties of carbon fibers are of great interest, and subject of intense research activities, see, e.g., [58, 91, 109, 129].

The tensile behavior of the fibers is well described, see ,e.g., [109, 129], whereas identifying the compressive behavior is more complicated due to experimental difficulties. Single carbon fibers are only a few micrometers in diameter and, thus show a tendency towards buckling when subjected to compressive loading. To overcome these problems several methods have been developed such as the elastic loop test [133], the single fiber composite test [59], the bending beam test [35], the tensile recoil method [4], and the direct compression method [112]. A good overview of these methods is provided, e.g., in [112].

Besides experiments, computational methods can be used in order to gain better insight into the mechanisms determining the properties of carbon fibers. In
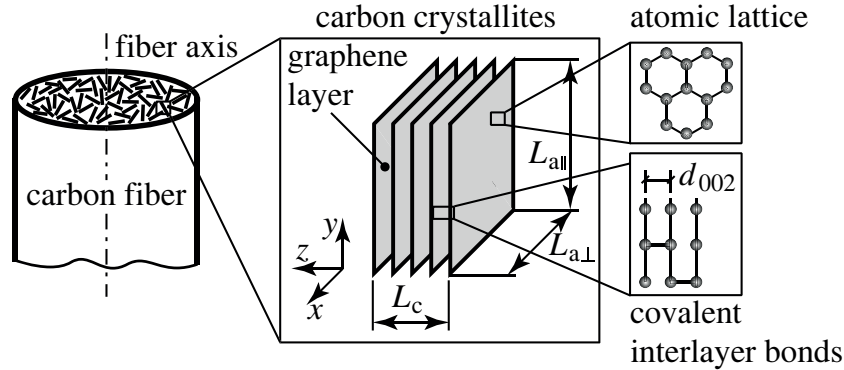
Figure 6.1: Nanostructure of PAN-based carbon fibers [147].

the present work the compressive behavior of polyacrylonitrile (PAN) based carbon fibers is investigated on a nano-scale level using the finite element method. The cross section of PAN based fibers usually shows a skin-core structure [115]. The outer surface of the fibers is formed by a skin-like layer, whereas randomly distributed carbon crystallites form the inner region of the cross section, see Figure 6.1. Carbon crystallites are stacks of imperfect graphene layers and have a size of a few nanometers. The layers are oriented almost parallel to the fiber axis and interact by weak vdW forces. The fiber properties in axial direction are closely related to the properties of the graphene layers, whereas the properties perpendicular to the axis are dominated by weak vdW interactions between the layers. Thus, the material behavior of the fiber is anisotropic and related to the properties of the carbon crystallites.

The influence of the orientation and size of the crystallites is investigated, e.g., in [38]. To obtain a high compressive strength of the fibers the carbon crystallites should be smaller than approximately 5 nm in all directions and should be oriented parallel to the fiber axis [38]. Further, a homogeneous distribution of the disordered regions over the fiber cross section is favorable [38]. In [113, 110] it is assumed that crystallite buckling occurs in fibers subjected to compressive loading. Failure of PAN based fibers is also related to crystallite buckling [38], as is the non-Hookean behavior of fibers observed in loop tests [58]. Experimental proof of crystallite buckling is found in [91], where it is directly observed using microbeam X-ray diffraction. Furthermore, in [91] a shift in the neutral axis of bent fibers is observed which is also related to the onset of crystallite buckling.

In the following a single carbon crystallite is investigated to better understand the influence of crystallite buckling on the mechanical properties of PAN based fibers. A finite element model of such a crystallite is developed to study its compressive response and the influence of covalent interlayer bonds on its buckling resistance. Parts of the results presented in this chapter have previously been published in [147].
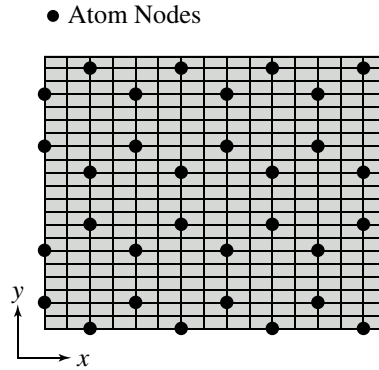
Figure 6.2: Finite element discretization of a single graphene layer accounting for the position of carbon atoms (only a small cut-out of the layer is shown).

6.2 Methodology

6.2.1 Crystallite Model

Carbon crystallites are planar structures consisting of a number of graphene layers of finite extension, as shown in Figure 6.1. The layers are modeled as thin elastic plates with an elastic modulus $E = 5.5\,\text{TPa}$, a Poisson's ratio $\nu = 0.19$, and a layer thickness $h = 0.066\,\text{nm}$, as discussed in Section 4.2 (values taken from [169]). The hexagonal arrangement of the carbon atoms is implicitly taken into account, as it is assured that finite element nodes are located at the atom positions, see Figure 6.2. These nodes are required later on for introducing covalent interlayer bonds. A carbon-carbon bond length of $0.149\,\text{nm}$ is used and it is assumed that the graphene layers are oriented parallel to the fiber axis. According to [38] the in-plane dimensions of the layers should be smaller than $5\,\text{nm}$. Hence, $L_{\text{a}\parallel} = 4.32\,\text{nm}$ and $L_{\text{a}\perp} = 3.87\,\text{nm}$ are used for the length parallel and perpendicular to the fiber axis (in y and x directions, respectively), being in good agreement with experimentally obtained values, see e.g. [38, 113]. To allow a straight forward random insertion of covalent interlayer bonds, it is assumed that atoms on neighboring layers are perfectly aligned, representing an AA stacking of the layers. According to [27] AA-stacking is energetically less favorable than AB stacking of graphite shown in Figure 2.2. However, the energy difference between these two configurations is small [34], so that the assumption of AA stacking seems reasonable.

The atoms forming a layer interact via vdW forces with the atoms forming the adjacent layers. To describe the vdW interactions the interface model described in Section 5.6.2 is used, where Equation (5.5) is employed to describe the vdW pressure-distance relation. For the compressive constant C_{33} a value of $36.5\,\text{GPa}$ is used [72, 183]. In Equation (5.5) the Lennard-Jones parameter σ determines the equilibrium vdW distance $\alpha_{\text{eq}} = \sigma$ and is chosen to be $\sigma = 0.344\,\text{nm}$. This value is in good agreement with the equilibrium vdW distances observed for carbon

crystallites ranging from $\alpha_{eq} = 0.344\,\text{nm}$ to $0.356\,\text{nm}$ in [92] or $\alpha_{eq} = 0.339\,\text{nm}$ to $0.347\,\text{nm}$ in [113], depending on the fiber type.

The width L_c of crystallites in standard PAN based fibers is between 1.7 and $5.9\,\text{nm}$ [38]. The values obtained for high-modulus and high-strength PAN based fibers range from 2.60 to $2.70\,\text{nm}$, and 3.47 to $8.38\,\text{nm}$, respectively [113]. In the present work it is assumed that the crystallite is formed by eight layers, resulting in a width $L_c = 2.512\,\text{nm}$, which is in good agreement with these values.

In [128] the influence of the fiber's nanostructure on the elastic properties is investigated using the theory of elasticity for anisotropic solids. The tensile properties of the fibers are determined, with an artificially high interlayer shear modulus of the carbon crystallites being used to obtain a good representation of the elastic modulus of the fibers [128]. A relatively high interlayer shear modulus of carbon crystallites is also observed in [92] for PAN based fibers. One possible reason for this increased interlayer shear modulus is the formation of covalent bonds between the layers of the crystallite. The graphene layers forming the crystallites can contain defects such as vacancies and interstitial atoms. These defects can be sources for the formation of covalent interlayer bonds [143]. Furthermore, dangling bonds at the edges of the graphene layers [156] can lead to the formation of interlayer bonds. In [53] it is shown that nanoindentation of multi-walled nanotubes and multi-layer graphene also gives rise to the formation of covalent interlayer bonds. The formation of these bonds locally increases the hardness of the nanostructures but is reversible as long the quantity of bonds is below a critical value [53]. Interlayer bonds also influence the mechanical properties of multi-walled carbon nanotubes [21, 65, 116], and carbon nanotube bundles [74]. Cross links constrain sliding between nanotube walls [21] and adjacent nanotubes [74], the load transfer between the tubes being best if the bonds are uniformly distributed [21]. However, for covalent bonds formed by Frenkel pair defects [143] a decrease in the axial buckling load of double-walled nanotubes is observed, as the Frenkel pair defect weakens the layers and stresses are concentrated around these defects [116].

The examples given above show that interlayer bonds should be considered in the computational analysis of carbon crystallites. For the sake of simplicity it is assumed that interlayer bonds at the edges and in the interior of the crystallite are similar and that the formation of interlayer bonds does not lead to any vacancies in the layers. Furthermore, it is assumed that the interlayer bonds reduce the interlayer distance locally to $d_c = 0.258\,\text{nm}$, corresponding to the value obtained for a fourfold coordinated interstitial atom [143]. For possible locations of the interlayer bonds two different distributions are considered. First, the interlayer bonds are distributed over the whole crystallite (including the edges). Second, the interlayer bonds are distributed along the edges only. In both distributions the defects are randomly introduced where it is assured that each finite element node representing a carbon atom (in the following referred to as atom node) is participating in at most one interlayer bond.

Each interlayer bond is modeled by a truss element (i.e., no bending or torsional stiffnesses), with its axial stiffness being much higher than the membrane stiffness of the layers. Due to the assumption of AA stacking one truss element connects two atom nodes on two adjacent layers, which are perfectly aligned. This simple truss model results in zero shear modulus between the layers, which is in contrast to findings made in [21, 92, 128]. However, it is assumed that the layers are perfectly parallel to the fiber axis, thus shear should be negligible before buckling occurs. Furthermore the interlayer shear stiffness is only 1.2% of the effective axial modulus of the crystallites [92] and, hence, the absence of the shear stiffness should have no major influence on the post-buckling behavior of the crystallite.

The quantity of interlayer bonds is varied from 1 to 5% to investigate their influence on the buckling load and the post-buckling behavior. It should be noted that if the interlayer bonds are located only at the edges, a value of 5% is close to the maximum number of interlayer bonds possible for the crystallite dimensions used in this study.

6.2.2 Analysis Steps

Step 1: Introducing the Interlayer Bonds

To get a reasonable representation of the self-equilibrating state in the layers due to the formation of the covalent interlayer bonds, the bonds are first introduced with an initial length of $d_c^{(0)} = 0.34\,\text{nm}$. Then these bonds are subjected to a virtual temperature change ΔT (cool down) to reduce their length from $d_c^{(0)}$ to $d_c = 0.258\,\text{nm}$. Considering geometrically nonlinear behavior the required temperature change ΔT can be estimated as

$$\Delta T = \ln\left(\frac{d_c}{l_c}\right)\frac{1}{\alpha_c}\ .\tag{6.1}$$

The quantity α_c is a fictitious coefficient of thermal expansion which, e.g. is assumed to be $1\,\text{K}^{-1}$. The boundary conditions used while introducing the interlayer bonds are depicted in Figure 6.3 (a). The individual layers are constrained as little as possible, but sufficiently for avoiding rigid body motions. The z-displacements are only constrained in three corners of layer 1, all other layers are bonded by vdW interfaces to the layers underneath.

Step 2: Compressive Loading

The axial compression is applied via prescribed displacements, u_y, in $-y$-direction on the upper edge of the crystallite. It is assumed that the upper edges of all layers are subjected to the same axial displacement. Carbon fibers usually have diameters in the range of 1 to $10\,\mu\text{m}$, being much larger than the crystallite dimensions perpendicular to the fiber axis ($\approx 4 \times 2.5\,\text{nm}$). Thus, the microstrain [91] in fiber
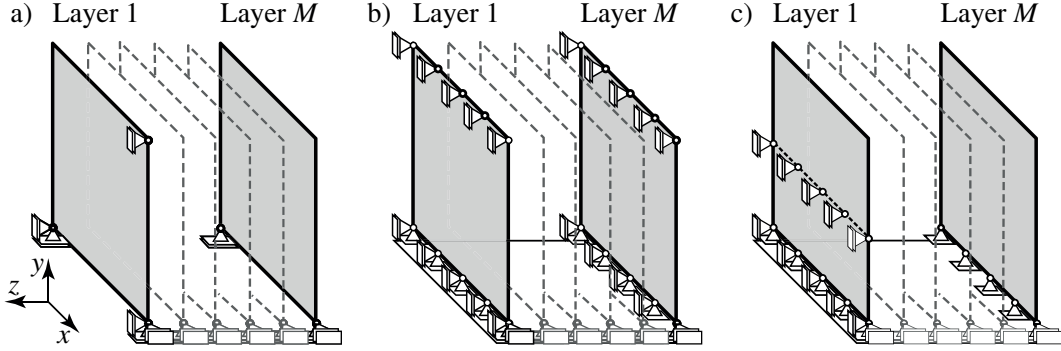
Figure 6.3: Boundary conditions applied to the crystallite during step 1 (a) and boundary conditions BC1 (b) and BC2 (c) used in step ((a) and (b) from [147]).

bending is assumed to be constant over the crystallite's dimensions. Two different types of boundary conditions are used in the second step, depicted in Figures 6.3 (b) and (c), respectively. For the first type (BC1) the z-displacements of Layer 1 are constrained on its upper and lower edges edges, whereas for the second type (BC2) the z-displacements are constrained at the lower edge and at the mid-line at $L_{a\parallel}/2$, see Figure 6.3.

6.3 Results

6.3.1 Step 1: Introducing the Interlayer Bonds

Typical deformations introduced by the formation of the covalent interlayer bonds are depicted in Figure 6.4. The vdW interactions between the layers prevent a uniform reduction of the interlayer distance by the covalent bonds, and thus local dimples form at the bond locations. If the bonds are randomly distributed over the whole crystallite the layers remain almost parallel to the fiber axis (y-axis), see Figure 6.4 (a). A pre-bending deformation in the form of an overall bulge can be observed if the bonds are located only at the edges as shown in Figure 6.4 (b). This bulge leads to a misalignment of the crystallite with respect to the fiber axis.

To quantify this misalignment the average azimuthal angles, χ_S and χ_N, are evaluated on the south (S) and north (N) sides of the crystallite, respectively. For each layer of the crystallite the deformations of the nodes along a skeleton line are measured, as depicted in Figure 6.5. The first ten nodes in the deformed configuration at the S and N side of the crystallite are then fitted with first order polynomials. From the slopes $k_{li} = \Delta z/\Delta y$ of the polynomials the azimuthal angles are evaluated as

$$\chi_{ki} = \arctan(k_{li}) \tag{6.2}$$

where the indices l and i denote the side (N or S) and the layer number, respec-
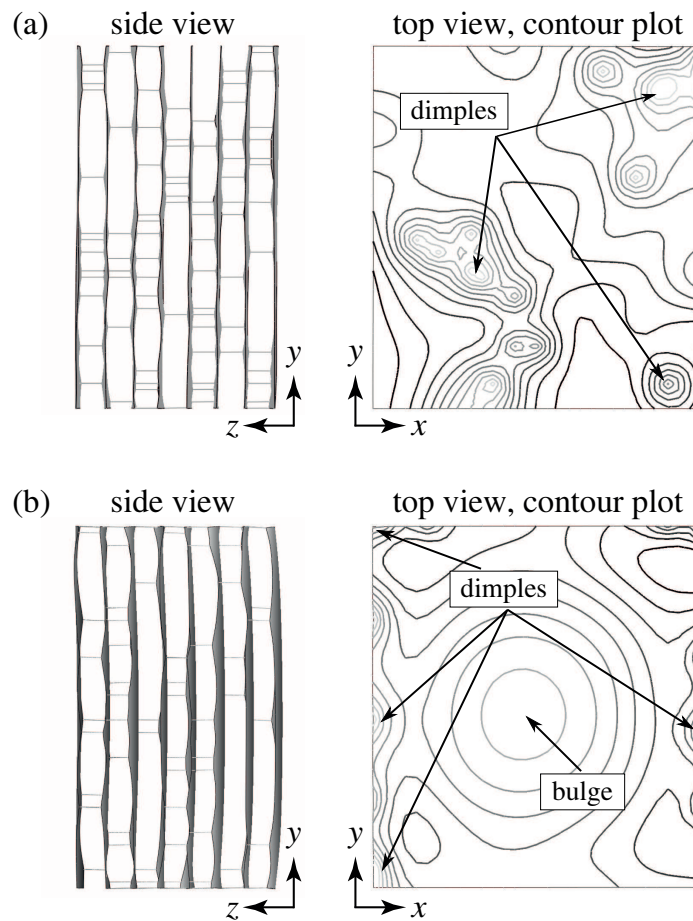
Figure 6.4: Deformation states after the initial step for crystallites with their interlayer bonds being randomly distributed over the whole crystallite (a) or being located only at the edges (b). The side view of the deformation state and the contour lines of the z-displacements of the uppermost layer are depicted on the left and right side, respectively [147].
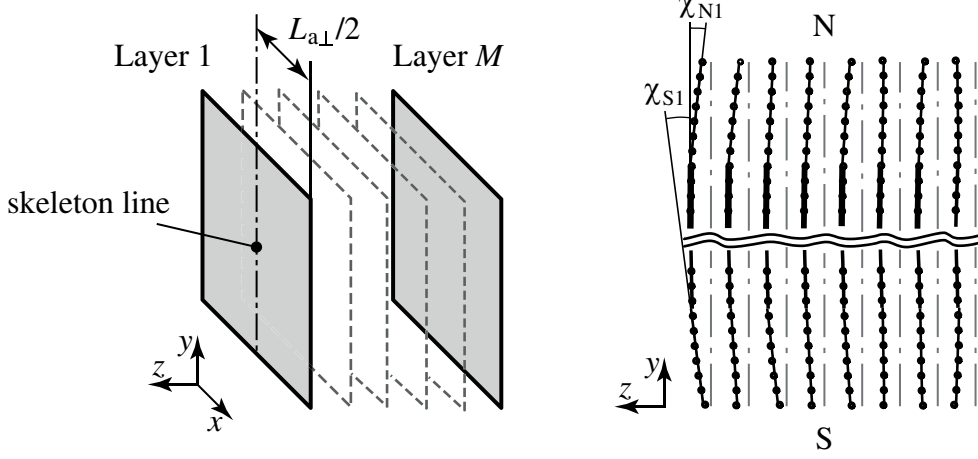
Figure 6.5: Measurement of the azimuthal angles, χ_S and χ_N, in the deformed state of carbon crystallites.

tively. With the azimuthal angles of the layers χ_{li} the average azimuthal angles of the crystallite read

$$\chi_S = \frac{1}{M} \sum_{i=1}^{M} \chi_{Si} \tag{6.3}$$

for the south side, and

$$\chi_N = \frac{1}{M} \sum_{i=1}^{M} \chi_{Ni} \tag{6.4}$$

for the north side, with $M = 8$ being the number of layers forming the crystallite.

Figure 6.6 shows the dependencies of the azimuthal angle on the proportion of covalent interlayer bonds after the formation of the bonds. If the interlayer bonds are randomly distributed over the whole crystallite the azimuthal angles χ_S and χ_N are close to 1° and show no clear dependence on the proportion of interlayer bonds. The azimuthal angles obtained for crystallites with the bonds only located at the edges are significantly higher and increase with the amount of interlayer bonds, although some fluctuations of the curves can be observed.

The misalignment obtained with the computational models is smaller than the 11° measured in [91]. However, in [91] a total misalignment is measured which conceivably is a superposition of a general misalignment and the pre-bending deformation due to the bond formation. As it is assumed that the layers of the crystallites are initially parallel to the fiber axis, the general misalignment is not captured with the current model. Finite graphene sheets also posses a certain waviness [18, 103] which is not taken into account, either.
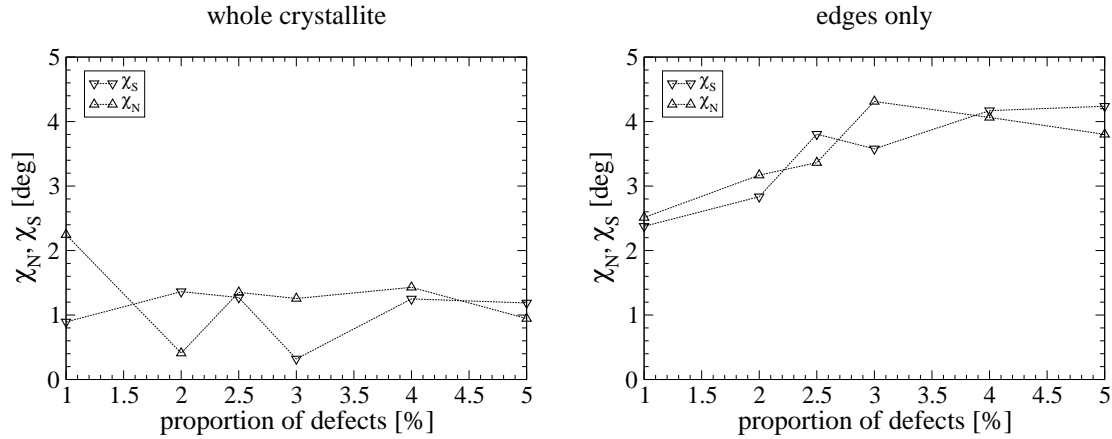
Figure 6.6: Azimuthal angles χ_S and χ_N depending on the proportion of interlayer bonds after the formation of the covalent interlayer bonds.

6.3.2 Step 2: Compressive Loading

The different deformation states obtained after the first step for the two distributions of defects also lead to differences in the compressive behavior of the crystallites. Figures 6.7 and 6.8 show the different load-displacement responses, depending on the location of the interlayer bonds and the boundary conditions used. In the pre-buckling state the obtained reaction forces F_y depend linearly on the applied displacements u_y if the interlayer bonds are randomly distributed over the whole crystallite, see Figures 6.7 (left) for BC1 and 6.8 (left) for BC2. The occurrence of crystallite buckling is indicated by a sudden and significant reduction of the tangential stiffness $K_T = \frac{\mathrm{d}F_y}{\mathrm{d}u_y}$. The corresponding buckling load increases significantly with the proportion of covalent interlayer bonds, whereas the tangential stiffness K_T in the pre- and post-buckling regime seems to be independent of the proportion of interlayer bonds. The increase in the critical load is slightly more pronounced for BC1.

If the interlayer bonds are only distributed along the edges the response of the crystallite is nonlinear even for small displacements u_y as shown in Figures 6.7 (right) and 6.8 (right) for BC1 and BC2, respectively. This nonlinear response is a result of the pre-bending deformations introduced by the formation of the bonds. Although the misalignment of the crystallites is stronger for larger quantities of bonds, initially all crystallites behave the same way. However, the difference between the responses evolves with increasing values of u_y, with a larger quantity of interlayer bonds tending to result in higher reaction forces F_y.

For crystallites containing 1% or 2.5% of interlayer bonds different random distributions have been analyzed to investigate their influence on the load-displacement response. Due to high computational costs of the analyses the study is limited to BC1 and a small number of different random distributions. For each of the consid-
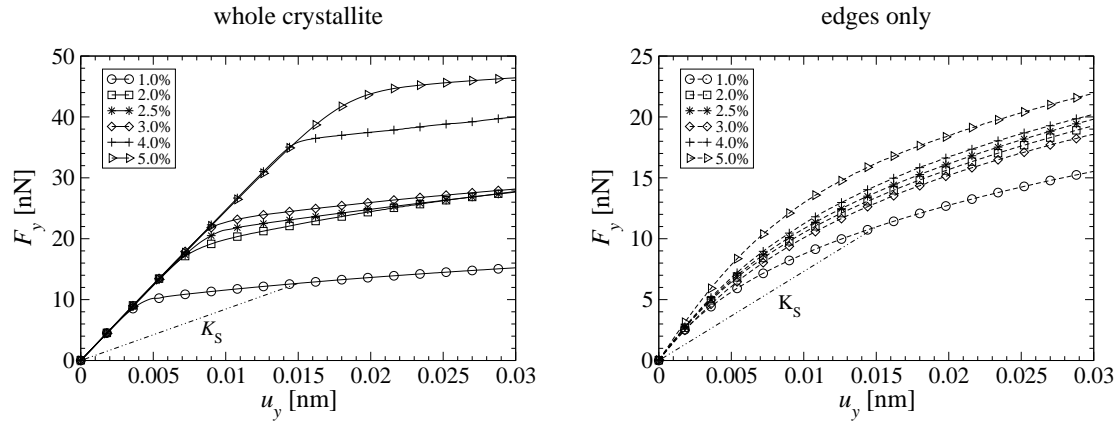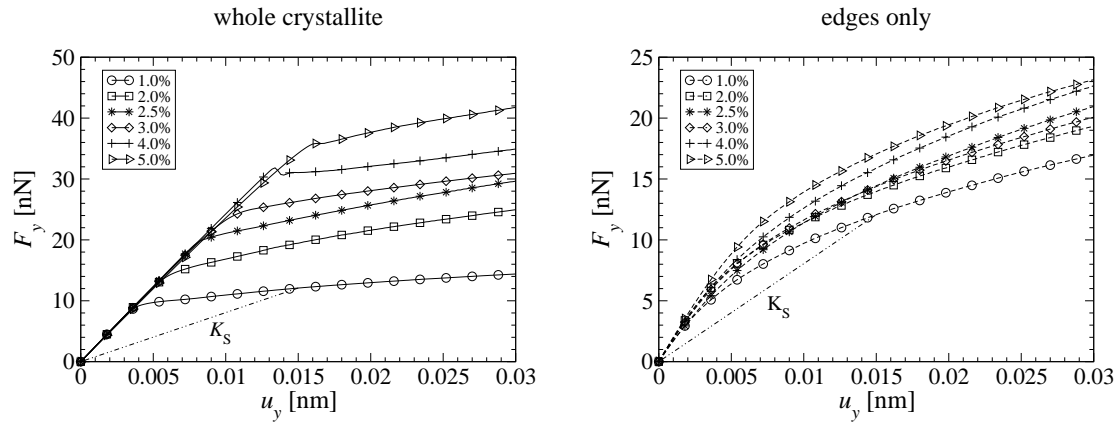
Figure 6.7: Load displacement diagram for different proportions of covalent interlayer bonds and for boundary conditions BC1. The figure on the left was already published in [147].
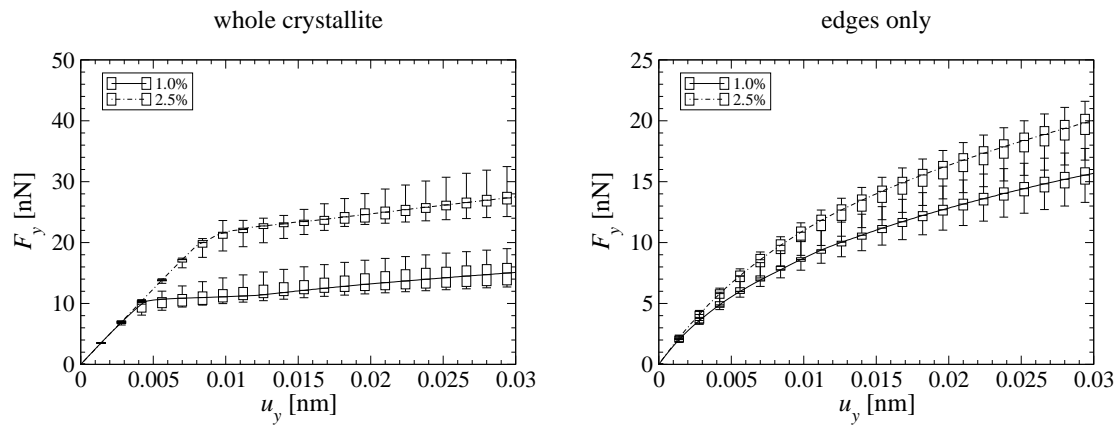
ered proportions of interlayer bonds 10 configurations are studied for bonds that are randomly distributed over the whole crystallite and another 10 configurations for bonds located solely at the edges. The results are summarized in box plots shown in Figure 6.9, where the curves represent the median of the values. The bottom and top of each box mark the 25% and 75% percentile of the data, i.e., each box contains 50% of the data. The ends of the whiskers mark the minimum and maximum values. When the interlayer bonds are distributed over the whole crystallite, the influence of the distribution on K_t is negligible in the pre-buckling regime, see 6.9 (left). However, the distribution of the bonds has a strong influence on the critical load and the post-buckling behavior as the dimples introduced by the formation of the bonds act as imperfections on the otherwise planar graphene sheets. For the case of 2.5% of interlayer bonds the influence of the distributions is smaller as indicated by the smaller boxes. This is due to the fact that the different possible configurations possess a higher similarity for higher quantities of interlayer bonds. Although, the distribution of the bonds has an influence on the critical load it is still possible to distinguish between the two different proportions considered, as not even the whiskers overlap in the post-buckling regime.

For the bonds being distributed only at the edges the whiskers in the plot overlap as depicted in Figure 6.9 (right), although the median curves are clearly separated. The curves obtained for other proportions than 1% and 2.5% are also very close to these median values and mainly within the statistical spread. This leads to the conclusion, that the quantity of interlayer bonds has only a minor influence on the compressive behavior if the bonds are located only at the edges of the crystallite, provided a certain number of interlayer bonds is surpassed.
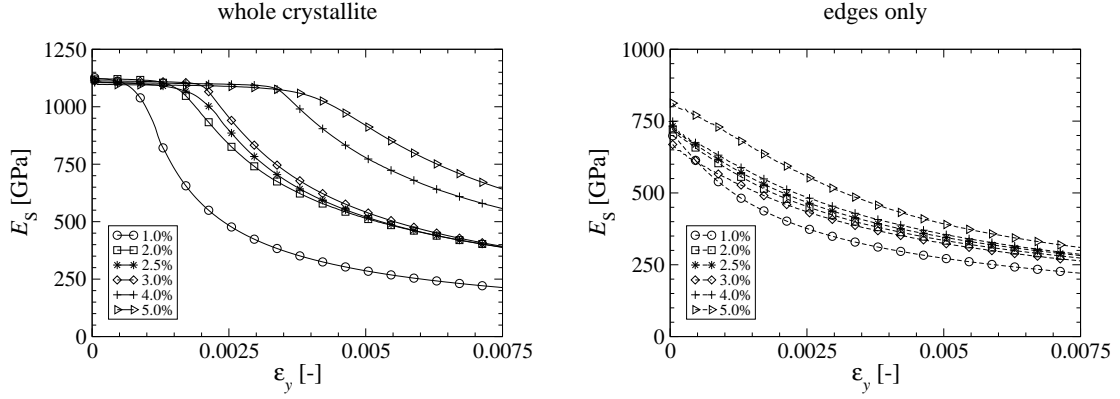
The effective secant modulus, E_S, of a crystallite is obtained from the secant

Figure 6.8: Load displacement diagram for different proportions of covalent interlayer bonds and for boundary conditions BC2.

Figure 6.9: Statistical spread of the reaction forces obtained for BC1 and different proportions of interlayer bonds.

Figure 6.10: Secant modulus E_S obtained for BC1 in dependence on the different proportions of covalent interlayer bonds. The figure on the left was already published in [147].

stiffness $K_S = F_y/u_y$ (see Figures 6.7 and 6.8) using

$$K_S = \frac{E_S A}{l} \ . \tag{6.5}$$

The parameters $A = L_{a\perp} \times L_c$ and $l = L_{a\|}$ are, as depicted in Figure 6.1, the initial cross section and initial height of the crystallite, respectively.

If the covalent interlayer bonds are randomly distributed over the whole crystallite the secant modulus E_S is equal to the tensile modulus of the crystallite and remains almost constant until buckling occurs, see Figures 6.10 (left) and 6.11 (left) respectively. After buckling E_S decreases significantly, where the decrease is stronger for a low proportion of interlayer bonds. The values obtained for E_S in the pre-buckling state range from 1076 GPa to 1158 GPa and are in good agreement with experimental values of 1140 ± 40 GPa obtained in [92]. Thus, values used for E, h, and ν are appropriate for describing the stiffness properties of carbon crystallites and, hence, also of graphene. The statistical spread of the values in the pre-buckling regime is small as shown in Figure 6.12 (left) and the initial value of E_S is independent of the boundary conditions used.

As shown in Figures 6.10 and 6.11 (right) significantly smaller initial values of E_S are obtained for crystallites when the interlayer bonds are only distributed along the edges. The values range from 670 GPa to 812 GPa and 763 GPa to 934 GPa for BC1 and BC2, respectively, and strongly differ from the experimental values reported in [92]. The differences between initial values are mainly within the statistical spread, see Figure 6.12 (right) and thus, E_S is independent of the amount of interlayer bonds and boundary conditions used, provided that at least a certain minimum number of interlayer bonds exists.

The results obtained for E_S for the different distributions of interlayer bonds indicate that the formation of these bonds occurs randomly over the whole crystallite and not only at the edges.
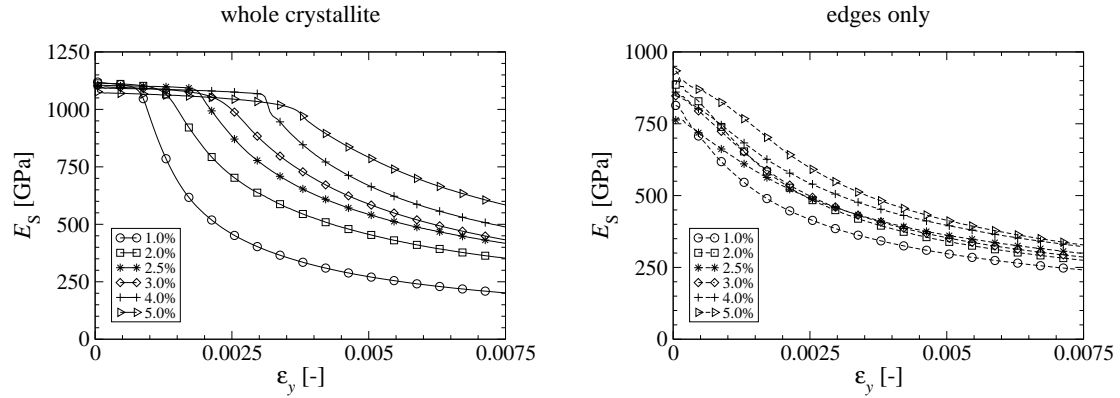
Figure 6.11: Secant modulus E_S obtained for BC2 in dependence on the different proportions of covalent interlayer bonds.
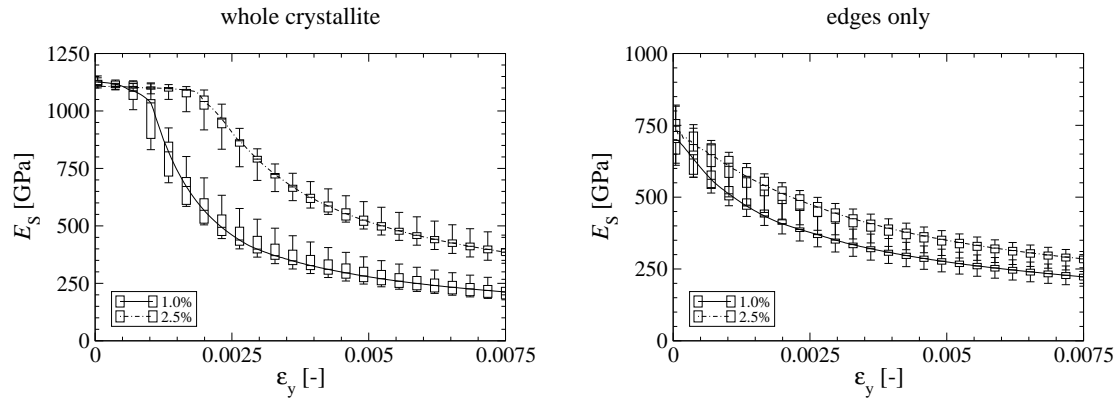
Figure 6.12: Statistical spread of the secant modulus E_S for BC1 and different proportions of covalent interlayer bonds.
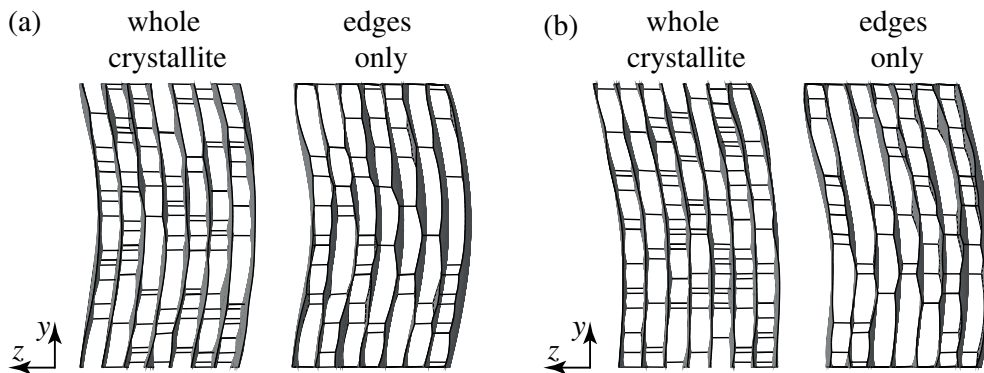
Figure 6.13: Deformations of carbon crystallites with 2.5% of covalent interlayer bonds at $u_y = 0.05\,\text{nm}$ for boundary conditions BC1 (a) and BC2 (b).

Figure 6.13 shows the deformations of crystallites containing 2.5% of interlayer bonds at $u_y = 0.05$ nm. The layers buckle in an interactive way, independent of the distribution of the bonds and the boundary conditions used. For boundary conditions BC1 the northern and southern parts of the crystallites deform in the same way, whereas for BC2 only the northern part shows a large deviation from the initially planar configuration of the layers. Whether, the interlayer bonds are distributed over the whole crystallite or only at the edges has no major influence on the observed deformations.

To obtain more information about crystallite buckling the mean azimuthal angles χ_S and χ_N during deformation of the crystallite are calculated using Equations (6.3) and (6.4), respectively.

Figures 6.14 to 6.17 (left) show the values evaluated for interlayer bonds that are randomly distributed over the whole crystallite. The azimuthal angles χ_S and χ_N remain constant until crystallite buckling occurs. If boundary conditions BC1 are used, both azimuthal angles, χ_S and χ_N, increase in a similar way after the onset of buckling, as shown in Figures 6.14 (left) and 6.15 (left), respectively. For BC2 the increase of χ_N in the post-buckling regime is of the same order of magnitude as for BC1, as can be seen from Figure 6.17 (left), whereas χ_S remains almost constant even after the onset of crystallite buckling, see Figure 6.16 (left).

With the bonds being only located at the edges, the azimuthal angels show no constant region and a monotonic increase during deformation can be observed (Figures 6.14 to 6.17(right)). Again χ_N remains almost constant for BC2.

Figures 6.18 and 6.19 show that the statistical spread of χ_S and χ_N are relatively large in the post-buckling regime. Thus, the results posses rather qualitative character. Although, the measured initial values of the azimuthal angles are higher in [91], there the azimuthal angles also show a constant region in the compressive area of the fiber. In [91] the increase of the azimuthal angles starts approximately for a compressive strain $\epsilon_y = 0.001$. This value is in good agreement with the results obtained with the computational models where the interlayer bonds are randomly distributed over the whole crystallite. For these models an increase in χ_S and χ_N occurs at compressive strains ranging from 0.001 to 0.003. This similarity between experiments and models is a further evidence that interlayer bonds are more likely to occur over the whole crystallite, where the tendency is towards lower amounts of interlayer bonds.

6.4 Conclusions

The compressive behavior of carbon crystallites making up PAN-based carbon fibers is investigated using the finite element method. With the used values of the elastic constants the effective elastic modulus of carbon crystallites could be well predicted. The effective elastic modulus of the crystallites is significantly reduced after the onset of crystallite buckling. This reduction of the modulus
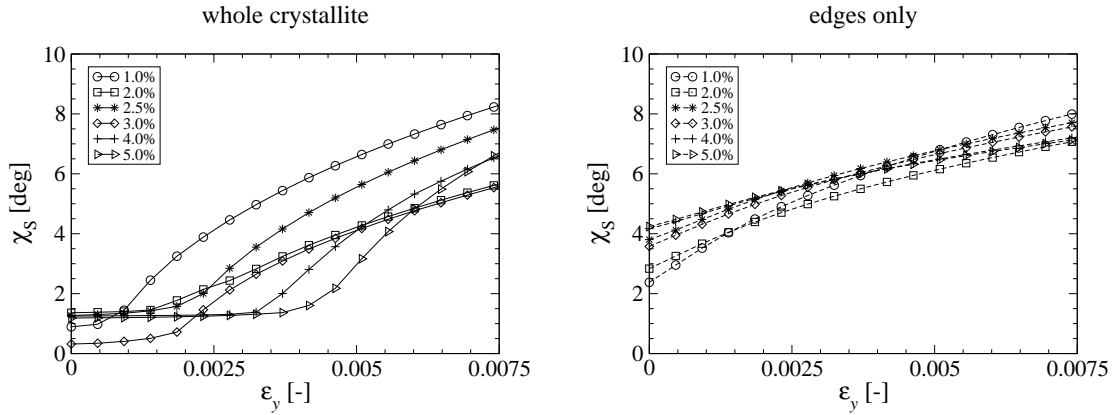
Figure 6.14: Azimuthal angle χ_S obtained for BC1 at the south side of the crystallites in dependence on the different proportions of covalent interlayer bonds.

Figure 6.15: Azimuthal angle χ_N obtained for BC1 at the north side of the crystallite in dependence on the different proportions of covalent interlayer bonds.

Figure 6.16: Azimuthal angle χ_S obtained for BC2 at the south side of the crystallite in dependence on the different proportions of covalent interlayer bonds.
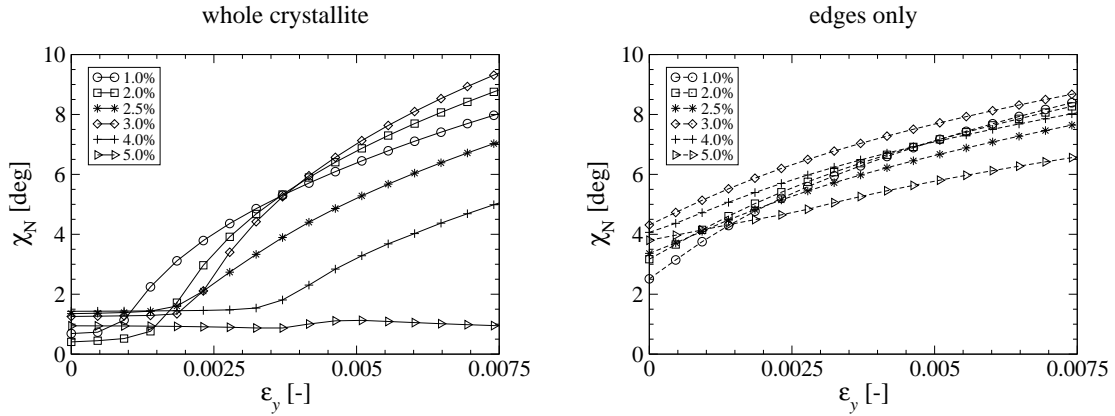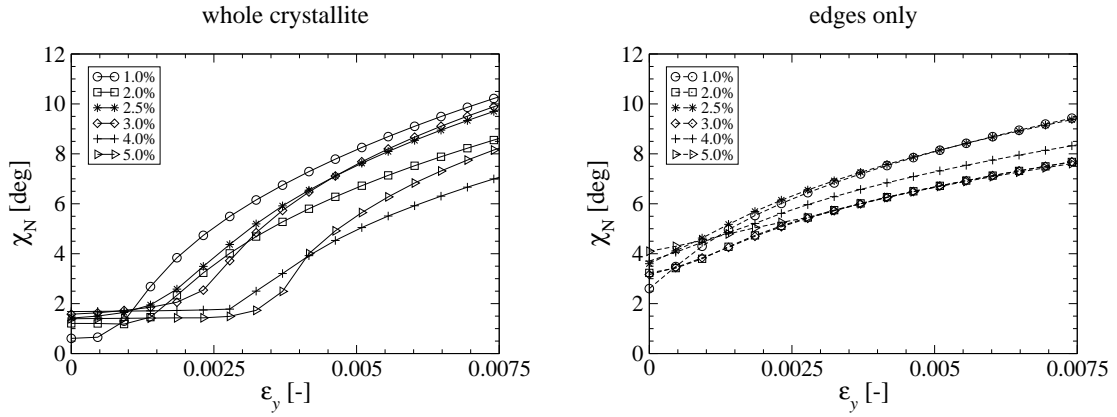
Figure 6.17: Azimuthal angle χ_N obtained for BC2 at the north side of the crystallite in dependence on the different proportions of covalent interlayer bonds.
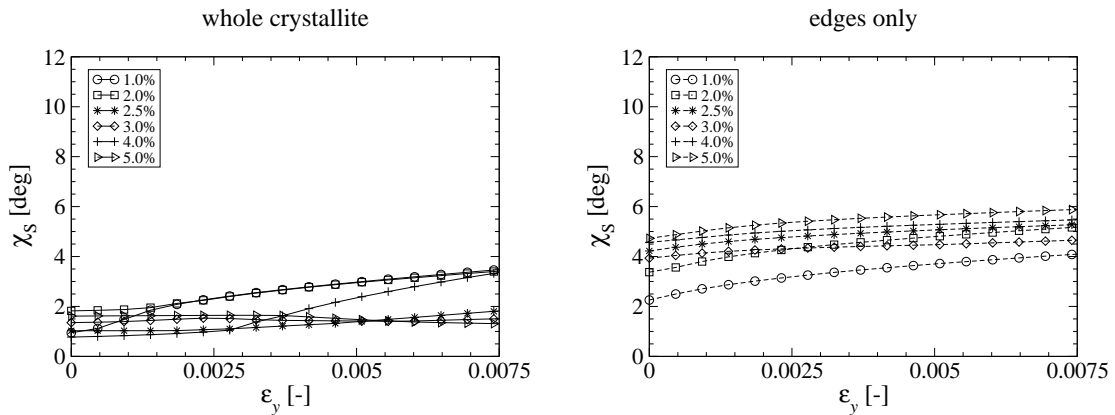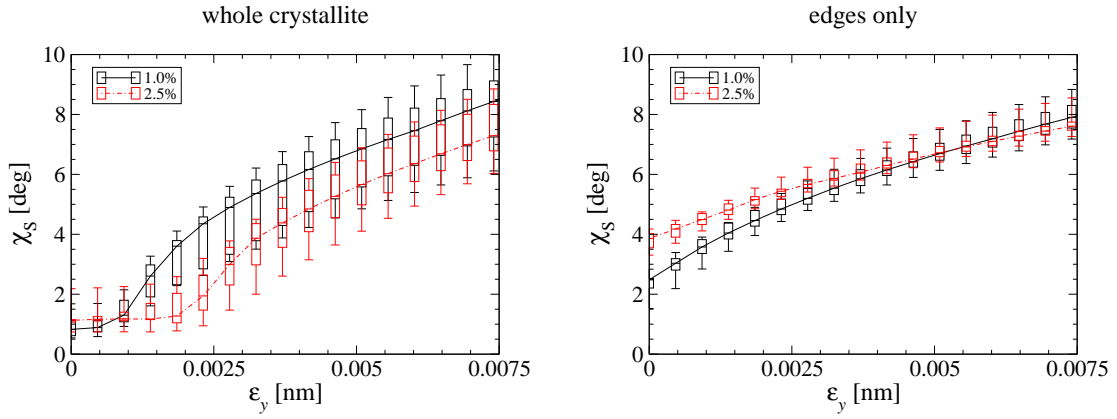

Figure 6.18: Statistical spread of the azimuthal angle, χ_S, at the south side of the crystallite obtained for BC1 and different proportions of cross links.

Figure 6.19: Statistical spread of the azimuthal angle, χ_N, at the north side of the crystallite obtained for BC1 and different proportions of cross links.
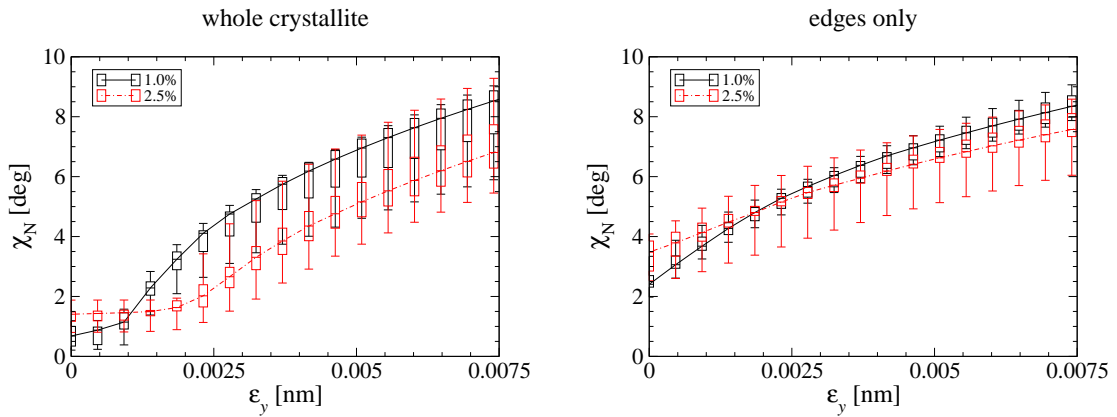
is responsible for the shift of the neutral axis observed experimentally for bent PAN-based carbon fibers. Covalent bonds randomly distributed over the whole crystallite have a stabilizing effect, whereas interlayer bonds distributed only at the edges cause bending deformations leading to a reduction of the axial stiffness of the crystallite already for small loads. Comparison with experimental results found in literature show that covalent interlayer bonds are more likely randomly distributed over the whole crystallite. A higher proportion of interlayer bonds distributed over the whole crystallite leads to a higher critical load for buckling, but has almost no influence on the post-buckling behavior of the crystallite. The results also show, that the layers forming the crystallite buckle in an interactive way. Layer separation due to buckling can be disregarded. Although, the present crystallite model includes some simplifications, the obtained results can serve as basis for further investigations regarding the compressive properties of carbon fibers.

Chapter 7

# Growth Limit of Carbon Onions

7.1   Introduction

In this chapter continuum mechanical shell models are used to address the question stated in Section 2.5 regarding the maximum size to which carbon onions can be grown. The growth of carbon onions and, hence, a possible growth limit of these particles are investigated. In contrast to [140] all considerations made are based on the assumption that the occurrence of a structural instability inhibits a further growth of the onion. This structural instability is supposed to be evoked by the formation of a further layer onto an already existing onion which is close to its stability limit. Parts of the results presented in this chapter have previously been published in [146].

7.2   Methodology

The boundary value problem arising when a new layer is added to an existing onion is solved using the finite element method. When a layer has been added a buckling analysis is performed in order to check whether or not the carbon onion has grown to its critical size. To save computational costs axi-symmetric shell models are used. The modeling assumptions made in the models and for the growing process are discussed in the following sections.

7.2.1   Axi-symmetric Shell Model

As the observed particles in [11, 12, 151] are almost perfectly spherical in their shape, the assumption of perfectly spherical onions seems to be admissible in the finite element model. In consequence of this assumption and due to axi-symmetry of the loading axi-symmetric models of N-layered carbon onions are
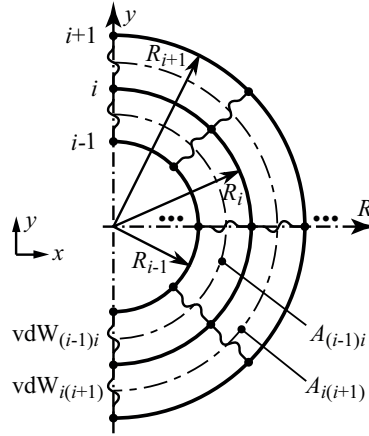
Figure 7.1: Axi-symmetric model of a carbon onion consisting of $N = i+1$ layers [146].

used in the computational stability analysis, see Figure 7.1, significantly reducing the computational requirements.

The assumption of axi-symmetry is justified as long as stable, i.e., pre-buckling states are considered. For a single thin-walled spherical shell subjected to a constant external pressure the lowest, and therefore, the relevant buckling eigenvalue appears with an extremely high multiplicity, see [39]. This high multiplicity of the eigenvalue leads to a high number of eigenfunctions all belonging to the one fundamental eigenvalue and being orthogonal to each other. Among these eigenfunctions several axi-symmetric ones can be found, which have the same physical relevance as non-axi-symmetric eigenfunctions. Regardless, whether an axi- or non-axi-symmetric buckling mode is considered, an imperfect shell most likely forms a single dimple in the post-buckling regime [39]. Thus, axi-symmetry is a reasonable assumption for the buckled configuration of a single spherical shell, too. Complete spherical shells filled with elastic media also show axi-symmetric buckling modes when subjected to external pressures [127]. A carbon onion can be envisaged as an outermost shell filled with an elastic medium which is formed by the layers below and the vdW interactions between the layers. Thus, using axi-symmetric shell models seems to be a reasonable approach to analyze the stability behavior of carbon onions.

As discussed in Chapter 4 the individual layers are modeled as thin shells with an elastic modulus $E = 4840\,\text{GPa}$, Poisson's ratio $\nu = 0.19$, and a thickness of $h = 0.075\,\text{nm}$ (taken from [114]) leading to a membrane stiffness of $Eh = 363\,\text{N/m}$ and a bending stiffness of $\frac{Eh^3}{12(1-\nu^2)} = 0.177\,\text{nN}\cdot\text{nm}$. This parameter set gives a good representation of the critical pressure of a single fullerene layer, see Chapter 4, and, thus, seems to be appropriate for investigating the stability of carbon onions, too. In Chapter 4 it is also shown that the hydrostatic stiffness of enforced spherical fullerenes is independent of the layer radius. Thus, all layers can be modeled by using the same elastic constants. Although the layers are modeled as

perfectly spherical it is assumed that their numbers of atoms are equal to those of fullerenes with the same mean radii. According to [139] the number of atoms forming fullerenes with icosahedral symmetry can be calculated using either $n_i = 60k^2$ or $n_i = 20m^2$, with $k, m \in \mathbb{N}$. The undeformed radii $R_i^{(0)}$ of layer i can then be calculated with Equation (5.28), where $a^{(0)} = 0.142\,\mathrm{nm}$ is used as carbon-carbon bond length in the undeformed configuration.

7.2.2   Excess Surface Energy

In curved nanostructures a curvature-dependent excess surface energy is present [63]. As a consequence of the surface energy a surface stress develops in the individual layers leading to a non-zero membrane stress state, even when no external loading is applied. This intrinsic membrane stresses may have an influence on the growth limit of carbon onions, and thus, are considered in the growth simulation.

The dependence of the excess surface energy on the layer radius R_i can be described using a power law [63]

$$E_i^{(S)} \propto R_i^{\beta} \ . \tag{7.1}$$

For $E_i^{(S)}$ being expressed in eV/bond the evaluated values for β range from $\beta = -1.40$ calculated with the whole fullerene models to $\beta = -2.51$ calculated with so called ring shell models; for more details see [63]. To be applicable in a continuum mechanical analysis $E_i^{(S)}$ has to be expressed in eV/(nm)^2 for which an average value of $\beta = -1.83$ can be obtained. As a consequence of the excess surface energy $E_i^{(S)}$ a surface stress $\bar{\sigma}_i^{(S)}$ (here in terms of a membrane force per unit area) develops as "plane hydrostatic" stress state in an onion layer according to the Shuttleworth equation [43]

$$\bar{\sigma}_i^{(S)} = E_i^{(S)} + \frac{\mathrm{d}E_i^{(S)}}{\bar{\varepsilon}_i^{(S)}} \ . \tag{7.2}$$

The parameter $\bar{\varepsilon}_i^{(S)}$ is the strain in each circumferential direction of the sphere in a small strain setting [43]. For a first estimate, usually the second term of the right hand side of Equation (7.2) can be neglected, and the relation

$$\bar{\sigma}_i^{(S)} = E_i^{(S)} \ , \tag{7.3}$$

is used. Note that $E_i^{(S)}$ and $\bar{\sigma}_i^{(S)}$ are physically different quantities but have the same units, viz force per unit length.

In the finite element model the surface stress $\bar{\sigma}_i^{(S)}$ is taken into account by applying a corresponding inwards oriented mechanical pressure p_i^{S} onto each of the spherical layers, which is determined according to [43] as

$$p_i^{\mathrm{S}} = \frac{2\bar{\sigma}_i^{(S)}}{R_i}, \tag{7.4}$$

resulting, with Eqn. (7.1), in

$$p_i^{\mathrm{S}} = 2A \, R_i^{-2.83}. \tag{7.5}$$

The factor $A \approx 0.36 \, \mathrm{nN} \, \mathrm{nm}/(\mathrm{nm})^{0.17}$ is estimated form Fig. 7 in [63]. As can be seen from Equation (7.5) the pressure p_i^{S} acting onto the onion layers decreases fast with increasing layer radius and, thus, is only of relevance for the innermost layers of a carbon onion.

7.2.3 Growth of carbon onions

For investigating the growth limit of carbon onions the growth process has to be represented within the computational model. As discussed in Section 2.5 several techniques are available for producing carbon onions, e.g., the high-temperature annealing of nano-diamonds [81, 148, 70] or the high pressure transformation of graphite [19]. If the carbon onions are produced by high-temperature annealing of nano-diamonds the transformation starts at the boundaries of the nano-diamond [81, 148]. Atomistic simulations of this technique have shown that the diameter of the outermost layer is almost the diameter of the initial nano-diamond [94]. In contrast, carbon onions produced by high pressure transformation of single-crystal graphite [19] and from coal by using a radio frequency plasma reactor [40] grow from the inside to the outside.

Starting with the outermost layer in growth simulations seems to be problematic as the size of the carbon onion at its growth limit is not known a priori and also the size of the remaining diamond core after the formation of a layer is an unknown parameter. Therefore, it is assumed that the carbon onion grows layer-by-layer from the inside to the outside. For the first, i.e., the innermost layer the C60 fullerene is used as this is the smallest fullerene to be thermodynamically stable [79]. This layer is assigned the layer index $i = 1$. Further layers are deposited one after the other. Each new layer $i = N$ with radius $R_N^{(0)}$ in the stress free configuration is concentrically located outside onto the surface of the current onion consisting of $N - 1$ layers. The pressure p_N^{S} is applied and kept constant during the whole growth simulation. Usually, the interlayer distance $R_N^{(0)} - R_{N-1}$ between layers N and $N - 1$ is not equal to the equilibrium distance α_{eq} of the vdW bonding being active between neighboring layers. Thus, the new layer N does not exactly fit the onion. Due to this misfit the vdW interactions lead, in combination with the surface stress, to either tensile or compressive stresses in this layer. Additionally, the stresses in the layers underneath are changed, too. The new equilibrium configuration of the N-layered onion is calculated in a geometrically nonlinear analysis step. This new configuration is evaluated regarding its stability by performing a buckling eigenvalue analysis. Detailed information about the eigenvalue analysis can be found in Appendix A. The formulation of

the eigenvalue problem depends on the type of model used to describe the vdW interactions between adjacent layers.

Linearized VdW Model

The vdW interactions between neighboring layers are modeled using linear spring elements, for details see Section 5.6.1. The stiffness of the individual springs is calculated using Equation (5.58), where the axi-symmetry of the finite element model is considered. The parameters of the vdW interactions are chosen as $C_{33} = 36.5$ GPa [72] and $\sigma = \alpha_{eq} = 0.3415$ nm [98]. Although, the interlayer distance $R_N^{(0)} - R_{N-1}$ between layers N and $N-1$ is usually not equal to the equilibrium distance α_{eq} the spring elements are introduced with a stress free length of $\alpha_{(N-1),N}^{(0)} = R_N^{(0)} - R_{N-1}$. The vdW interactions due do $\alpha_{(N-1),N}^{(0)} \neq \alpha_{eq}$ can be calculated using Equation (5.59) and are, like the surface stress being active in layer N, considered as perturbation loads in the buckling eigenvalue prediction, see Appendix A. The corresponding eigenvalue problem reads

$$\left(\underset{\approx}{\mathbf{K}}_{N-1} + \bar{\lambda}_N^j \Delta \underset{\approx}{\bar{\mathbf{K}}}_N \right) \underset{\sim}{\bar{\mathbf{\Phi}}}_N^j = \underset{\sim}{\mathbf{0}} \ . \tag{7.6}$$

In Equation (7.6) $\underset{\approx}{\mathbf{K}}_{N-1}$ is the stiffness matrix of the system with N layers including the effects of the surface stress and the vdW forces acting in the configuration of the carbon onion with $N-1$ layers. The matrix $\Delta \underset{\approx}{\bar{\mathbf{K}}}_N$ represents the contribution of the vdW interactions between layer $N-1$ and N and the surface stress in layer N. The parameters $\bar{\lambda}_N^j$ are the eigenvalues and $\underset{\sim}{\bar{\mathbf{\Phi}}}_N^j$ are the corresponding eigenfunctions. The smallest eigenvalue $\bar{\lambda}_N^1$ is the factor by which the contribution of the N-th layer has to be multiplied in order to bring the onion consisting of N layers to an unstable state. Thus, layer N cannot be added without surpassing the stability limit if $\bar{\lambda}_N^1 < 1.0$. The corresponding eigenvector $\underset{\sim}{\mathbf{\Phi}}_N^1$ characterizes the buckling mode of the N-layered carbon onion.

Nonlinear VdW Model

The vdW model described in Section 5.6.2 is used to consider the nonlinear behavior of the vdW interactions. Two different vdW interfaces, M1 and M2, are defined using Equations (5.5) and (5.11), respectively, where $C_{33} = 36.5$ GPa [72, 183] is used for M1. For the required Lennard-Jones parameters σ and ϵ two different sets, S1 ($\sigma = 0.3415$ nm and $\epsilon = 0.00239$ eV [98]) and S2 ($\sigma = 0.3345$ nm and $\epsilon = 0.00319$ eV [176]) are taken from literature. The two vdW models M1 and M2 in combination with the parameter sets S1 and S2 lead to four different vdW models, see Table 7.1.

In contrast to the linearized vdW model the vdW interactions due to the difference $\alpha_{(N-1),N}^{(0)} \neq \alpha_{eq}$ become active directly after the new layer is added. They are, thus, not available as perturbation loads in the eigenvalue buckling prediction. To

Table 7.1: Nonlinear vdW models used in the stability analysis of carbon onions.

Model	Equation	σ	ϵ
M1S1	(5.5)	$0.3415\,\mathrm{nm}$	$0.00239\,\mathrm{eV}$
M2S1	(5.11)	$0.3415\,\mathrm{nm}$	$0.00239\,\mathrm{eV}$
M1S2	(5.5)	$0.3345\,\mathrm{nm}$	$0.00319\,\mathrm{eV}$
M2S2	(5.11)	$0.3345\,\mathrm{nm}$	$0.00319\,\mathrm{eV}$

overcome this problem an external pressure $p_N^{(\text{ext})}$ is applied to the outermost layer N in the stability analysis. The pressure $p_N^{(\text{ext})}$ is defined as the critical pressure of this layer without the supporting layers underneath and, thus, reads [118]

$$p_N^{(\text{ext})} = \frac{2Eh^2}{\sqrt{3(1-\nu^2)}(R_N^{(0)})^2} \ , \tag{7.7}$$

where $R_N^{(0)}$ is the radius of layer $i = N$. The choice of $p_N^{(\text{ext})}$ as external pressure is not based on any necessity but provides information about the effect of bedding due to the inner layers.

The corresponding eigenvalue problem is then defined as

$$\left(\underset{\approx}{\mathbf{K}}_N + \bar{\lambda}_N^j \Delta\underset{\approx}{\bar{\mathbf{K}}}_N\right) \underset{\sim}{\bar{\mathbf{\Phi}}}_N^j = \underset{\sim}{\mathbf{0}} \tag{7.8}$$

with $\underset{\approx}{\mathbf{K}}_N$ being the stiffness matrix of the N-layered onion in its equilibrium state including the vdW interactions. The matrix $\Delta\underset{\approx}{\bar{\mathbf{K}}}_N$ represents the change in the stiffness of the onion due to the external pressure $p_N^{(\text{ext})}$. The variables $\bar{\lambda}_N^j$ and $\bar{\mathbf{\Phi}}_N^j$ again are the eigenvalues and the corresponding eigenvectors, respectively. For this model the smallest eigenvalue $\bar{\lambda}_N^1$ is the factor by which the pressure $p_N^{(\text{ext})}$ on the outermost layer has to be multiplied to bring the N-layered onion to a critical state. In contrast to the linarized model, $\bar{\lambda}_N^1 = 0$ indicates that the carbon onion has grown to its critical size, whereas $\bar{\lambda}_N^1 <= 1$ means that the critical pressure of the onion is equal to or smaller than the buckling pressure of the outermost layer. For the linearized vdW model the eigenvalue analysis is used to check, if another layer can be added without provoking a structural instability. For the nonlinear model it is checked if an existing onion is still stable when its outermost layer is subjected to an external pressure $p_N^{(\text{ext})}$. Thus, if $\bar{\lambda}_N^1 = 0$ no external pressure is required to provoke a structural instability. The section forces introduced due to the mutual accommodation of the layers are sufficient to evoke buckling and, hence, the onion has grown to its critical size.

7.3 Results

7.3.1 Linearized VdW Model

For the linearized vdW model adding a further layer to the onion requires only a single linear solution step, leading to low computational requirements. Thus, this model is used to check if the surface stress has an influence on a possible growth limit of carbon onions. Furthermore, the number of atoms n_i forming the new layer to be added is calculated in two different ways. (i) It is assumed that every new layer is an icosahedral fullerene where $n_i = 60 \, i^2$, with i being the layer index. (ii) The new layer belongs either to the group of $n_i = 60 \, m^2$ or $n_i = 20 \, k^2$ fullerenes ($k, m \in \mathbb{N}$), where the fullerene with the smallest accommodation effort is chosen. In the following (i) and (ii) are referred to as pure and mixed configuration, respectively.

The results of the eigenvalue buckling prediction of the pure and mixed configurations are depicted in Figures 7.2 (left) and (right), respectively. The figures show the lowest, i.e., the relevant, buckling eigenvalue $\bar{\lambda}_N^1$ in dependence on the number of layers N forming the carbon onion. An eigenvalue $\bar{\lambda}_N^1 > 1.0$ denotes a stable equilibrium configuration of the onion. The eigenvalue curves for the pure and mixed configurations are rather similar. In both cases $\bar{\lambda}_N^1$ approaches 1.0 if the onion has grown to a size of $N = N_{\mathrm{crit}} = 23$, whether or not the surface stress is considered. An influence of the surface stress on the obtained values of $\bar{\lambda}_N^1$ can only be observed for carbon onions consisting of fewer than eight layers. If the surface stress is not considered a negative eigenvalue peak occurs for $N = 2$. This peak is due to a relatively high tensile section force f_1 in layer $i = 1$ and a rather small compressive section force f_2 in layer $i = 2$, see Figure 7.4 left and right, respectively, and has no physical relevance. The section forces are calculated according to Equation 4.13. The indices of the spatial directions can be omitted as the section forces are independent of the direction due to spherical symmetry.

The corresponding buckling mode for $N = N_{\mathrm{crit}}$ of the pure configuration is shown in Figure 7.3. Merely the outer layers buckle in an interactive way, whereas the inner layers remain almost unaffected. The observed buckling mode is comparable to buckling modes observed for complete spheres filled with elastic media [127]. This confirms the assumption that a carbon onion behaves comparably to a spherical shell filled with an elastic medium.

The difference between pure and mixed configurations becomes obvious if the section forces f_i in the layers (Figure 7.4) and the resulting interlayer distances α_{ij} (Figure 7.5) are considered.

Figure 7.4 shows the evolution of the section forces f_i in the individual layers during the growth of the onion. Both configurations give the same results for the section forces for an onion consisting up to six layers. Thus, the six inner layers of the mixed configuration belong to the group of $n_i = 60 \, i^2$ fullerenes. For both configurations $f_1 = 0$ for $N = 1$ if the surface stress is neglected. Adding a second
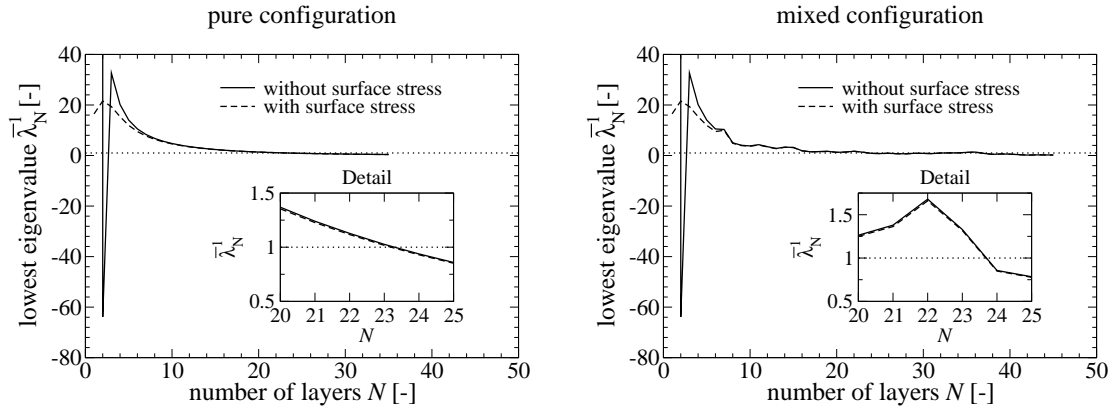
Figure 7.2: Lowest eigenvalue $\bar{\lambda}_N^1$ depending on the number of layers N forming a carbon onion for the pure (left) and mixed (right) configurations. Details of the stability limit can be found in the insets. The figure on the left was already published in [146].
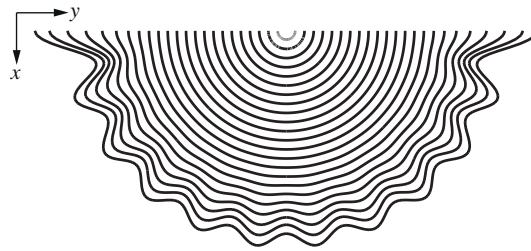
Figure 7.3: Buckling mode of a carbon onion corresponding to the lowest eigenvalue $\bar{\lambda}_N^1$ at the growth limit $N_{\mathrm{crit}} = 23$ [146].
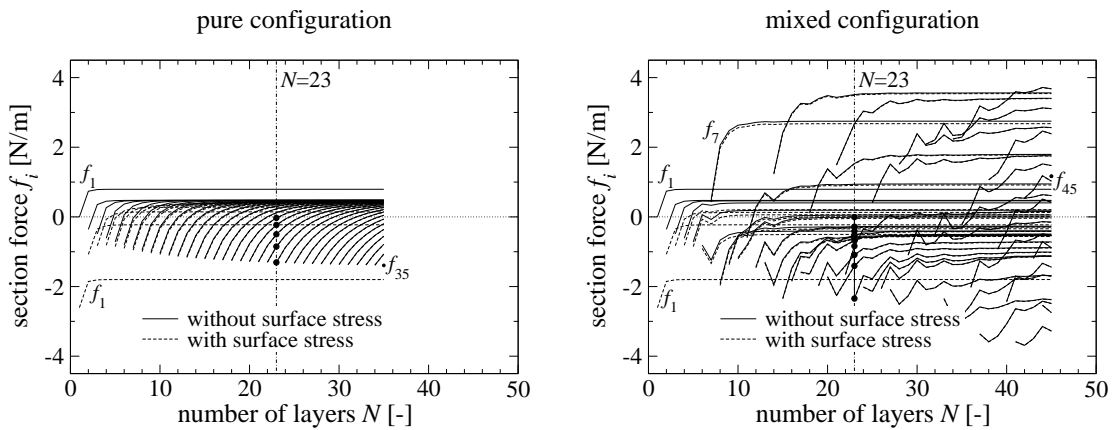

Figure 7.4: Section forces f_i in the i-th layer of an N-layered onion for the pure (left) and mixed (right) configurations. Negative values of f_i denote compression. Layers under compression are marked with • at the critical configuration $N = 23$.

layer $i = N = 2$ leads to a tensile membrane stress in layer $i = 1$ whereas layer $i = 2$ is under compression. If a third layer $i = 3$ is added a tensile membrane stress develops in layer $i = 2$ and layer $i = 3$ is subjected to compressive section forces. The section force f_1 in the innermost layer is almost unaffected by the formation of the third layer and also by the further growth of the onion. In case of the pure configuration each newly added layer k is first subjected to compressive section forces f_k whether or not the surface stress is considered. During further growth of the onion the compression section forces are reduced and if sufficient layers are added tensile section forces develop in layer k. Thus, only the outer layers of the onion are under compression. The influence of the formation of a new layer on the section forces of the layers underneath vanishes towards the center. At the growth limit $N = N_{\mathrm{crit}}$ only the four outer layers are under compression for an onion of the pure configuration if the surface stress is not taken into account, see Figure 7.4 (left).

Considering the surface stress leads to a relatively large compressive section force in the innermost layer, which is reduced after the second layer is added but does not become a tensile section force during the growth of the onion. In this case also the second layer remains under compression during the growing process. The influence of the surface stress on the section forces f_i vanishes fast with increasing size of the layers and and for layers with $i > 8$ the section forces are unaffected by the surface stress. Although the surface stress introduces substantial compressive section forces in the two innermost layers it has no influence on the growth limit of the onion. The pressure, $p_{\mathrm{crit}} = \frac{2Eh^2}{\sqrt{3(1-\nu^2)R^2}}$ required to introduce buckling in a layer with radius R scales with $\frac{1}{R^2}$. Thus, layers in the outer region of the onion are much more sensitive to buckling than those in the inner region. The radius of the outermost layer R_{23} is about 23 times the radius of the innermost layer $R_1 \approx 0.341\,\mathrm{nm}$, and therefore, the critical pressure of the innermost layer is about 530 times higher, than that of layer $i = 23$. From Figure 7.4 it can bee seen that the compressive section force f_1 is at most two times higher than the section force in the outer layer. Thus, the influence of the compressive section forces in the inner layers, and hence, the surface stress is negligible and buckling is always introduced in the outer region of the onion.

For the mixed configuration (Figure 7.4, right) a newly added layer is not a priori under compression, see, e.g., layers $i = 7, 15, 21$. In comparison to the pure configuration 11 layers are under compression at the stability limit. Not all of them are located in the outer region of the onion. The absolute values of the compressive and tensile section forces are generally higher than those observed for the pure configuration. The reason for the difference in the section forces between the different configurations can be found in the interlayer distances $\alpha_{i,j}$ between layers i and $j = i + 1$. Figure 7.5 shows the current interlayer distances α_{ij} after layer N has been added and the N-layered onion has reached its new equilibrium configuration.
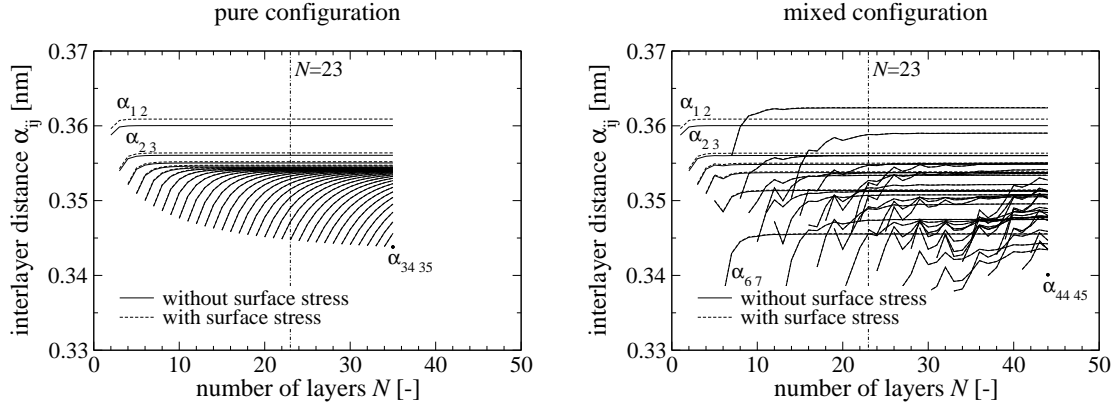
Figure 7.5: Inter-layer distances $\alpha_{i,j}$ between layers i and $j = i + 1$ depending on the number of layers N for the pure (left) and mixed (right) configurations.

For the pure configuration the interlayer distance $\alpha_{ij}^{(0)} = R_j^{(0)} - R_i$ $(i = j - 1)$ between the newly formed layer $j = N$ and the onion consisting of $N - 1$ layers is always larger than the equilibrium distance of the vdW interactions, $\alpha_{\mathrm{eq}} = 0.3415\,\mathrm{nm}$. This leads to attractive vdW forces between the $(N-1)$-layered onion and the new layer, introducing compressive section forces in the new layer and tensile section forces in the $N - 1$ layers forming the onion. As a consequence also the interlayer distances in the outer region of the $(N - 1)$-layered onion increase, whereas the interlayer distances in the inner region remain almost unaffected. All interlayer distances α_{ij} of an N-layered onion in its equilibrium state are larger than α_{eq}, and also larger than the values reported in [10], Figure 7.5 (left). The the interlayer distances decrease from the inner region of the onion to the outer region, which is in contrast to experimental observations, see e.g., [10]. However, also in [13] a decrease in layer spacing from the inner region to the outer region of a carbon onion is calculated using analytical continuum mechanical models. The surface stress has an influence on the interlayer distances $\alpha_{1\,2}$ and $\alpha_{2\,3}$ only. The interlayer distances in the outer region of an N-layered onion are completely unaffected by the surface stress.

For onions of the mixed configuration (Figure 7.5, right) the interlayer distances α_{ij} do not decrease continuously from the inner region to the outer region. Generally, the formation of a layer j from the series $n_j = 20\,k^2$ leads to a smaller interlayer distance α_{ij} than the formation of a layer belonging to the $n_j = 60\,m^2$ series. The mixture of interlayer distances smaller and larger than α_{eq} leads to the waviness of the interlayer distance curves (Figure 7.5, right) and as a consequence also to wavy section force curves (Figure 7.4, right) evaluated during the growth of the onion. For example the interlayer distance $\alpha_{6\,7}$ is smaller than α_{eq}, leading to repulsive vdW interaction forces between layer $i = 7$ and the six-layered onion underneath. This introduces compressive section forces in the layers forming the onion and tensile section forces in the added layer $i = 7$, see Figure 7.4

(right). Adding the next layer $i = 8$ leads to an interlayer distance $\alpha_{7\,8}$ far larger than α_{eq}, introducing tensile section forces in the onion and a compressive section force in layer $i = 8$. The interlayer distance $\alpha_{7\,8}$ of the mixed configuration is also larger than the same interlayer distance of the pure configuration, and hence, the compressive section force introduced in layer $i = 8$ is larger for the mixed configuration.

Although, the interlayer distances and section forces obtained for the pure and mixed configurations are different, both configurations give quite the same growth limit $N_{\mathrm{crit}} = 23$ layers. This growth limit is significantly lower than the number of layers found in reality [10, 12, 19, 163, 185]. The reason for the difference between experimental observations and the simulated values of N_{crit} is the rough simplification of the vdW interactions. The linearized vdW model is only valid for interlayer distances α_{ij} close to α_{eq}, but the obtained interlayer distances differ considerably from α_{eq}, see Figure 7.5. If α_{ij} is larger than α_{eq} the linearized vdW model overestimates the stiffness of the vdW bedding, and, as a consequence, the vdW interaction forces between the layers. Thus, the vdW induced section forces in the layers are too high. Since the compressive section forces in the outer layers are responsible for the occurrence of the instability, overestimating these forces introduces the instability too early. This leads to a value N_{crit} which is much lower than the experimentally observed number of layers.

Nevertheless, it was possible to show that the occurrence of a structural instability most likely limits the size of carbon onions. The vdW interactions, leading to self-equilibrating stress states in the layers due to mutual accommodation, have shown to be responsible for the loss of stability, whereas the curvature induced surface stress plays only a minor role. Using a nonlinear vdW model should lead to higher values of N_{crit}.

7.3.2 Nonlinear VdW Model

The results obtained with the linear vdW model show that the vdW interactions due to the misfit of the added layers are responsible for the occurrence of a structural instability. To overcome the shortcomings of the linear vdW model nonlinear vdW interfaces are used in the following. As shown, the surface stress has no influence on the growth limit of carbon onions, and thus, is neglected. Furthermore, it seems to be of no importance if the layers forming the carbon onion belong to the group of $n_i = 60\, i^2$ fullerenes or if the onion is a mixture between fullerenes of the $n_i = 60\, m^2$ and $n_i = 20\, k^2$ series. Therefore, only onions formed by $n_i = 60\, i^2$ fullerenes are considered.

As discussed in Section 7.2.3 four different nonlinear vdW interfaces (M1S1, M1S2, M2S1, and M2S2) are used to describe the vdW interactions between adjacent onion layers. The vdW models M1 and M2 used to define the interfaces were derived for plane graphene and give the same vdW pressure on opposite faces
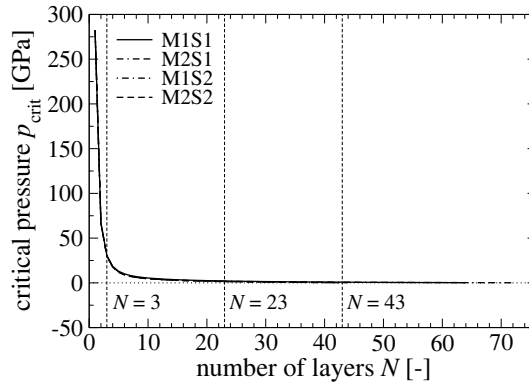
Figure 7.6: Estimated critical pressure p_{crit} required to initiate the loss of structural stability of the carbon onion depending on the number of layers, N forming the carbon onion and the vdW interface used.

of adjacent layers. This is not correct for curved nanostructures, where the vdW pressures on opposite faces of neighboring layers are different and depend – besides the interlayer distance – also on the radii of the layers [98, 145]. However, the difference between the pressures acting on the opposite faces vanishes fast with increasing layer radii. Thus, M1 and M2 give good approximations for layers in the outer region of the onion. In conjunction with the surface stress it was shown in the previous section, that the stress state in the innermost layers has no influence on the the growth limit of the onion. It can be concluded that also the incorrect representation of the vdW pressures on the inner layers due to M1 and M2 is of no relevance to the growth limit.

The pressures p_{crit} which have to be applied to the outer layer to bring a N-layered onion to its stability limit are depicted in Figure 7.6. A value $p_{\text{crit}} = 0.0\,\text{GPa}$ indicates that the onion has reached its growth limit. For all four interfaces the obtained critical pressures are almost equal and 'smoothly' approach the value of $0.0\,\text{GPa}$. From this curves it is hard to distinguish, whether or not the onion has reached its critical size.

More information can be gained from the results of the eigenvalue prediction given by Equation (7.8). Figure 7.7 shows the eigenvalue curves obtained for the different vdW models. A value of $\lambda_1 = 0.0$ would indicate that the onion has reached its critical size, but it is not reached by any of the eigenvalue curves. The problem becomes mathematically ill-conditioned for carbon onions which are close to their critical size, making it difficult to obtain a solution for the underlying boundary value problem. However, from the tendency of the curves it can be guessed that the onion will reach its stability limit by adding a few more layers. The critical number of layers obtained with the nonlinear models are significantly larger than $N_{\text{crit}} = 23$ obtained with the linearized model. Thus, considering the nonlinear character of the vdW interactions is crucial if the stability of carbon
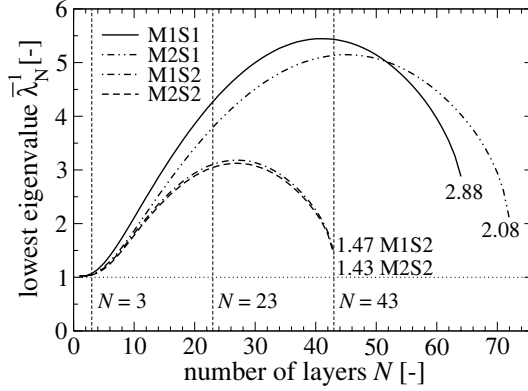
Figure 7.7: Lowest eigenvalue $\bar{\lambda}_N^1$ for different vdW interface models in dependence on the number of layers N forming a carbon onion.

onions is investigated.

The corresponding buckling patterns of the onions at their critical size are depicted in Figure 7.8 and are nearly the same for all interface models. As for the linearized model, the outer layers buckle in an interactive way, whereas the inner layers remain almost unaffected. The buckling patterns are not as wavy and show dominant dimples at the poles. These dimples are an implication of small imperfections introduced by the interfaces at the poles, and should not be overrated. The results again confirm the assumption that carbon onions behave like thin shells (the outer layer) filled with an elastic medium (the layers underneath linked by the vdW interactions).

M1S1 is the linear counterpart of the linearized model and leads to $N_{\text{crit}} \approx 64$ layers, see Figure 7.7. The highest number of layers $N_{\text{crit}} \approx 72$ is reached with the interface model M1S2. The models M2S1 and M2S2 give almost equal eigenvalue curves and both lead to $N_{\text{crit}} \approx 43$ for the critical layer number. The different numbers of layers obtained by the four vdW interfaces are due to the parameters and underlying vdW models used.

The current interlayer distances α_{ij} of an N-layered onion in its equilibrium state are depicted in Figure 7.9. Figure 7.10 shows the corresponding section forces f_i being active in the layers. Generally, the obtained interlayer distances are larger than the values of α_{eq} obtained for the interface models, see Figure 7.9 and a newly added layer k is always subjected to compressive section forces (Figure 7.10). The values of initial compressive section forces in a newly added layer increase with the size of the onion, whereas the interlayer distance between the new layer and the onion underneath becomes smaller. Adding further layers reduces the compressive section force in layer k and leads to an increase of the interlayer distance $\alpha_{k\ k-1}$. If sufficient layers are added a tensile section force develops in layer k. However, for a certain size of the onion adding a new layer has no influence on the section force in layer k and on the interlayer distance $\alpha_{k\ k-1}$. The number of layers which
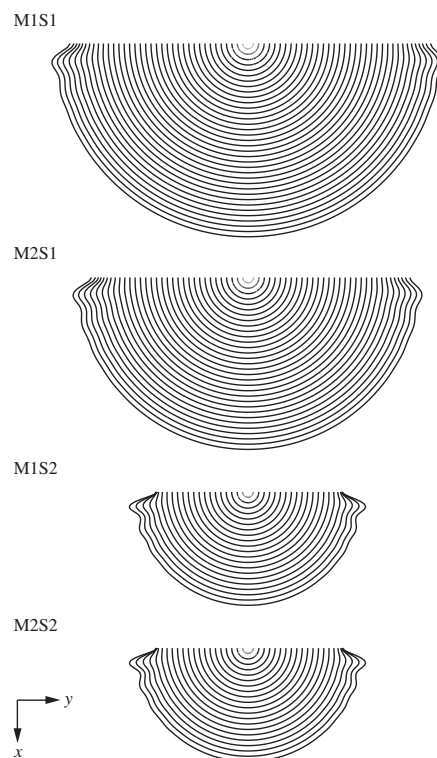
Figure 7.8: Buckling modes corresponding to the lowest eigenvalues $\bar{\lambda}_N^1$ for the different vdW interface models. Only odd-numbered layers are shown for the sake of simplicity.
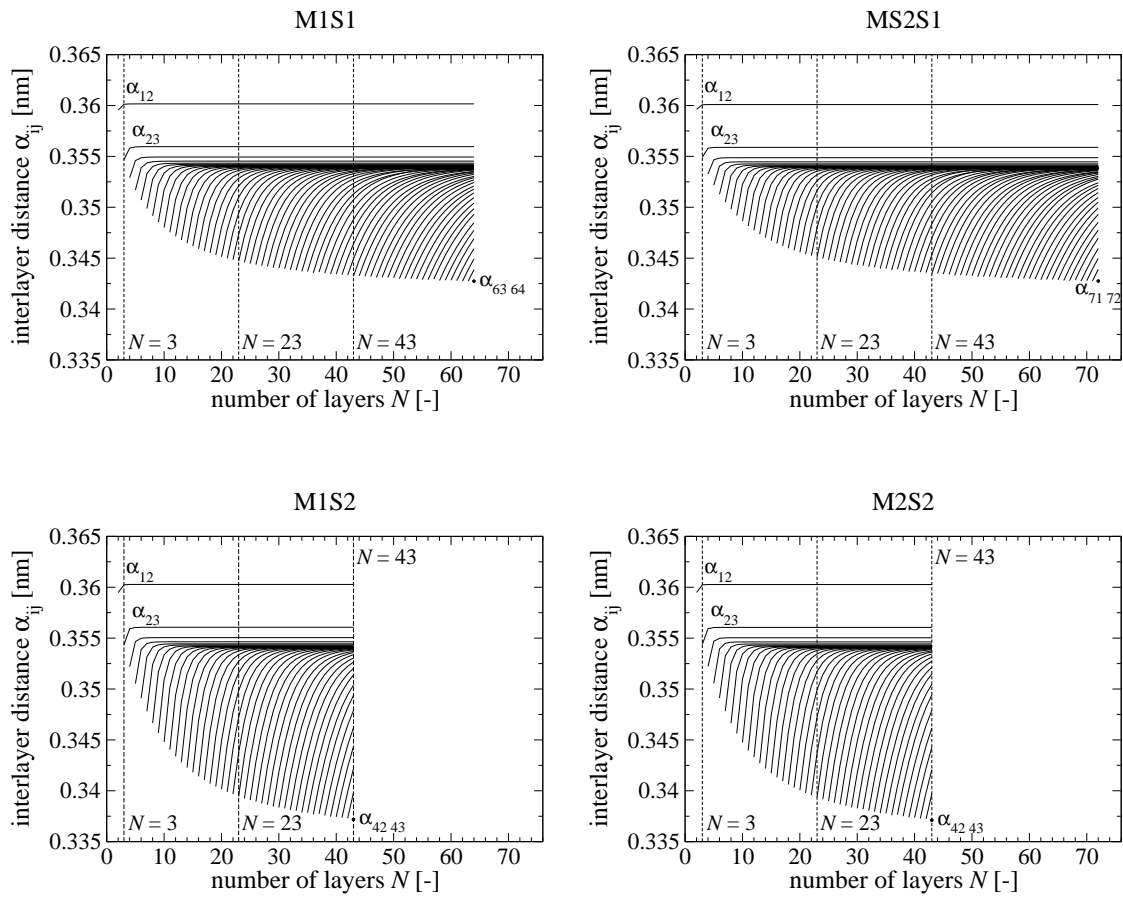
Figure 7.9: Interlayer distances $\alpha_{i,j}$ between layers i and $j = i + 1$ depending on the number of layers N for the vdW interface models M1S1, M2S1, M1S2, and M2S2.

have to be added until a tensile section force develops in layer k or until this layer remains unaffected by the formation of a new layer depends on the position of the layer k in the onion. For a layer close to the center fewer further layers are required (e.g. f_3 unaffected for $N > 5$) than for a layer closer to the outer region (e.g. f_{23} unaffected for $N > 40$). With increasing size of the onion also the number of layers under compression becomes higher, which is illustrated in Figure 7.11. As no surface stress is considered, only layers in the outer region are subjected to compressive section forces.

All interface models behave qualitatively the same way, but show substantial quantitative differences. M2S1 results in slightly larger interlayer distances α_{ij} and smaller section forces f_i than M1S1, although both models use the same α_{eq} of 0.3415 nm. The reason for the differences in the compressive section forces and interlayer distances are the different compressive constants $C_{33}/6 = 6.08$ GPa and $C_0 = 4.79$ GPa of M1S1 and M2S1, respectively. The higher value of $C_{33}/6$ leads to higher vdW pressures, and hence to a larger deformations ΔR_i and ΔR_j of neighboring layers i and $j = i + 1$, if the same initial interlayer distances $\alpha_{i\,j}^{(0)}$ are assumed. Thus, higher compressive section forces are introduced in a newly added layer $j = N$ for M1S1. As a further consequence more layers are under compression for M1S1 if the onion has reached a certain size, e.g. for $N = 43$ eight layers are under compression for M1S1 but only seven for M2S1, see Figure 7.10. The higher number of layers being under compression in combination with the higher magnitudes of the compressive section forces result in the lower growth limit observed for M1S1.

For the vdW interfaces M1S2 and M2S2 the equilibrium vdW interlayer distance is $\alpha_{eq} = 0.3345$ nm and, thus, smaller than for the other two interlayer models. The vdW parameters chosen for S2 give almost equal values of $C_{33}/6$ and C_0, see Section 5.3. Therefore, the difference between M1S2 and M2S2 lies only in the exponents of the pressure-distance relations described by Equations (5.5) and (5.11). As the results of the eigenvalue problem of both models are almost equal, it can be concluded that the different exponents play only a minor role. Both models also give almost equal results for the interlayer distances $\alpha_{i,j}$ and the section forces f_i in an N-layered onion, see Figures 7.9 and 7.10, respectively. The section forces obtained for parameter set S2 are significantly higher than those obtained for S1. The higher section forces are mainly due to the smaller equilibrium interlayer distance α_{eq} as the compressive constant is the same as that used in M1S1.

As mentioned above, the initial distance $\alpha_{ij}^{(0)}$ between a newly added layer and the layer underneath is always larger than α_{eq}. From Equations (5.5) and (5.11) one finds that if $\alpha_{ij}^{(0)} > \alpha_{eq} = \sigma$ parameter set S2 leads to higher values of the vdW pressure even if the same compressive constant as in M1S1 is obtained. Thus, higher values of the vdW interaction pressure implicates higher section forces introduced in the interacting layers. The higher compressive section forces in the
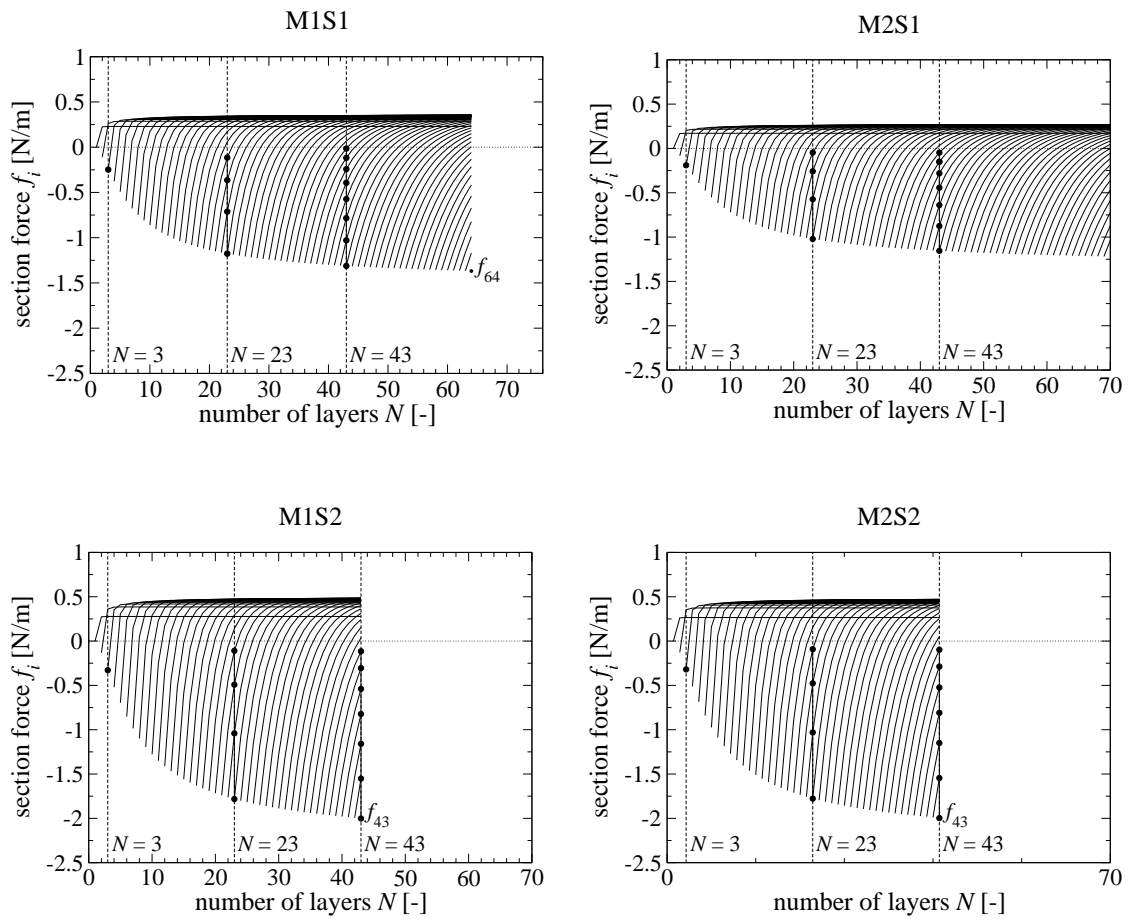
Figure 7.10: Section forces f_i in the i-th layer of an N-layered onion for all interface models. Negative values of f_i denote compression.

outer region induce the occurrence of a structural instability at a lower number of layers compared to the interface models using S1, although the number of layers under compression is the same as for M2S1, see Figure 7.11.

The results obtained with the nonlinear vdW interfaces confirm the outcome of the linear vdW model: It is most likely that the growth of carbon onions is limited by the occurrence of a structural instability. The calculated number of layers at the stability limit is already close to the number of layers observed in reality [10, 12], indicating that the nonlinear character of the vdW interactions has to be considered. However, also far larger onions can be produced [163, 185]. A larger number of layers might be reached if the assumption of the layers being icosahedral fullerenes is abandoned. Layer configurations with smaller accommodation effort might be possible in nature, explaining the large number of layers observed in [185]. Furthermore, the obtained growth limit is highly sensitive to the compressive constant and the vdW equilibrium distance used in the vdW interfaces, whereas the different exponents of vdW models M1 and M2 play only a minor role. Due to this high parameter sensitivity the results are more of a qualitative nature than of a quantitative one.

7.4 Conclusions and Outlook

Axi-symmetric shell models are used to investigate the growth of carbon onions. It is shown that the size of these particles might be limited by the occurrence of a structural instability. This instability is introduced by self-equilibrating stress states emerging due to accommodation of misfitting carbon layers during the growing process. The stresses are mainly introduced by vdW interactions between adjacent layers, whereas the influence of the curvature induced surface stress has shown to be negligible. Under the assumption that carbon onions grow from the inside to the outside, loss of stability is introduced in the outer layers whereas the innermost layers remain unaffected. Other growing scenarios might lead to different buckling patterns and should be considered in further studies. To obtain reasonable results for the growth limit the nonlinear behavior of the vdW interactions has to be taken into account. The obtained critical sizes of the onion are highly sensitive to the interlayer distance and compressive constant used in the vdW models and, thus, rather have a qualitative than a quantitative character. To obtain a better reproduction of nature also the assumption of the layers being icosahedral fullerenes should be abandoned in further studies. Nevertheless, the used models clearly indicate a growth limit of carbon onions and can serve as basis for further investigations concerning the growth of such particles.
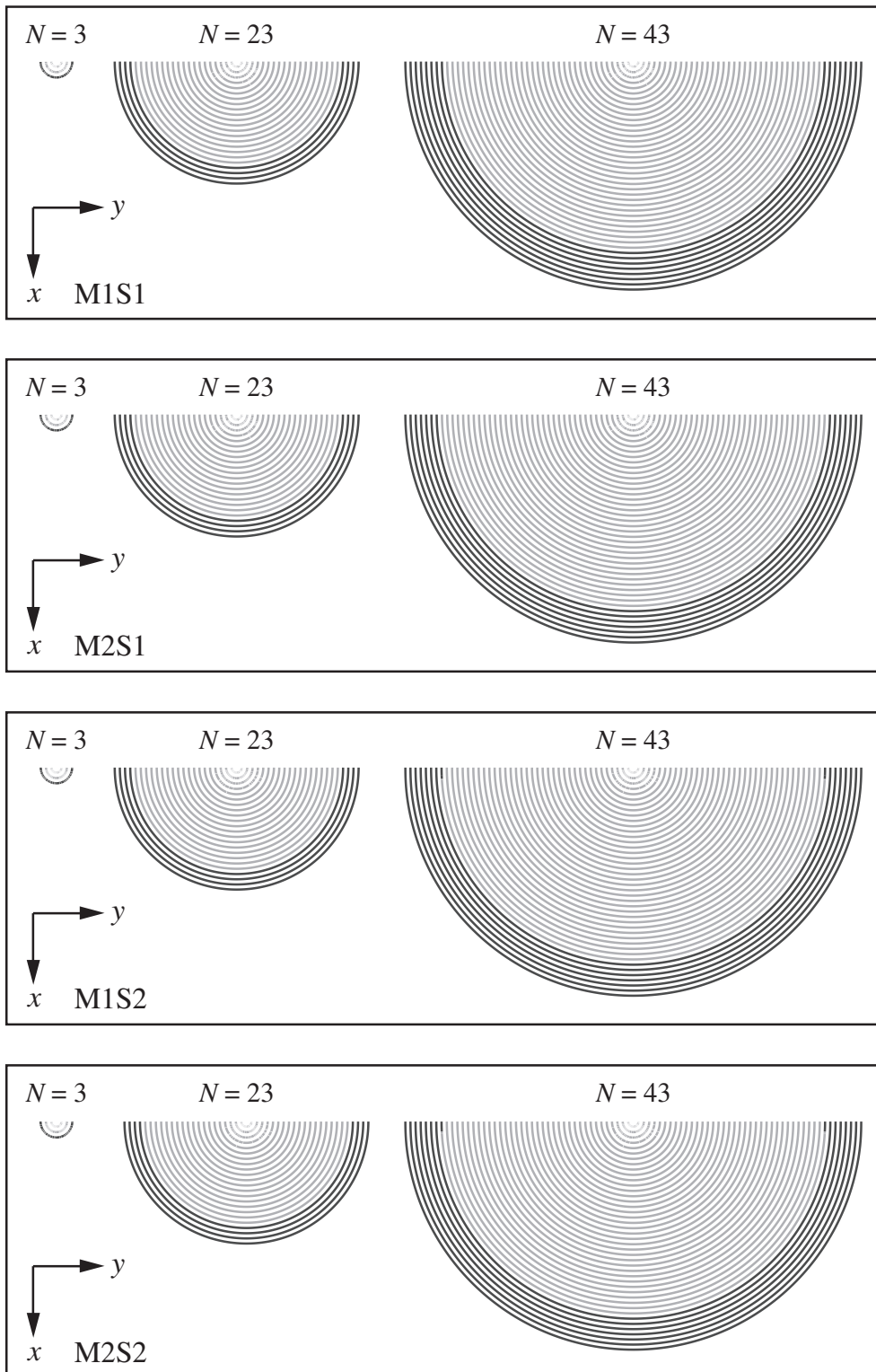
Figure 7.11: Number of layers under compression and tension for onions of different size, illustrated in black and gray, respectively.

Chapter 8

Summary

Continuum shells models were used to investigate the mechanical behavior of multi-layer carbon nanostructures such as carbon crystallites and carbon onions. The individual carbon layers were modeled as thin elastic isotropic shells, with their properties being described by three independent parameters: the elastic modulus, the layer thickness, an the Poisson's ratio. The van der Waals (vdW) interactions between adjacent layers were represented by pressure-distance relations.

Before the shell models were applied to particular multi-layer structures, different parameter sets found in literature were tested regarding their ability to predict the mechanical behavior of carbon nanostructures subjected to different loads. It was shown that the most frequently proposed parameter set with a layer thickness of $0.34\,\mathrm{nm}$ and an elastic modulus of $\sim 1\,\mathrm{TPa}$ completely fails to predict the mechanical behavior of carbon nanostructures when bending of the layers gets involved. Parameter sets with an thickness of $\sim 0.07\,\mathrm{nm}$ and an elastic modulus of $\sim 5000\,\mathrm{GPa}$ showed much better agreement with MC results and results found in literature, and hence, were used in the present thesis.

Furthermore, the influence of layer curvature on the formulation of the vdW interactions was investigated and a new pressure-distance relation for spherical carbon nanostructures was derived. It is shown that in spherical particles the vdW pressure on opposite faces is not equal and depends, besides the interlayer distance, also on the layer radii. VdW models for planar structures cannot correctly predict the vdW induced deformations of curved layers, and, consequently, also the stress state is not correctly estimated. Although the derived vdW model gives more reliable results for spherical nanostructures, it is not used further, as it cannot be implemented into standard finite element codes in a straight forward way. However, the influence of the inexact vdW model on the critical size of onions is considered to be negligible.

The first carbon nanostructures investigated were carbon crystallites which are the basic building blocks of PAN based carbon fibers. The obtained effective elastic modulus of the crystallites is in good agreement with experimentally observed

values. Hence, the used parameter set of the elastic constants predicts at least the inplane behavior of the crystallites correctly. Interlayer defects can increase the buckling load of carbon crystallites if they are randomly distributed over the whole crystallite. The elastic secant modulus is significantly reduced after the onset of buckling, explaining the shift of the neutral axis observed experimentally in bent carbon fibers. Further, it was shown that the layers buckle in an interactive way and are not separated due to buckling.

The second nanostructures considered were perfectly spherical carbon onions. It is shown that the size of the onions is limited by the occurrence of a structural instability. The stresses in the layers leading to instability are mainly introduced by the vdW interactions between the layers which emerge during the growth of the onion. The instability is introduced in the outermost layers of the onion, and, again, the layers buckle in an interactive way. The obtained critical layer numbers are close to those observed in experiments, if the nonlinear character of the vdW interactions is considered. However, they strongly depend on the values used for the parameters in the vdW models. Thus, this results rather have a qualitative than a quantitative character.

Concluding, it can be said that the membrane stiffness of carbon nanostructures can be well predicted with continuum shell models. The correctness of the results can be verified against experimental data. Although qualitatively reliable results can be achieved also for structures for which bending gets involved, the quantitative results have to be considered with more care, as the influence of the layer thickness becomes more pronounced. The values found in literature for the thickness and elastic modulus of the layers are widely scattered, even if the data set with a thickness of $0.34\,\mathrm{nm}$ and an elastic modulus of $\sim 1\,\mathrm{TPa}$ is excluded. Hence, also the bending stiffnesses and buckling loads obtained for the different sets are scattered. Further experiments and atomistic simulations on the mechanical properties of carbon nanostructures are required to reduce this scattering, and to get reliable quantitative predictions of the bending properties of carbon nanostructures.

Appendix A

Stability Analysis by Eigenvalue Prediction

According to the static stability criterion [118] (pp. 57), the stability limit of the equilibrium structure is indicated by

$$\underset{\approx}{\mathbf{K}}^* \delta \underset{\sim}{\mathbf{u}} = \underset{\sim}{\mathbf{0}} \quad \text{and} \quad \delta \underset{\sim}{\mathbf{u}} \neq \underset{\sim}{\mathbf{0}} \tag{A.1}$$

within the finite element framework. The matrix $\underset{\approx}{\mathbf{K}}^* = \underset{\approx}{\mathbf{K}}(\underset{\sim}{\mathbf{F}}_{\text{crit}})$ is the tangential stiffness matrix $\underset{\approx}{\mathbf{K}}$ at the critical loading state $\underset{\sim}{\mathbf{F}}_{\text{crit}}$ and $\delta \underset{\sim}{\mathbf{u}}$ is an infinitesimal small displacement field. The criterion states that at $\underset{\sim}{\mathbf{F}}_{\text{crit}}$ the structure can take further equilibrium states described by $\delta \underset{\sim}{\mathbf{u}}$ which are in infinitesimally close vicinity to the current equilibrium state, and do not require any change in the loading state. Calculating the critical loading state $\underset{\sim}{\mathbf{F}}_{\text{crit}}$ leads to an eigenvalue problem in which $\delta \underset{\sim}{\mathbf{u}}$ is the corresponding eigenvector representing the buckling mode of the structure.

In ABAQUS this eigenvalue problem is formulated as

$$(\underset{\approx}{\mathbf{K}} + \lambda_i \underset{\approx}{\mathbf{K}}_\Delta) \delta \underset{\sim}{\mathbf{u}}_i = \underset{\sim}{\mathbf{0}} \quad \text{with} \quad \underset{\approx}{\mathbf{K}}^* = \underset{\approx}{\mathbf{K}} + \lambda_i \underset{\approx}{\mathbf{K}}_\Delta \tag{A.2}$$

with $\underset{\approx}{\mathbf{K}}$ being the stiffness matrix of structure at the current loading state $\underset{\sim}{\mathbf{F}}$ and $\underset{\approx}{\mathbf{K}}_\Delta$ as the incremental stiffness matrix due to an additionally applied loading pattern $\underset{\sim}{\mathbf{F}}_{\text{B}}$. The quantities λ_i and $\delta \underset{\sim}{\mathbf{u}}_i$ denote the eigenvalues and corresponding eigenvectors, where $i = 1, 2, ...$ and $\lambda_1 \leq \lambda_2 \leq \lambda_3 \leq ....$ The eigenvalues λ_i are estimates of the values by which $\underset{\sim}{\mathbf{F}}_{\text{B}}$ has to be multiplied to bring the pre-loaded structure to its stability limit. For estimating the critical loading state only, the lowest eigenvalue λ_1 is of interest leading to

$$\underset{\sim}{\mathbf{F}}_{\text{crit}} \approx \underset{\sim}{\mathbf{F}} + \lambda \underset{\sim}{\mathbf{F}}_{\text{B}} . \tag{A.3}$$

Since in general $\underset{\approx}{\mathbf{K}}_\Delta(\underset{\sim}{\mathbf{F}}_{\text{B}})$ is a nonlinear relation the term $\lambda_1 \underset{\approx}{\mathbf{K}}_\Delta(\underset{\sim}{\mathbf{F}}_{\text{B}})$ is just a linear estimate of $\underset{\approx}{\mathbf{K}}_\Delta(\lambda_1 \underset{\sim}{\mathbf{F}}_{\text{B}})$. Therefore, λ_1 gets more accurate the closer the pre-loaded

state is to the critical state, meaning that $\mathbf{F}_{\mathrm{crit}}$ becomes exact for $\lambda_1 \to 0$, what can be achieved in an incremental analysis.

The loading patterns $\mathbf{F}$ and $\mathbf{F}_{\mathrm{B}}$ may consist of concentrated nodal forces, prescribed non-zero displacements, thermal loading, and distributed loads. In many practical applications the pre-buckling state does not influence the critical load (e.g., buckling of slender beams and thin plates) and the unloaded configuration represented by $\mathbf{K}(\mathbf{F} = \mathbf{0})$ is used as the current configuration of the structure, leading to $\mathbf{F}_{\mathrm{crit}} = \lambda \mathbf{F}_{\mathrm{B}}$.

Bibliography

[1] J. Aihara, S. Oe, M. Yoshida, and E. Osawa. Further test of the isolated pentagon rule: Thermodynamic and kinetic stabilities of C84 fullerene isomers. *Journal of Computational Chemistry*, 17:1387–1394, 1996.

[2] J.M. Alford and M.D. Diener. Polynuclear aromatic hydrocarbons for fullerene synthesis in flames. *U.S. Patent Application*, 20030049195, 2003.

[3] A.E. Aliev, J. Oh, M.E. Kozlov, A.A. Kuznetsov, S. Fan, and A.F. Fonseca et al. Giant-stroke, superelastic carbon nanotube aerogel muscles. *Science*, 323:1575–1578, 2009.

[4] S.R. Allen. Tensile recoil measurement of compressive strength for polymeric high performance fibres. *Journal of Materials Science*, 22:853–859, 1987.

[5] N.L. Allinger, Y.H. Yuh, and J.H. Lii. Molecular mechanics. The MM3 force field for hydrocarbons. *Journal of the American Chemical Society*, 111:8551–8566, 1989.

[6] R. Ansari and H. Rouhi. Analytical treatment of the free vibration of single-walled carbon nanotubes based on the nonlocal flugge shell theory. *Journal of Engineering Materials and Technology*, 134:011008, 2012.

[7] B. Arash and Q. Wang. A review on the application of nonlocal elastic models in modeling of carbon nanotubes and graphenes. *Computational Materials Science*, 51:303–313, 2012.

[8] S. Arghavan and A.V. Singh. Atomic lattice structure and continuum plate theories for the vibrational characteristics of graphenes. *Journal of Applied Physics*, 110:084308, 2011.

[9] K.R. Atkinson, S.C. Hawkins, C. Huynh, C. Skourtis, J. Dai, and M. Zahng et al. Multifunctional carbon nanotube yarns and transparent sheets: Fabrication, properties, and applications. *Physica B*, 394:339–343, 2007.

[10] F. Banhart. The transformation of graphitic onions to diamond under electron irradiation. *Journal of Applied Physics*, 81:3440–3445, 1997.

[11] F. Banhart and P.M. Ajayan. Carbon onions as nanoscopic pressure cells for diamond formation. *Nature*, 382:433–435, 1996.

[12] F. Banhart, T. Füller, Ph. Redlich, and P.M. Ajayan. The formation, annealing and self-compression of carbon onions under electron irradiation. *Chemical Physics Letters*, 269:349–355, 1997.

[13] D. Baowan, N. Thamwattana, and J.M. Hill. Continuum modelling of spherical and spheroidal carbon onions. *European Physical Journal D*, 44:117–123, 2007.

[14] W.E. Barth and R.G. Lawton. The synthesis of corannulene. *Journal of the American Chemical Society*, 93:1730–1745, 1971.

[15] R.C. Batra and A. Sears. Continuum models of multi-walled carbon nanotubes. *International Journal of Solids and Structures*, 44:7577–7596, 2007.

[16] R.H. Baughman, A.A Zakhidov, and W.A. de Heer. Carbon nanotubes – the route toward applications. *Science*, 297:787–792, 2002.

[17] C. Berger, Z. Song, T. Li, X. Li, A.Y. Ogbazghi, and R. Feng et al. Ultrathin epitaxial graphite: 2D electron gas properties and a route toward graphene-based nanoelectronics. *The Journal of Physical Chemistry B*, 108:19912–19916, 2004.

[18] S. Bhowmick and U.V. Waghmare. Anisotropy of the Stone-Wales defect and warping of graphene nanoribbons: A first-principles analysis. *Physical Review B*, 81:155416, 2010.

[19] V.D. Blank, V.N. Denisov, A.N. Kirichenko, B.A. Kulnitskiy, S. Yu Martushov, and B.N. Mavrin et al. High pressure transformation of single-crystal graphite to form molecular carbon onions. *Nanotechnology*, 18:345601, 2007.

[20] F.P. Bundy, H.T. Hall, H.M. Strong, and H.R. Wentorf. Man-made diamonds. *Nature*, 176:51–55, 1955.

[21] E.M. Byrne, A. Letertre, M.A. McCarthy, W.A. Curtin, and Z. Xia. Optimizing load transfer in multiwall nanotubes through interwall coupling: Theory and simulation. *Acta Materialia*, 58:6324–6333, 2010.

[22] E. Cadelano, S. Giordano, and L. Colombo. Interplay between bending and stretching in carbon nanoribbons. *Physical Review B*, 81:144105, 2010.

[23] E. Cadelano, P.L. Palla, S. Giordano, and L. Colombo. Nonlinear elasticity of monolayer graphene. *Physical Review Letters*, 102:235502, 2009.

[24] A.G. Cano-Márquez, F.J. Rodiguez-Macías, J. Campos-Delgado, C.G. Espinosa-González, F. Tristán-López, and D. Ramirez-González et al. Ex-MWNTs: Graphene sheets and ribbons produced by lithium intercalation and exfoliation of carbon nanotubes. *Nano Letters*, 9:1527–1533, 2009.

[25] F. Cataldo. The impact of a fullerene-like concept in carbon black science. *Carbon*, 40:157–162, 2011.

[26] T. Chang. A molecular based anisotropic shell model for single-walled carbon nanotubes. *Journal of the Mechanics and Physics of Solids*, 58:1422–1433, 2010.

[27] J.C. Charlier and J.P. Michenaud. First-principles study of the electronic properties of simple hexagonal graphite. *Physical Review B*, 46:4531–4540, 1992.

[28] S. Chen and D.C. Chrzan. Monte Carlo simulation of temperature-dependent elastic properties of graphene. *Physical Review B*, 84:195409, 2011.

[29] S. Chen, E. Ertekin, and D.C. Chrzan. Plasticity in carbon nanotubes: Cooperative conservative dislocation motion. *Physical Review B*, 81:155417, 2010.

[30] L.P.F. Chibante, A. Thess, J.M. Alford, M.D. Diener, and R.E. Smalley. Solar generation of the fullerenes. *Journal of Physical Chemistry*, 97:8696–8700, 1993.

[31] W. Choi and J.W. Lee, editors. *Graphene Synthesis and Applications*. CRC Press, New York, 2012.

[32] A. Chuvilin, U. Kaiser, E. Bichoutskaia, N.A. Besley, and A.N. Khlobystov. Direct transformation of graphene to fullerene. *Nature Chemistry*, 2:450–453, 2010.

[33] O.C. Compton and S.T. Nguyen. Graphene oxide, highly reduced graphene oxide, and graphene: Versatile building blocks for carbon-based materials. *Small*, 6:711–723, 2010.

[34] P.L. deAndres, R. Ramirez, and J.A. Vergés. Strong covalent bonding between two graphene layers. *Physical Review B*, 77:045403, 2008.

[35] S.J. Deteresa, S.R. Allen, R.J. Farris, and R.S. Porter. Compressive and torsional behaviour of Kevlar 49 fibre. *Journal of Materials Science*, 19:57–72, 1984.

[36] F. Diederich, R. Ettl, Y. Rubin, R.L. Whetten, R. Beck, and M. Alvarez et al. The higher fullerenes: Isolation and characterization of C76, C84, C90, C94, and C70O, an oxide of D5h-C70. *Science*, 252:548–551, 1991.

[37] M. Dion, H. Rydberg, E. Schröder, D.C. Langreth, and B.I. Lundqvist. Van der Waals density functional for general geometries. *Physical Review Letters*, 92:246401, 2004.

[38] M.G. Dobb, H. Guo, D.J. Johnson, and C.R. Park. Structure-compressional property relations in carbon fibres. *Carbon*, 33:1553–1559, 1995.

[39] M. Drmota, R. Scheidl, H. Troger, and E. Weinmüller. On the imperfection sensitivity of complete spherical shells. *Computational Mechanics*, 2:63–74, 1987.

[40] A.-B. Du, X.-G. Liu, D.-J. Fu, P.-D. Han, and B.-S. Xu. Onion-like fullerenes synthesis from coal. *Fuel*, 86:294–298, 2007.

[41] H. Dumlich and S. Reich. Nanotube bundles and tube-tube orientation: A van der Waals density functional study. *Physical Review B*, 84:064121, 2011.

[42] R. Ettl, I. Chao, and F. Diederich R.L. Whetten. Isolation of C76, a chiral (D2) allotrope of carbon. *Nature*, 353:149–152, 1991.

[43] F.D. Fischer, T. Waitz, D. Vollath, and N.K. Simha. On the role of surface energy and surface stress in phase-transforming nanoparticles. *Progress in Materials Science*, 53:481–527, 2008.

[44] P.W. Fowler, R.C. Batten, and D.E. Manolopoulos. The higher fullerences: a candidate for the structure of C78. *Journal of the Chemical Society: Faraday Transactions*, 87:3103–3104, 1991.

[45] D. Fu, X. Liu, X. Lin, T. Li, H. Jia, and B. Xu. Synthesis of encapsulating and hollow onion-like fullerenes from coal. *Journal of Material Science*, 42:3805–3809, 2007.

[46] T. Füller and F. Banhart. In situ observation of the formation and stability of single fullerene molecules under electron irradiation. *Chemical Physics Letters*, 254:372–378, 1996.

[47] A.K. Geim. Graphene: Status and prospects. *Science*, 324:1530–1534, 2009.

[48] A.K. Geim and K.S. Novoselov. The rise of graphene. *Nature Materials*, 6:183–191, 2007.

[49] S.K. Georgantzinos, D.E. Katsareas, and N.K. Anifantis. Limit load analysis of graphene with pinhole defects: A nonlinear structural mechanics approach. *International Journal of Mechanical Sciences*, 55:85–94, 2012.

[50] Ph. Gerhardt, S. Löffler, and K.H. Homann. Polyhedral carbon ions in hydrocarbon flames. *Chemical Physics Letters*, 137:306–310, 1987.

[51] S. Grimme. Accurate description of van der Waals complexes by density functional theory including emprical conditions. *Computational Chemistry*, 25:1463–1473, 2004.

[52] P.R. Guduru and Z. Xia. Shell buckling of imperfect multiwalled carbon nanotubes – experiments and analysis. *Experimental Mechanics*, 47:153–161, 2007.

[53] W. Guo, C.Z. Zhu, T.X. Yu, C.H. Woo, B. Zhang, and Y.T. Dai. Formation of sp^3 bonding in nanoindented carbon nanotubes and graphite. *Physical Review Letters*, 93:245502, 2004.

[54] S.E. Haggerty. Diamond genesis in a multiply-constrained model. *Nature*, 320:34–38, 1986.

[55] H.C. Hamaker. The London–van der Waals attraction between spherical particles. *Physica IV*, 10:1058–1072, 1937.

[56] M.A. Hartmann. Private communications. 2012.

[57] R.E. Haufler, J. Conceicao, L.P.F. Chibante, Y. Chai, N.E. Byrne, and S. Flanagan et al. Efficient production of C60 (buckminsterfullerene), C60H36, and the solvated buckide ion. *Journal of Physical Chemistry*, 94:8634–8636, 1990.

[58] H.M. Hawthorne. On non-Hookean behavior of carbon fibers in bending. *Journal of Material Science*, 28:2531–2535, 1993.

[59] H.M. Hawthorne and E. Teghtsoonian. Axial compression fracture in carbon fibres. *Journal of Material Science*, 10:41–51, 1975.

[60] X.Q. He, S. Kitipornchai, and K.M. Liew. Buckling analysis of multi-walled carbon nanotubes: a continuum model accounting for van der Waals interaction. *Journal of the Mechanics and Physics of Solids*, 53:303–326, 2005.

[61] A. Hirata, M. Igarashi, and T. Kaito. Study on solid lubricant properties of carbon onions produced by heat treatment of diamond clusters or particles. *Tribology International*, 37:899–905, 2004.

[62] A. Hirsch and M. Brettreich. *Fullerenes*. Wiley-VCH Verlag, Weinheim, 2005.

[63] D. Holec, M.A. Hartmann, F.D. Fischer, F.G. Rammerstorfer, P.H. Mayrhofer, and O. Paris. Curvature-induced excess surface energy of fullerenes: Density functional theory and Monte Carlo simulations. *Physical Review B*, 81:235403, 2010.

[64] J.B. Howard, J.T. McKinnon, Y. Makarovsky, A.L. Lafleur, and M.E. Johnson. Fullerenes C60 and C70 in flames. *Nature*, 352:139–141, 1991.

[65] X. Huang, H. Yuan, W. Liang, and S. Zhang. Mechanical properties and deformation morphologies of covalently bridged multi-walled carbon nanotubes: Multiscale modeling. *Journal of the Mechanics and Physics of Solids*, 58:1847–1862, 2010.

[66] Y. Huang, J. Wu, and K.C. Hwang. Thickness of graphene and single-wall carbon nanotubes. *Physical Review B*, 74:245413, 2006.

[67] S. Iglesias-Groth, J. Breton, and C. Girardet. An analytical approach for the interlayer interaction in spherical buckyonions. *Chemical Physics Letters*, 264:351–358, 1997.

[68] S. Iijima. Direct observation of the tetrahedral bonding in graphitized carbon black by high resolution electron microscopy. *Journal of Crystal Growth*, 50:675–683, 1980.

[69] S. Iijima. Helical microtubules of graphitic carbon. *Nature*, 354:56–58, 1991.

[70] L. Joly-Pottuz, N. Matsumoto, H. Kinoshita, B. Vacher, M. Belin, and G. Montagnac et al. Diamond-derived carbon onions as lubricant additives. *Tribology International*, 41:69–78, 2008.

[71] Z.Y. Juang, C.Y. Wu, C.W. Lo, W.Y Chen, C.F. Huang, and J.C. Hwang et al. Synthesis of graphene on silicon carbide substrates at low temperature. *Carbon*, 47:2026 – 2031, 2009.

[72] B. Kelly. *Physics of Graphite*, pages 79–80. Advanced Science Publishers, 1981.

[73] K. Kikuchi, N. Nakahara, M. Honda, S. Suzuki, K. Saito, and H. Shiromaru et al. Separation, detection, and UV/visible absorption spectra of fullerenes; C76, C78, and C84. *Chemistry Letters*, 20:1607–1610, 1991.

[74] A. Kis, C. Csányi, J.-P. Salvetat, T.N. Lee, E. Couteau, A.J. Kulik, W. Benoit, J. Brugger, and L. Forró. Reinforcement of single-walled carbon nanotube bundles by intertube bridging. *Nature Materials*, 3:153–157, 2004.

[75] D.J. Klein, W.A. Seitz, and T.G. Schmalz. Icosahedral symmetry carbon cage molecules. *Nature*, 323:703–706, 1986.

[76] W. Krätschmer, L.D. Lamb, K. Fostiropoulos, and D.R. Huffman. Solid C60: a new form of carbon. *Nature*, 347:354–358, 1990.

[77] H.W. Kroto. The stability of the fullerenes C_n, with $n = 24, 28, 32, 36, 50, 60,$ and 70. *Nature*, 329:529–531, 1987.

[78] H.W. Kroto. Carbon onions introduce new flavour to fullerene studies. *Nature*, 359:670–671, 1992.

[79] H.W. Kroto, J.R. Heath, S.C. O'Brien, R.F. Curl, and R.E. Smalley. C60: Buckminsterfullerene. *Nature*, 318:162–163, 1985.

[80] H.W. Kroto and K. McKay. The formation of quasi-icosahedral spiral shell carbon particles. *Nature*, 331:328–331, 1988.

[81] V.L. Kuznetsov, A.L. Chuvilin, Y.V. Butenko, I.Y. Malkov, and V.M. Titov. Onion-like carbon from ultra-disperse diamond. *Chem Phys Lett*, 222:343–348, 1994.

[82] C.N. Lau, W. Bao, and J. Velasco Jr. Properties of suspended graphene membranes. *Materials Today*, 15:238–245, 2012.

[83] C. Lee, X. Wei, J.W. Kysar, and J. Hone. Measurement of the elastic properties and intrinsic strength of monolayer graphene. *Science*, 321:385–388, 2008.

[84] S.T. Lee and Y. Lifshitz. The road to diamond wafers. *Nature*, 424:500–501, 2003.

[85] C. Li and T.W. Chou. Elastic moduli of multi-walled carbon nanotubes and the effect of van der Waals forces. *Composite Science and Technology*, 63:1517–1524, 2003.

[86] C. Li and T.W. Chou. A structural mechanics approach for the analysis of carbon nanotubes. *International Journal of Solids and Structures*, 40:2487–2499, 2003.

[87] G. Van Lier, C. Van Alsenoy, V. Van Doren, and P. Geerlings. *Ab initio* study of the elastic properties of single-walled carbon nanotubes and graphene. *Chemical Physics Letters*, 326:181–185, 2000.

[88] K.M. Liew and Y.Z. Sun. Computational modelling and simulation of carbon nanotubes. In B.H.V Topping, J.M. Adam, F.J. Pallarés, R. Bru, and

M.L. Romeo, editors, *Development and Applications in Engineering Computational Technology*, pages 201–217. Saxe-Coburg Publications, Stirlingshire, Scotland, 2010.

[89] F. Liu, P. Ming, and J. Li. *Ab initio* calculation of ideal strength and phonon instability of graphene under tension. *Physical Review B*, 76:064120, 2007.

[90] W.K. Liu, E.G. Karpov, S. Zhang, and H.S. Park. An introduction to computational nanomechanics and materials. *Computer Methods in Applied Mechanics and Engineering*, 193:1529–1578, 2004.

[91] D. Loidl, O. Paris, M. Burghammer, C. Riekel, and H. Peterlik. Direct observation of nanocrystallite buckling in carbon fibers under bending load. *Physical Review Letters*, 95:225501, 2005.

[92] D. Loidl, H. Peterlik, M. Müller, Ch. Riekel, and O. Paris. Elastic moduli of nanocrystallites in carbon fibers measured by in-situ X-ray microbeam diffraction. *Carbon*, 41:563–570, 2003.

[93] F. London. Zur Theorie und Systematik der Molekularkräfte. *Zeitschrift für Physik*, 63:245–279, 1930.

[94] J.H. Los, N. Pineau, G. Chevrot, G. Vignoles, and J.M. Leyssale. Formation of multiwall fullerenes from nanodiamonds studied by atomistic simulations. *Physical Review B*, 80:155420, 2009.

[95] O. Lourie, D.M. Cox, and H.D. Wagner. Buckling and collapse of embedded carbon nanotubes. *Physical Review Letters*, 81:1638–1641, 1998.

[96] Q. Lu, M. Arroyo, and R. Huang. Elastic bending modulus of monolayer graphene. *Journal of Physics D*, 42:102002, 2009.

[97] Q. Lu and R. Huang. Nonlinear mechanics of single-atomic-layer graphene sheets. *International Journal of Applied Mechanics*, 1:443–467, 2009.

[98] W.B. Lu, B. Liu, J. Wu, J. Xiao, K.C. Hwang, and S.Y. Fu et al. Continuum modeling of van der Waals interactions between carbon nanotube walls. *Applied Physics Letters*, 94:101917, 2009.

[99] J. Macutkevic, D. Seliuta, G. Valusis, J. Banys, P. Kuzhir, and S. Maksimenko et al. Dielectric properties of onion-like carbon based polymer films: Experiment and modeling. *Solid State Sciences*, 11:1828–1832, 2009.

[100] A. Mashreghi and M.M. Moshksar. Bond lengths and bond angles of armchair single-walled carbon nanotubes through molecular dynamics and potential energy curve approaches. *Computational Materials Science*, 49:871–875, 2010.

[101] A. Mashreghi and M.M. Moshksar. Investigating the effect of chirality on structural parameters of chiral single-walled carbon nanotubes by molecular dynamics simulation. *Computational Materials Science*, 50:934–938, 2011.

[102] M. Meo and M. Rossi. Prediction of Young's modulus of single wall carbon nanotubes by molecular-mechanics based finite element modelling. *Composites Science and Technology*, 66:1597–1605, 2006.

[103] J.C. Meyer, A.K. Geim, M.I. Katsnelson, K.S. Novoselov, T.J. Booth, and S. Roth. The structure and properties of suspended graphene sheets. *Nature*, 446:60–63, 2007.

[104] J.C. Meyer, C. Kisielowski, R. Erni, M.D. Rossell, M.F. Crommie, and A. Zettl. Direct imaging of lattice atoms and topological defects in graphene membranes. *Nano Letters*, 8:3582–3586, 2008.

[105] G. Mie. Zur kinetischen Theorie der einatomigen Körper. *Annalen der Physik*, 11:657–697, 1903.

[106] A. Montazeri, M. Sadeghi, R. Naghdabadi, and H. Rafii-Tabar. Computational modeling of the transverse-isotropic elastic properties of single-walled carbon nanotubes. *Computational Materials Science*, 49:544–551, 2010.

[107] C.E. Mortimer. *Chemie*. Georg Thieme Verlag KG, Stuttgart, 2010.

[108] A. Muc. Design and identification methods of effective mechanical properties for carbon nanotubes. *Materials and Design*, 31:1671–1675, 2010.

[109] K. Naito, Y. Tanaka, J.M. Yang, and Y. Kagawa. Tensile properties of ultrahigh strength PAN-based, ultrahigh modulus pitch-based and high ductility pitch-based carbon fibers. *Carbon*, 46:189–195, 2008.

[110] M. Nakatani, M. Shioya, and J. Yamashita. Axial compressive fracture of carbon fibers. *Carbon*, 37:601–608, 1999.

[111] K.S. Novoselov, A.K. Geim, S.V. Morozov, D. Jiang, Y. Zhang, and S.V. Dubonos et al. Electric field effect in atomically thin carbon films. *Science*, 306:666–669, 2004.

[112] N. Oya and D.J. Johnson. Direct measurement of longitudinal compressive strength in carbon fibres. *Carbon*, 37:1539–1544, 1999.

[113] N. Oya and D.J. Johnson. Longitudinal compressive behaviour and microstructure of PAN-based carbon fibres. *Carbon*, 39:635–645, 2001.

[114] A. Pantano, D.M. Parks, and M.C. Boyce. Mechanics of deformation of single- and multi-wall carbon nanotubes. *Journal of the Mechanics and Physics of Solids*, 52:789–821, 2004.

[115] O. Paris and H. Peterlik. The structure of carbon fibres. In S. Eichhorn, J.W.S Hearle, M. Jaffe, and T. Kikutani, editors, *Handbook of textile fibre structure*, volume 2. Woodhead Publishing Limited, Cambridge, UK, 2009.

[116] B. Peng, Y. Li, S. Liu, Z. Guo, and L. Ding. The roles of crosslinks in the buckling behaviors and load transferring mechanisms of double-walled nanotubes under compression. *Computational Materials Science*, 55:95–99, 2012.

[117] G. Peters and M. Jansen. A new fullerene synthesis. *Angewandte Chemie International Edition*, 31:223–224, 1992.

[118] A. Pflüger. *Stabilitätsprobleme der Elastostatik*. Springer-Verlag, Berlin, 1975.

[119] M. Pozzo, D. Alfè, P. Lacovig, P. Hofmann, S. Lizzit, and A. Baraldi. Thermal expansion of supported and freestanding graphene: Lattice constant versus interatomic distance. *Physical Review Letters*, 106:135501, 2011.

[120] H. Rafii-Tabar. *Computational physics of carbon nanotubes*. Cambridge University Press, Cambridge, 2008.

[121] P. Redlich, F. Banhart, Y. Lyutovich, and P.M. Ajayan. EELS study of the irradiation-induced compression of carbon onions and their transformation to diamond. *Carbon*, 36:561–563, 1998.

[122] C.Q. Ru. Effect of van der Waals forces on axial buckling of a double-walled carbon nanotube. *Journal of Applied Physics*, 87:7227–7231, 2000.

[123] A. Sakhaee-Pour. Elastic buckling of single-layered graphene sheet. *Computational Material Science*, 45:266–270, 2009.

[124] A. Sakhaee-Pour. Elastic properties of single-layered graphene sheet. *Solid State Communications*, 149:91–95, 2009.

[125] A. Sakhaee-Pour, M.T. Ahmadian, and A. Vafai. Applications of single-layered graphene sheets as mass sensors and atomistic dust detectors. *Solid State Communications*, 145:168–172, 2008.

[126] A. Sakhaee-Pour, M.T. Ahmadian, and A. Vafai. Potential application of single-layered graphene sheet as strain sensor. *Solid State Communications*, 147:336–340, 2008.

[127] M. Sato, M.A. Wadee, K. Iiboshi, T. Sekizawa, and H. Shima. Buckling patterns of complete spherical shells filled with an elastic medium under external pressure. *International Journal of Mechanical Sciences*, 59:22–30, 2012.

[128] C. Sauder and J. Lamon. Prediction of elastic properties of carbon fibers and CVI matrices. *Carbon*, 43:2044–2053, 2005.

[129] C. Sauder, J. Lamon, and R. Pailler. The tensile behavior of carbon fibers at high temperatures up to 2400°C. *Carbon*, 42:715–725, 2004.

[130] A. Sears and R.C. Batra. Macroscopic properties of carbon nanotubes from molecular-mechanics simulations. *Physical Review B*, 69:235406, 2004.

[131] H.S. Shen and C.L. Zhang. Postbuckling of double-walled carbon nanotubes with temperature dependent properties and initial defects under combined axial and radial mechanical loads. *International Journal of Solids and Structures*, 44:1461–1487, 2007.

[132] H. Shima, S. Ghosh, M. Arroyo, K. Iiboshi, and M. Sato. Thin-shell theory based analysis of radially pressurized multiwall carbon nanotubes. *Computational Materials Science*, 52:90–94, 2012.

[133] D. Sinclair. A bending method for measurement of the tensile strength and Young's modulus of glass fiber. *Journal of Applied Physics*, 21:380–386, 1950.

[134] V. Singh, D. Joung, L. Zhai, S. Das, S.I. Khondaker, and S. Seal. Graphene based materials: Past, present and future. *Progress in Materials Science*, 56:1178–1271, 2011.

[135] P.R. Somani, S.P. Somani, and M. Umeno. Planer nano-graphenes from camphor by CVD. *Chemical Physics Letters*, 430:56–59, 2006.

[136] S. Stankovich, D.A. Dikin, G.H.B. Dommett, K.M. Kohlhaas, E.J. Zimney, and E.A. Stach et al. Graphene-based composite materials. *Nature*, 442:282–286, 2006.

[137] S. Stankovich, D.A. Dikin, R.D. Piner, K.A. Kohlhaas, A. Kleinhammes, and Y. Jia et al. Synthesis of graphene-based nanosheets via chemical reduction of exfoliated graphite oxide. *Carbon*, 45:1558–1565, 2007.

[138] C. Sun and K. Liu. Combined torsional buckling of multi-walled carbon nanotubes coupling with axial loading and radial pressures. *International Journal of Solids and Structures*, 45:2128–2139, 2008.

[139] A.C. Tang and F.Q. Huang. Stability rules of icosahedral (Ih or I) fullerenes. *Chemical Physics Letters*, 247:494–501, 1995.

[140] A.C. Tang and F.Q. Huang. Theoretical study of multishell fullerenes. *Physical Review B*, 52:17435–17438, 1995.

[141] A. Tapia, R. Peón-Escalante, C. Villanueva, and F. Avilés. Influence of vacancies on the elastic properties of a graphene sheet. *Computational Materials Science*, 55:255–262, 2012.

[142] R. Taylor, J. Langley, H.W. Kroto, and D.R.M. Walton. Formation of C60 by pyrolysis of naphthalene. *Nature*, 366:728–731, 1993.

[143] R.H. Telling, C.P. Ewels, A.A. El-Barbary, and M.I. Heggie. Wigner defects bridge the graphite gap. *Nature Materials*, 2:333–337, 2003.

[144] H. Terrones and M. Terrones. The transformation of polyhedral particles into graphitic onions. *Journal of the Physics and Chemistry of Solids*, 58:1789–1796, 1997.

[145] M. Todt, F.G. Rammerstorfer, F.D. Fischer, P.H. Mayrhofer, D. Holec, and M.A. Hartmann. Continuum modeling of van der Waals interactions between carbon onion layers. *Carbon*, 49:1620–1627, 2011.

[146] M. Todt, F.G. Rammerstorfer, M.A. Hartmann, O. Paris, and F.D. Fischer. Shell-models for multi-layer carbon nano-particles. In H. Altenbach and V.A. Eremeyev, editors, *Advanced Structured Materials: Shell-like Structures*, pages 585–602. Springer-Verlag, Berlin, 2011.

[147] M. Todt, F.G. Rammerstorfer, O. Paris, and F.D. Fischer. Nanomechanical studies of the compressive behavior of carbon fibers. *Journal of Material Science*, 45:6845–6848, 2010.

[148] S. Tomita, A. Burian, J.C. Dore, D. LeBolloch, M. Fujii, and S. Hayashi. Diamond nanoparticles to carbon onions transformation: X-ray diffraction studies. *Carbon*, 40:1469–1474, 2002.

[149] M.M.J. Treacy, T.W. Ebbesen, and J.M. Gibson. Exceptionally high Young's modulus observed for individual carbon nanotubes. *Nature*, 381:678–680, 1996.

[150] K.I. Tserpes and P. Papanikos. Finite element modeling of single-walled carbon nanotubes. *Composites: Part B*, 36:468–477, 2005.

[151] D. Ugarte. Curling and closure of graphitic networks under electron-beam irradiation. *Nature*, 359:707–709, 1992.

[152] D. Ugarte. Morphology and structure of graphitic soot particles generated in arc-discharge C60 production. *Chemical Physics Letters*, 198:596–602, 1992.

[153] D. Ugarte. Formation mechanism of quasi-spherical carbon particles induced by electron bombardment. *Chemical Physics Letters*, 207:473–479, 1993.

[154] D. Ugarte. Onion-like graphitic particles. *Carbon*, 33:989–993, 1995.

[155] L.M. Viculis, J.J. Mack, and R.B. Kaner. A chemical route to carbon nano-scrolls. *Science*, 299:1361, 2003.

[156] D. Vollath. *Nanomaterials*. Wiley-VCH, Weinheim, 2008.

[157] Y.L. Voytekhovsky. A formula to estimate the size of a fullerene. *Acta Crystallographica A*, 59:193–194, 2003.

[158] J.H. Walther, R. Jaffe, T. Halicioglu, and P. Koumoutsakos. Carbon nanotubes in water: Structural characteristics and energetics. *Journal of Physical Chemistry B*, 105:9980–9987, 2001.

[159] B.C. Wang, H.W. Wang, J.C. Chang, H.C. Tso, and Y.M. Chou. More spherical large fullerenes and multi-layer fullerene cages. *Journal of Molecular Structure*, 540:171–176, 2001.

[160] C.M. Wang, Y.Y. Zhang, Y. Xiang, and J.N. Reddy. Recent studies on buckling of carbon nanotubes. *Applied Mechanics Reviews*, 63:030804, 2010.

[161] C.Y. Wang, C.Q. Ru, and A. Mioduchowski. Axially compressed buckling of pressured multiwall carbon nanotubes. *International Journal of Solids and Structures*, 40:3893–3911, 2003.

[162] X. Wang, H.K. Yang, and K. Dong. Torsional buckling of multi-walled carbon nanotubes. *Materials Science and Engineering A*, 404:314–322, 2005.

[163] P. Wesolowski, Y. Lyutovich, F. Banhart, H.D. Carstanjen, and H. Kronmüller. Formation of diamond in carbon onions under MeV ion irradiation. *Applied Physics Letters*, 71:1948–1950, 1997.

[164] J. Wu, K.C. Hwang, and Y. Huang. An atomistic-based finite-deformation shell theory for single-wall carbon nanotubes. *Journal of the Mechanics and Physics of Solids*, 56:279–292, 2008.

[165] J. Wu, J. Peng, K.C. Hwang, J. Song, and Y. Huang. The intrinsic stiffness of single-wall carbon nanotubes. *Mechanics Research Communications*, 35:2–9, 2008.

[166] Z. Xin, Z. Jianjun, and Q.Y. Zhong-can. Strain energy and Young's modulus of single-wall carbon nanotubes calculated from electronic energy-band theory. *Physical Review B*, 62:13692–13696, 2000.

[167] M. Xu, J.T. Paci, J. Oswald, and T. Belytschko. A constitutive equation for graphene based on density functional theory. *International Journal of Solids and Structures*, 49:2582–2589, 2012.

[168] M. Xu, A. Tabarraei, J.T. Paci, J. Oswald, and T. Belytschko. A coupled quantum/continuum mechanics study of graphene fracture. *International Journal of Fracture*, 173:163–173, 2012.

[169] B.I. Yakobson, C.J. Brabec, and J. Bernholc. Nanomechanics of carbon tubes: Instabilities beyond linear response. *Physical Review Letters*, 76:2511–2514, 1996.

[170] X. Yao, Q. Han, and H. Xin. Bending buckling behaviors of single- and multi-walled carbon nanotubes. *Computationa Material Science*, 43:579–590, 2008.

[171] A. Yarnel. The many facets of manmade diamonds. *Chemical and Engineering News*, 82:26–31, 2004.

[172] Q. Yu, J. Lian, S. Siriponglert, H. Li, Y.P. Chen, and S.S. Pei. Graphene segregated on Ni surfaces and transferred to insulators. *Applied Physics Letters*, 93:113103, 2008.

[173] M. Yudasaka, T. Komatsu, T. Ichihashi, and S. Iijima. Single-wall carbon nanotube formation by laser ablation using double-targets of carbon and metal. *Chemical Physics Letters*, 278:102–106, 1997.

[174] C.L. Zhang and H.S. Shen. Buckling and postbuckling analysis of single-walled carbon nanotubes in thermal environments via molecular dynamics simulation. *Carbon*, 44:2608–2616, 2006.

[175] D.B. Zhang, E. Akatyeva, and T. Dumitrică. Bending ultrathin graphene at the margins of continuum mechanics. *Physical Review Letters*, 106:255503, 2011.

[176] H.W. Zhang, L. Wang, and J.B. Wang. Computer simulation of buckling behavior of double-walled carbon nanotubes with abnormal interlayer distances. *Computational Materials Science*, 39:664–672, 2007.

[177] P. Zhang, Y. Huang, P.H. Geubelle, P.A. Klein, and K.C. Hwang. The elastic modulus of single-wall carbon nanotubes: a continuum analysis incorporating interatomic potentials. *International Journal of Solids and Structures*, 39:3893–3906, 2002.

[178] Q.L. Zhang, S.C. O'Brien, J.R. Heath, Y. Liu, R.F. Curl, and H.W. Kroto et al. Reactivity of large carbon clusters: Spheroidal carbon shells and their possible relevance to the formation and morphology of soot. *Journal of Physical Chemistry*, 90:525–528, 1986.

[179] Y.Y. Zhang, Y. Xiang, and C.M. Wang. Buckling of defective carbon nanotubes. *Journal of Applied Physics*, 106:113503, 2009.

[180] H. Zhao and N.R. Aluru. Temperature and strain-rate dependent fracture strength of graphene. *Journal of Applied Physics*, 108:064321, 2010.

[181] J. Zhao, M. He, S. Dai, J.Q. Huang, F. Wei, and J. Zhu. TEM observations of buckling and fracture modes for compressed thick multiwall carbon nanotubes. *Carbon*, 49:206–213, 2011.

[182] M. Zhao, H. Song, X. Chen, and W. Lian. Large-scale synthesis of onion-like carbon nanoparticles by carbonization of phenolic resin. *Acta Materialia*, 55:6144–6150, 2007.

[183] Y.X. Zhao and I.L. Spain. X-ray diffraction data for graphite to 20 GPa. *Physical Review B*, 40:993–997, 1989.

[184] J. Zhou and R. Huang. Internal lattice relaxation of single-layer graphene under in-plane deformation. *Journal of the Mechanics and Physics of Solids*, 56:1609–1623, 2008.

[185] M.S. Zwanger, F. Banhart, and A. Seeger. Formation and decay of spherical concentric-shell carbon clusters. *Journal of Crystal Growth*, 163:445–454, 1996.

Curriculum Vitae: Melanie Todt

Birth:	22.10.1982 in Leoben
Address:	Canongasse 16/3, A-1180 Wien
Tel.:	+43 660 250 48 28
E-mail:	mt@ilsb.tuwien.ac.at
Nationality:	Austrian
Martial status:	not married

Education

2008 – 2012	PhD studies at the Vienna University of Technology, Institute for Lightweight Design and Structural Biomechanics.
2002 – 2008	Diploma studies in mechanical engineering at the Vienna University of Technology, with the focus on numerical methods in engineering.
1997 – 2002	HTBLuVA Mödling (technical high school), with focus on precision engineering.

Professional activities

since 2008	Scientific assistant at the Institute of Lightweight Design and Structural Biomechanics, Vienna University of Technology.
since 2010	Member of the curriculum commission of mechanical engineering at Vienna University of Technology
17.07. - 31.08. 2005	Internship SA&SA Company, Skopje, Republic of Macedonia, IAESTE Program

Further activities and awards

2011	Amelia Earhart Fellowship Award 2011/12, Zonta International Foundation.
2010	Best Poster Award PhD Category, 2010, Junior Scientist Conference.
2007 – 2008	Member of the Formula Student Team at Vienna University of Technology, Responsible for the construction of the crash box.

Journal Articles:

M. Todt, F. G. Rammerstorfer, F.D. Fischer, P.H. Mayrhofer, D. Holec, M.A. Hartmann: "Continuum Modeling of van der Waals Interactions Between Carbon Onion Layers"; Carbon, 49 (2011), 5; p. 1620 - 1627.

M. Todt, F. G. Rammerstorfer, O. Paris, F.D. Fischer: "Nanomchanical Studies of the Compressive Behavior of Carbon Fibers"; Journal of Materials Science, 45 (2010), 24; S. 6845 - 6848.

Conferences:

M.A. Hartmann, M. Todt, F. G. Rammerstorfer, D. Holec, P.H. Mayrhofer, F.D. Fischer, O. Paris: "Simualtion-Based Design of Nanocomposite Metamaterials"; Presentation: 10th World Congress on Computational Mechanics (WCCM 2012), So Paulo; 08.07.2012 - 13.07.2012.

M. Todt, M.A. Hartmann, D. Holec, F. G. Rammerstorfer: "Accessing the Mechanical Behavior of Carbon Fullerenes by Continuum Shell Models"; Presentation: 10th World Congress on Computational Mechanics (WCCM 2012), So Paulo; 08.07.2012 - 13.07.2012.

M. Todt, M.A. Hartmann, O. Paris, F.D. Fischer, F. G. Rammerstorfer: "Computational Treatment of the Stability of Multi-Layered Carbon Nanoparticles"; Presentation: 7th International Conference on Computational Mechanics of Spatial Structures (IASS-IACM 2012), Sarajevo; 02.04.2012 - 04.04.2012; in: "Proceedings of the 7th International Conference on Computational Mechanics of Spatial Structures", A. Ibrahimbegovic, S Dolarevic, M. Hrasnica, M. Madzarevic, M. Zlatar

(Hrg.); Faculty of Civil Engineering Sarajevo, (2012), ISBN: 978-9-958-63830-5; S. 307 - 309.

M.A. Hartmann, D. Holec, M. Todt, F.D. Fischer, F. G. Rammerstorfer, P.H. Mayrhofer, O. Paris: "A Multi-Scale Approach for Studying Carbon Nanostructures"; Presentation: Joint Annual Meeting of the Swiss Physical Society and the Austrian Physical Society 2011, Lausanne; 15.06.2011 - 17.06.2011.

M. Todt, F. G. Rammerstorfer, O. Paris, F.D. Fischer: "Mechanical Behavior of Carbon Crystallites Forming Carbon Fibers"; Presentation: ICCE 19, 19th Annual International Conference on Composites/Nano Engineering, Shanghai; 24.07.2011 - 30.07.2011.

M. Todt, F. G. Rammerstorfer, M.A. Hartmann, O. Paris, F.D. Fischer: "Shell-Models for Multi-Layer Carbon Nano-Particles;"; Presentation: EC 527 Shell-Like Structures - Non-Classical Theories and Applications, Wittenberg (invited); 22.08.2011 - 26.08.2011; in: "Shell-Like Structures", H. Altenbach, V.A. Eremeyev (Hrg.); Springer-Verlag, Berlin (2011), ISBN: 978-3-642-21854-5; S. 585 - 602.

F. G. Rammerstorfer, T. Daxner, F.D. Fischer, T. Flatscher, D. H. Pahr, M. Todt: "Instabilities in Materials at the Nano, Micro and Meso Scale"; Presentation: ECCM2010, European Conference on Computational Mechanics 2010, Paris; 21.05.2010 - 26.05.2010.

M. Todt, F. G. Rammerstorfer: "On the van der Waals Interactions Between Carbon Onion Layers"; Poster: Junior Scientist Conference 2010, Wien; 07.04.2010 - 09.04.2010; in: "Proceedings of the Junior Scientist Conference 2010", H. Kaiser, R. Kirner (Hrg.); (2010), ISBN: 978-3-200-01797-9; S. 215 - 216.

M. Todt, F. G. Rammerstorfer, R.D. Bitsche, F.D. Fischer, P.H. Mayrhofer, M.A. Hartmann, D. Holec, O. Paris: "On the Stability of Carbon Onions"; Presentation: GAMM 2010 - 81st Annual Meeting of the International Association of Applied Mathematics and Mechanics, Karlsruhe; 22.03.2010 - 26.03.2010.

M. Todt, T. Daxner: "Long Wave Instabilities in Periodic Structures"; Presentation: Junior Scientist Conference, Wien; 16.11.2008 - 18.11.2008.